CHARACTERISTICS OF ARCTIC STORMS AND THEIR IMPACT ON SURFACE
CLIMATE

By

Yang Yang, M.S.

A Dissertation Submitted in Partial Fulfillment of the Requirements

for the degree of

DOCTOR OF PHILOSOPHY

in

Atmospheric Sciences

University of Alaska Fairbanks
November 2019

Approved by:

Xiangdong Zhang, Advisor and Committee

Chair

Seth Danielson, Committee member

Javier Fochesatto, Committee member

Regine Hock, Committee member

Javier Fochesatto, Chair

Department of Atmospheric Sciences

Kinchel Doerner, Dean

College of Natural Science and Mathematics

Michael Castellini, Dean *Graduate school*

Abstract

Impacts of intense synoptic storms on Chukchi Sea and Beaufort Sea surface environmental conditions are examined, focusing on storms moving into the regions with northward and eastward pathways. Both storms alter the prevailing northeasterly wind to southerly and southwesterly wind. The storms moving from the East Siberian Sea that follow a west to east route are most active in summer and have the longest duration. Increasing southwesterly wind plays a key role in the decline of thin sea ice within the warm season. Storms traveling from the relatively warm Pacific Ocean into the Arctic over the Bering Strait are more common in winter, and are typically more intense than the summer storms that propagate west to east. Downward longwave radiation increases considerably with the passage of intense winter storms over the ice-covered Chukchi Sea; the sea ice concentration decreases accordingly.

The impact of different sea ice conditions on Arctic synoptic storm systems in autumn are investigated in the North Pacific and Atlantic sectors, based on the ten ensembles of hindcast simulations from coupled regional climate model HIRHAM-NAOSIM. In both the Pacific and Atlantic sectors, greater transfers of heat and moisture fluxes from the open ocean to the atmosphere occur in low sea ice years than in high sea ice years. The largest increase of upward heat fluxes and baroclinicity occurs over the Laptev, southern Chukchi and Beaufort Seas in the Pacific sector, and over the southern Greenland and Barents Seas in the Atlantic sector. Enhanced baroclinity plays a dominant role in the development of intense storm systems. Therefore, storms in reduced sea ice years are more intense than in enhanced sea ice years in both Atlantic and Pacific sectors. The storm count also increases over locations exhibiting high baroclinicity. Sea ice volume anomalies are significantly correlated with synoptic storm counts based on maximum covariance analysis (MCA). Leading modes of covariance between sea ice volume and storm count over

Pacific and Atlantic sectors are identified respectively. The results are consistent with our findings in the composite analysis. In the Pacific sector, the first pattern of the MCA demonstrates that increasing storm counts over the Laptev Sea corresponds to decreasing sea ice volume over that region. In the Atlantic sector, the decrease of sea ice volume is highly correlated with decreasing storm counts over the northern Greenland Sea.

Connection of storm activity over the North Pacific Ocean with the tropical stratosphere quasi-biennial oscillation (QBO) is investigated following a composite analysis of intense storm vertical cross sections. An observed stronger potential vorticity anomaly of intense storms is associated with the QBO west phase and results in enhanced warm air advection near the surface. A warm core structure forms over the east or northeast direction relative to the surface low center, which bows the isentropes downward. Upward motion following the isentropes reduces the surface low pressure, which in turn, facilitate storms to keep propagating in east and northeast directions. Under the QBO east phase, a weak surface warm core forms to the southeast of the storm center, resulting in a slow development of the storms, and these storms tend to move southeastward.

Table of Contents

List of Figures

Chapter 3

Chapter 4

Acknowledgement

I would like to take this opportunity to thank all of those who have generously offered me help and contributed to this PhD dissertation. I would like to thank my advisor Professor Xiangdong Zhang for his continuous supports and guidance through my Ph.D. study. My sincere thanks also go to my committee members Dr. Javier Fochesatto, Dr. Seth Danielson and Dr. Regine Hock for their insightful suggestions in all my committee meetings and during my defense. I would like to express my deep gratitude for the teaching assistant opportunities offered by Dr. Richard Collins. I would also like to thank Dr. Carl Tape for agreeing to be the outside examiner for my defense and his helpful comments on the dissertations. I would also like to extend my deepest gratitude to Dr. Annette Rinke for providing the ensemble data from the couple regional climate mode. I would also like to thank Dr. Jing Zhang for helping me with the CBHAR data and answering my questions in a timely manner. I would also like to thank Mr. Warren Horowitz for providing the funding to support my study of the storms over the Chukchi and Beaufort Seas.

I would like to express my deepest gratitude to my family for their unconditional love and support. I would like to thank my parents to their financial support to help me pursue my higher education. I would like to thank my husband Liran Peng for his support.

Finally, I would like to thank all the professors at the Department of Atmospheric Sciences and IARC for their support and. I thank all my friends and colleagues in the Akasofu building. I would like to also thank the enormous help I receive from the CNSM and the Graduate School.

Chapter 1 Introduction

The Arctic has experienced significant climate and environmental changes in recent decades, including dramatically decreased sea ice cover and considerably increased ocean and air temperatures (e.g., Rigor et al., 2000; Polyakov et al., 2003; Comiso et al., 2008; Steele et al., 2008; Screen and Simmonds, 2010; Simmonds and Rudeva, 2012). Dramatic decline of the Arctic sea ice (Parkinson and Cavalieri 2002; Comiso, 2006; Serreze at al., 2007; Comiso, 2012; Stroeve et al., 2012) leads to large open water areas that can result in stronger temperature contrast. Recent research has found an intensification of synoptic storm activity over the Arctic Ocean (e.g., Zhang et al., 2004; Serreze et al., 2008; Simmond et al., 2008; Woods and Caballero, 2016; Graham et al., 2017; Koyama et al., 2017; Rinke et al., 2017; Day and Hodges, 2018). As one outstanding example, a superstorm invaded the Beaufort-Chukchi seas in August 2012, contributing to record low summer sea ice coverage (Simmonds and Rudeva, 2012). With diminishing sea ice cover and more open water, we will likely observe increased frequency and intensity of storms (Inoue et al., 2012; Zhang, 2013; Vihma, 2014; Akperov et al., 2015), changes in surface wind patterns associated with location shift of the major low pressure systems (Danielson et al., 2014), and increased surface wind speeds (Ogi et al., 2010; Stegall and Zhang, 2012) and precipitation (Zhang et al., 2013). The communities along the coast of Alaska would be subject to the threat of extreme weather events caused by intense storms, which increase the potential for coastal erosion and flooding (Petrich et al., 2012).

The spatial resolution of hindcast models ranged from 50 km to 200 km in previous Arctic storm studies; such coarse resolution may not resolve mesoscale and sub-mesoscale geometrical features of storms. Little research has been undertaken using fine-resolution data to document climatological characteristics of storms in the Chukchi and Beaufort Seas and investigate how the

storms influence surface climate. The Chukchi-Beaufort High-resolution Atmospheric Reanalysis (CBHAR) has horizontal resolutions of 10 km for each hour from 1979 to 2009, which makes it possible to analyze high-resolution climatology features of synoptic storms and their influences on surface climate and ocean properties (Liu et al., 2013). In this study, we analyzed storms in the Chukchi and Beaufort Seas by categorizing them into two groups based on their main propagation pathways into the study domain. Then we investigate how the different groups of the storms influence the surface climate. The aim of this study is to document climatological features of the storms that travel along different pathways and their impact on the surface climate.

Over the Pan-Arctic domain, sea ice has been declining over the past decades and accelerated dramatically in the past few years (Serreze et al., 2007; Comison et al., 2008). The high albedo of sea ice can reflect solar radiation back to the space (Simmonds and Keay, 2002; Perovich et al., 2007). Without sea ice covering the ocean surface, solar radiation is absorbed by the ocean, which in turn causes a higher sea surface temperature and further melts more sea ice. Sea ice also serves as an importance boundary between the ocean and the atmosphere (Inoue et al., 2012). The exchange of heat between the ocean and the atmosphere is strongly moderated by the sea ice (Serreze et al., 2016). The warm ocean can provide more energy and moisture for the development of cyclones in the high latitude. The large sea ice extent anomaly during summer 1990 has been linked to a high frequency of cyclone activity over the central Arctic Ocean during spring (Serreze et al., 1995). Linkages between sea ice anomalies and a sharp increase since 1989 in the frequency of cyclones over the central Arctic were also proposed by Maslanik et al. (1996). Changes in sea ice thickness of the western Arctic lower boundary indicate an Arctic-wide response in the large-scale circulation and seem to have an impact on the troposphere-stratosphere coupling (Rinke et al., 2006). Negative Arctic sea ice anomalies are associated with increased heat

and moisture fluxes, decreased static stability, increased lower tropospheric moisture, and modified baroclinicity, synoptic activity and atmospheric large-scale circulation (Simmond and Keay, 2012).

The Atlantic water inflow through the Fram Strait and the Pacific water inflow through the Bering strait are considered as primary oceanic heat source affecting the sea ice variability (Rogers, 1997; Shimada et al., 2006; Woodgate et al., 2006; Rodionov et al., 2007). The influence of sea ice changes in these two sectors may result in different changes in cyclone activity in these regions (Serreze, 1995; Rogers, 1997). The storm characteristic in these two regions are also different. The response of the large-scale atmospheric circulation to the reduction of sea ice is most significant in the cold season (Deser et al., 2010). In winter, more Arctic storms migrate from the Atlantic side. It is of interest to know how sea ice change in either Pacific or Atlantic sector will impact the storms occurs in that area in winter seasons. Therefore, our study focuses on the influence of sea ice change on cyclone activity during winters in the Pacific and Atlantic sectors of the Arctic Ocean respectively.

An increased storm intensity and frequency over the North Pacific result in weather hazards, which challenged the offshore environment (Dupre, 1980; Dau et al., 2011; Terenzi et al., 2014), coastal community, and landscape (Anderson et al., 2018). Better understand the mechanisms controlling the storm track propagation and further predict its long-term variability has an important pratical implication. Previous studies show a connection between the stratospheric quasi-biennial oscillation (QBO) with tropical cyclone activities (Gray, 1984; Shapiro, 1989; Gray et al., 1992; Chan, 1995; Jury et al., 1999). However, the impact of QBO on storms tracks over the North Pacific receives less attention. An improved understanding of the physical mechanisms

connecting the QBO to the North Pacific storm tracks has the potential to promote seasonal and decadal scale forecast ability of the storm track patterns.

Many studies have revealed connections between the stratospheric variability and tropospheric circulation (Baldwin and Dunkerton, 2001; Thompson et al., 2002; Scaife et al., 2014, 2016; Kidston et al., 2015; Hansen et al., 2017; Tao et al., 2017) and direct connections between the QBO and tropospheric processes over tropical and subtropical regions (Giorgetta et al., 1999; Collimore et al., 2003; Ho et al., 2009; Liess and Geller, 2012; Garfinkel and Hartmann, 2011a; Nie and Sobel, 2015). The impact of the QBO on Northern Hemisphere stratospheric polar vortex (PV) has been well known for decades (Holton and Tan, 1980, 1982; Baldwin et al., 2001; Anstey and Shepherd, 2014). The variability of the equatorial winds affects the vertical propagation of planetary-scale waves from the troposphere via its influence on the stratospheric waveguide in winter via refraction or reflection of the waves towards (away from) high latitudes. The PV becomes stronger (weaker) when the QBO winds in the lower-mid stratosphere are westerly (easterly) phase (Lu et al., 2008, 2014; Anstey and Shepherd, 2008; Christiansen, 2010).

Mid-latitude storms travels through the North Pacific is an important pathway impact on the Arctic climate (Zhang et al., 2004). The phase lock between an upstream upper-level PV anomaly and a downstream lower-level PV anomaly has been shown to contribute to storm intensification (e.g. Hoskinset al.,1985; Davis and Emanuel, 1991; Rossaet al., 2000; Cavallo and Hakim, 2010; Campa and Wernli, 2012; Odellet et al., 2013). In this study, we connect the upper level PV anomaly under two QBO phase conditions to surface storm tracks propagation.

References

Akperov, M.G.; Mokhov, I.I.; Rinke, A.; Dethloff, K.; Matthes, H. (2015): Cyclones and their possible changes in the Arctic by the end of the 21st century from regional climate model simulations. *Theor. Meteorol. Clim.*, 122, 85–96.

Anderson, T. R., and Coauthors (2018): Modeling multiple sea level rise stresses reveals up to twice the land at risk compared to strictly passive flooding methods. *Sci. Rep.*, 8(1), 14484.

Anstey, J. A. and Shepherd, T. G. (2008): Response of the north- ern stratospheric polar vortex to the seasonal alignment of QBO phase transitions, *Geophys. Res. Lett.*, 35, L22810,

Anstey, J. A. and Shepherd, T. G. (2014): High-latitude influence of the quasi-biennial oscillation, *Q. J. Roy. Meteor. Soc.*, 140, 1–21.

Baldwin, M. P. and Dunkerton, T. J. (2001): Stratospheric Harbingers of Anomalous Weather Regimes, *Science*, 294, 581–584.

Campa J., Wernli H. (2012): A PV perspective on the vertical structure ofmature midlatitude cyclones in the Northern Hemisphere. *J. Atmos. Sci.*, 69, 725 – 740.

Cavallo SM, Hakim G. J. (2010): Composite structure of tropopause polarcyclones. *Mon. Weather Rev.*, 138, 3840–3857.

Chan, J. C. L. (1995): Tropical cyclone activity in the western North Pacific in relation to the stratospheric quasi-biennial oscillation, *Mon. Wea. Rev.*, 123, 2567−2571.

Christiansen, B. (2010): Stratospheric bimodality: can the equatorial QBO explain the regime behavior of the NH winter vortex, *J. Clim*, 23, 3953–3966.

Collimore, C. C., Martin, D. W., Hitchman, M. H., Huesmann, A., and Waliser, D. E. (2003): On the relationship between the QBO and tropical deep convection, *J. Clim*, 16, 2552–2568.

Comiso, J. C. (2006): Abrupt decline in the Arctic winter sea ice cover. *Geophys. Res. Lett.*, 33, L18504

Comiso, J. C., C. L. Parkinson, R. Gersten, and L. Stock (2008): Accelerated decline in the Arctic sea ice cover. *Geophys. Res. Lett.*, 35, L01703.

Danielson, S. L., T. W. Weingartner, K. Hedstrom, K. Aagaard, R. Woodgate, E. Curchitser, and P. Stabeno (2014): Coupled wind-forced controls of the Bering–Chukchi shelf circulation and the Bering Strait through-flow: Ekman transport, continental shelf waves, and variations of the Pacific–Arctic sea surface height gradient, *Prog. Oceanogr*.

Dau, C. P., J. G. King Jr. and C. J. Lensink (2011): Effects of storm surge erosion on waterfowl habitats at the Kashunuk River, Yukon– Kuskokwim Delta, Alaska. U.S. Fish and Wildlife Service, Anchorage, Alaska, USA.

Davis C. A., Emanuel K. A. (1991): Potential vorticity diagnostics of cyclogenesis. *Mon. Weather Rev.*, 119, 1929 – 1953.

Day, J. J. and K. I. Hodges. (2018): Growing Land-Sea Temperature Contrast and the Intensification of Arctic Cyclones. *Geophys. Res. Lett.*, 45, 3673-3681.

Dee, D. P., Uppala, S. M., Simmons, A. J., Berrisford, P., Poli, P., Kobayashi, S., Andrae, U., Balmaseda, M. A., Balsamo, G., Bauer, P., Bechtold, P., Beljaars, A. C. M., van de Berg, L., Bid- lot, J., Bormann, N., Delsol, C., Dragani, R., Fuentes, M., Geer, A. J., Haimberger, L., Healy, S. B., Hersbach, H., Hólm, E. V., Isaksen, L., Kållberg, P., Köhler, M., Matricardi, M., McNally, A. P., Monge-Sanz, B. M., Morcrette, J.-J., Park, B.-K., Peubey, C., de Rosnay, P., Tavolato, C., Thépaut, J.-N., and Vitart, F. (2011): The ERA-Interim

reanalysis: configuration and performance of the data assimilation system, *Q. J. Roy. Meteor. Soc.*, **137**, 553–597.

Deser, C., R. Tomas, A. Alexander, and D. Lawrence (2010): The seasonal atmospheric response to projected Arctic sea ice loss in the late 21st century, *J. Clim*., 23, 333– 351,

Dupre, W. R. (1980): Yukon Delta coastal processes study. National Oceanic and Atmospheric Administration, Outer Continental Shelf Environmental Assessment Program, Tech. Rep., 58, 393–447.

Giorgetta, M. A., Bengtsson, L., and Arpe, K. (1999): An investigation of QBO signals in the east Asian and Indian monsoon in GCM experiments. *Clim. Dynam*., 15, 435–450.

Garfinkel, C. I. and Hartmann, D. L. (2011), The influence of the quasi- biennial oscillation on the troposphere in winter in a hierarchy of models. Part I: Simplified dry GCMs, *J. Atmos. Sci.*, 68, 1273– 1289.

Graham, R. M., L. Cohen, A. A. Petty,L. N. Boisvert, A. Rinke, S. R. Hudson,M. Nicolaus, and M. A. Granskog (2017): Increasing frequency and duration of Arctic winter warming events, *Geophys. Res. Lett.*, 44, 6974–6983.

Gray, W. M. (1984): Atlantic seasonal hurricane frequency. Part I: El Nino and 30 mb quasi-biennial oscillation influences, *Mon. Wea. Rev*., 112, 1649−1668.

Gray, W. M., C. W. Landsea, P. W. Mielke Jr., and K. J. Berry (1992): Predicting Atlantic seasonal hurricane activity 6−11 months in advance, *Wea. Forecasting*, 7, 440−455.

Gray, L. J. (2003): The influence of the equatorial upper stratosphere on stratospheric sudden warmings, *Geophys. Res. Lett*., 30, 1166– 1169.

Hansen, F., Greatbatch, R. J., Gollan, G., Jung, T., and Weisheimer, A. (2017): Remote control of North Atlantic Oscillation predictability via the stratosphere, *Q. J. Roy. Meteorol. Soc.*, 143, 706–719.

Inoue, J., M. E. Hori, and K. Takaya (2012): The role of Barents sea ice in the wintertime cyclone track and emergence of a warm-Arctic cold-Siberian anomaly, *J. Clim.*, 25, 2561– 2568.

Ho, C. H., Kim, H. S., Jeong, J. H., and Son, S. W. (2009): Influence of stratospheric quasi-biennial oscillation on tropical cyclone tracks in western North Pacific. *Geophys. Res. Lett.*, 36, L06702.

Holton, J. R. and Tan, H.-C. (1980): The Influence of Equatorial Quasi- Biennial Oscillation on the Global Circulation at 50 mb, *J. Atmos. Sci.*, 37, 2200–2208.

Holton, J. R. and Tan, H.-C. (1982): The quasi-biennial oscillation in the Northern Hemisphere lower stratosphere, *J. Meteorol. Soc. Jpn.*, 60, 140–148.

Hoskins B. J., McIntyre M. E., Robertson A. W. (1985): On the use and significance of isentropic potential vorticity maps. *Q. J. R. Meteorol. Soc.*, 111, 877 – 946.

Jury, M. R., B. Pathack, and B. Parker (1999): Climatic determinants and statistical prediction of tropical cyclone days in the southwest Indian Ocean, *J. Clim.*, 12, 1738−1746.

Kidston, J., Scaife, A. A., Hardiman, S. C., Mitchell, D. M., Butchart, N., Baldwin, M. P., and Gray, L. J. (2015): Stratospheric in- fluence on tropospheric jet streams, storm tracks and surface weather, *Nat. Geosci.*, 8, 433–440.

Kim, B. K., Hong, J. Y., Jun, S. Y., Zhang, X., Kwon, H., Kim, S. J., Kim, J. H., Kim, S. W., Kim, H. K (2017): Major cause of unprecedented Arctic warming in January 2016: Critical role of an Atlantic windstorm. *Sci. Rep.*, 7, 40051.

Koyama, T, J. Stroeve, J. Cassano, and A. Crawford (2017): Sea Ice Loss and Arctic Cyclone Activity from 1979 to 2014, *J. Clim*., 30, 4735–54

Liess, S. and Geller, M. A. (2012): On the relationship between the QBO and distribution of tropical deep convection, *J. Geophys. Res.- Atmos*., 117, D03108.

Liu F., J. R. Krieger, and J. Zhang (2014): Toward Producing the Chukchi–Beaufort High-Resolution Atmospheric Reanalysis (CBHAR) via the WRFDA Data Assimilation System. *Mon. Wea. Rev*., 142, 788–805.

Lu, H., Baldwin, P. B., Gray, L. J., and Jarvis, M. J. (2008): Decadal- scale changes in the effect of the QBO on the northern stratospheric polar vortex, *J. Geophys. Res*., 113, D10114,

Lu, H., Bracegirdle, T. J., Phillips, T., Bushell, A., and Gray, L. J. (2014): Mechanisms for the Holton–Tan relationship and its decadal variation, *J. Geophys. Res.- Atmos*., 119, 2811–2830.

Nie, J. and Sobel, A. H. (2015): Responses of tropical deep convection to the QBO: Cloud-resolving simulations*, J. Atmos. Sci*., 72, 3625– 3638.

Odell L., Knippertz P., Pickering S., Parkes B., Roberts A. (2013): The Braer storm revisited. *Weather*, 68, 105 – 111.

Ogi, M., Yamazaki, K., Wallace, J.M. (2010): Influence of winter and summer surface wind anomalies on summer Arctic sea ice extent. *Geophys. Res. Lett*., 37, L07701.

Parkinson, C. L., and D. J. Cavalieri (2002): A 21 year record of Arctic sea-ice extents and their regional, seasonal and monthly variability and trends. *Ann. Glaciol*., 34, 441–446.

Perovich, D. K., B. Light, H. Eicken, K. F. Jones, K. Runciman, and S. V. Nghiem (2007): Increasing solar heating of the Arctic Ocean and adjacent seas, 1979–2005: Attribution and role in the ice-albedo feedback, *Geophys. Res. Lett.*, 34, L19505,

Petrich, C., H. Eicken, J. Zhang, J. R. Krieger, Y. Fukamachi, and K. I. Ohshima (2012): Coastal landfast sea ice decay and break-up in northern Alaska: Key processes and seasonal prediction, *J. Geophys. Res.*, 117, C02003,

Polyakov, I. V., R. V. Bekryaev, G. V. Alekseev, U. S. Bhatt, R. L. Colony, M. A. Johnson, A. P. Maskshtas, and D. Walsh (2003): Variability and trends of air temperature and pressure in the maritime Arctic, 1875–2000. *J. Clim*, 16, 2067–2077.

Rigor, I. G., R. L. Colony, and S. Martin (2000): Variations in surface air temperature observations in the Arctic, 1979–97. *J. Clim*, 13, 896–914.

Rinke, A., M. Maturilli, R. M. Graham, H. Matthes, D. Handorf, L. Cohen, S. R. Hudson, and J. C. Moore (2017): Extreme cyclone events in the Arctic: Wintertime variability and trends, *Environ. Res. Lett*.

Rodionov, S., N. Bond, and J. Overland (2007): The Aleutian low, storm tracks, and winter climate variability in the Bering Sea. *Deep-Sea Res.*, 54, 2560–2577.

Rogers, J. C. (1997): North Atlantic storm track variability and its association to the North Atlantic Oscillation and climate variability of Northern Europe, *J. Clim*, 10, 1635–1645.

Rossa A. M., Wernli H., Davies H. C. (2000): Growth and decay of an extra-tropicalcyclone's PV-tower. *Meteorol. Atmos. Phys.*, 73: 139 – 156.

Rinke, A., R. Gerdes, K. Dethloff, T. Kandlbinder, M. Karcher, F. Kauker, S. Frickenhaus, C. Köberle, and W. Hiller (2003): A case study of the anomalous Arctic sea ice conditions

during 1990: Insights from coupled and uncoupled regional climate model simulations, *J. Geophys. Res.*, 108(D9), 4275.

Rinke, A., K. Dethloff, W. Dorn, D. Handorf, and J. C. Moore (2013): Simulated Arctic atmospheric feedbacks associated with late summer sea ice anomalies, *J. Geophys. Res. Atmos.*, 118, 7698–7714.

Roeckner, E; Bäuml, G; Bonaventura, L; Brokopf, R; Esch, M; Giorgetta, M; Hagemann, S; Kirchner, I; Kornblueh, L; Manzini, E; Rhodin, A; Schlese, U; Schulzweida, U; and Tompkins, A (2003): The atmospheric general circulation model ECHAM5. Part 1. Model description. Report no. 349, Max-Planck-Institut für Meteorologie (MPI-M).

Scaife, A. A., Athanassiadou, M., Andrews, M., Arribas, A., Baldwin, M., Dunstone, N., Knight, J., MacLachlan, C., Manzini, E., Müller, W. A., Pohlmann, H., Smith, D., Stockdale, T., and Williams, A. (2014): Predictability of the quasi-biennial oscillation and its northern winter teleconnection on seasonal to decadal timescales. *Geophys. Res. Lett.*, 41, 1752–1758.

Scaife, A. A., Karpechko, A. Y., Baldwin, M. P., Brookshaw, A., Butler, A. H., Eade, R., Gordon, M., MacLachlan, C., Martin, N., Dunstone, N., and Smith, D. (2016): Seasonal winter forecasts and the stratosphere, *Atmos. Sci. Lett.*, 17, 51–56.

Screen, J. A., and I. Simmonds (2010), The central role of diminishing sea ice in recent Arctic temperature amplification. *Nature.*, 464, 1334–1337.

Serreze, M. C. (1995), Climatological aspects of cyclone development and decay in the Arctic. *Atmos.–Ocean.*, 33, 1–23.

Serreze, M. C., M. M. Holland, and J. Stroeve (2007): Perspectives on the Arctic's shrinking sea-ice cover. *Science*, 315, 1533–1536.

Serreze, M. C., and A. P. Barrett (2008), The summer cyclone maximum over the central Arctic Ocean. *J. Clim.*, 21, 1048–1065.

Serreze M C, Stroeve J., Barrett A. P. and Boisvert L. N. (2016): Summer atmospheric circulation anomalies over the Arctic Ocean and their influences on September sea ice extent: a cautionary tale. *J. Geophys. Res.- Atmos.*, 121, 11463–85

Shapiro, L. (1989): The relationship of the QBO to Atlantic tropical storm activity, *Mon. Wea. Rev.*, 117, 1545–1552.

Shimada, K., T. Kamoshida, M. Itoh, S. Nishino, E. Carmack, F. McLaughlin, S. Zimmerman, and A. Proshutinsky (2006): Pacific Ocean inflow: Influence on catastrophic reduction of sea ice cover in the Arctic Ocean, *Geophys. Res. Lett.*, 33, L08605,

Skamarock, W. C., and Coauthors (2008): A description of the Advanced Research WRF version 3. NCAR Tech Note NCAR/TN–4751STR, 113 pp.

Simmonds, I., C. Burke, K. Keay (2008), Arctic climate change as manifest in cyclone behavior. *J. Clim.*, 21: 5777-5796.

Simmonds I. and Keay K. (2002): Surface fluxes of momentum and mechanical energy over the North Pacific and North Atlantic Oceans. *Meteorol Atmos Phys.* 80, 1–18

Simmonds, I., and I. Rudeva (2012), The great Arctic cyclone of August 2012. *Geophys. Res. Lett.*, 39, L23709.

Steele, M., W. Ermold, and J. Zhang (2008), Arctic Ocean surface warming trends over the past 100 years. *Geophys. Res. Lett.*, 35, L02614.

Stegall, S. T., and J. Zhang (2012): Wind field climatology, changes, and extremes in the Chukchi/Beaufort Seas and Alaska North Slope during 1979–2009. *J. Clim*, 25, 8075–8089.

Tao, W., Zhang, J., Zhang, X. (2017): Driving roles of tropospheric and stratospheric thermal anomalies in the intensification and persistence of 2012 Arctic superstorm. *Geophys. Res. Lett.*, 44, 10017–10025

Terenzi, J., M. T. Jorgenson, and C. R. Ely. (2014): Storm-surge flooding on the Yukon–Kuskokwim Delta, Alaska. Arctic 67:360–374.

Thompson, D. W. J., Baldwin, M. P., and Wallace, J. M. (2002): Stratospheric connection to Northern Hemisphere wintertime weather: Implications for prediction, J. Clim, 15, 1421–1428.

Thorndike, A. S., and R. Colony (1982): Sea ice motion in response to geostrophic winds. *J. Geophys. Res.*, 87C, 5845–5852.

Undén, P; Rontu, L; Järvinen, H; Lynch, P; Calvo, J; Cats, G; Cuxart, J; Eerola, K; Fortelius, C; Garcia-Moya, J A; Jones, C; Lenderlink, G; McDonald, A; McGrath, R; Navascues, B; Woetman Nielsen, N; Ødegaard, V; Rodrigues, E; Rummukainen, M; Rõõm, R; Sattler, K; Hansen Sass, B; Savijärvi, H; Wichers Schreur, B; Sigg, R; The, H; and Tijm, A (2002): HIRLAM-5 Scientific Documentation. Scientific Report.

Vihma, T. (2014): Effects of Arctic sea ice decline on weather and climate: A review. *Surv. Geophys*. 2014, 35, 1175–1214.

Wendler, G. (1973): Sea ice observation by means of satellite, *J. Geophys. Res.*, 78(9), 1427-1448

Woodgate, R. A., K. Aagaard, and T. J. Weingartner (2006): Interannual changes in the Bering Strait fluxes of volume, heat and freshwater between 1991 and 2004, *Geophys. Res. Lett.*, 33, L15609

Woods, C. and R. Caballero (2016), The Role of Moist Intrusions in Winter Arctic Warming and Sea Ice Decline. *J. Clim.*, 29, 4473–4485

Zhang, J., et al. (1998): Warming of the Arctic Ocean by a strengthened Atlantic inflow: model results, *Geophys. Res. Lett.*, 25, 1745– 1748.

Zhang, J., Lindsay, R., Schweiger, A., Steele, M. (2013): The impact of an intense summer cyclone on 2012 Arctic sea ice retreat. *Geophys. Res. Lett.*, 40, 720–726.

Zhang, X., J. E. Walsh, J. Zhang, U. S. Bhatt, and M. Ikeda (2004): Climatology and interannual variability of Arctic cyclone activity, 1948–2002. *J. Clim.*, 17, 2300– 2317.

Zhang, X., Sorteberg, A., Zhang, J., Gerdes, R., Comiso, J.C. (2008): Recent radical shifts in atmospheric circulations and rapid changes in Arctic climate system. *Geophys. Res. Lett.*, 35, L22701.

Zhang, X., J. Zhang, J. Krieger, M. Shulski, F. Liu, S. Stegall, W. Tao, J. You, and B. Potter, (2013): Beaufort and Chukchi Seas Mesoscale Meteorology Modeling Study, Final Project Report. Bureau of Ocean Energy Management, BOEM 2013-0119, 204 pp.

Zhang, X., He, J., Zhang, J., Polyakov, I., Gerdes, R., Inoue, J., Wu, P. (2013): Enhanced poleward moisture transport and amplified northern high-latitude wetting trend. *Nat. Clim. Chang.*, 3, 47–51.

Chapter 2 Chukchi and Beaufort Seas Storms and Their Impacts on Surface Environmental

Conditions

Abstract

To examine the impacts of storms on Chukchi and Beaufort Seas, we focus on a subset of intense storms entering the region either following a northward pathway from the North Pacific Ocean or following an eastward track from East Siberia Sea. These storms have distinct origins and characteristics, which generate substantial regional variations in surface environmental conditions, including sea level pressure, 10-meter surface wind, 2-meter air temperature and sea surface temperature, surface downward longwave and shortwave radiations, sensible and latent heat fluxes. Using the Chukchi-Beaufort High-Resolution Atmospheric Reanalysis (CBHAR) dataset, we compare the composite surface environmental parameters under the influence of storms with their climatological values. The results show that storms with west to east route moving into the Chukchi and Beaufort Seas are most active in summer, while winter is the preferable season for storms moving northward over the Bering Strait. Storms traveling from the relatively warm Pacific Ocean into the ice-covered Chukchi and Beaufort Seas in winter are typically stronger than the summer storms, with respect to central pressure and wind speed. The strengthened low pressure center is accompanied by an intensified Beaufort High, causing significant increase of maximum wind speed in between over the Chukchi Sea. Both storms change the prevailing northeasterly wind over the Bering Strait to warm and moist southerly and southwesterly wind. Extensive cloud coverage associated with the storms has a large impact on the amount of radiation received at the surface. Although negative surface downward shortwave radiation anomalies outweigh the positive longwave radiation anomalies in summer, surface temperature increase and sea ice concentration declines indicating the predominant role the southwesterly wind plays over the thin

ice and open water area in warm season. On the other hand, due to lack of daylight in winter, downward longwave radiation increases considerably with the passage of intense storms over the ice-covered Chukchi Sea and the sea ice concentration decrease accordingly, suggesting the limited effect of southwesterly wind over ice-covered surface.

2.1 Introduction

The Arctic has experienced significant environmental changes, including rapidly decreased sea ice cover and considerably increased ocean and air temperatures (e.g., Comison, 2006; Comiso et al., 2008; Steele et al., 2008; Screen and Simmonds, 2010). Recent research has found an intensification of synoptic storm activity over the Arctic Ocean (e.g., Zhang et al., 2004; Serreze et al., 2008; Simmond et al., 2008; Woods and Caballero, 2016; Graham et al., 2017). Presence of storms can alter the wind pattern, surface temperature and atmospheric heat and moisture transport into the Arctic (Screen et al., 2011). The Chukchi and Beaufort seas are home to some of the most intense storms in the Arctic. Previous studies show that the storms travel into this region primarily from East Siberia Sea (Reed and Kunkel, 1960) and from the North Pacific Ocean (Serreze and Barry, 1988; Serreze and Barrett, 2008). As one outstanding example for storms migrating into the area from west, a superstorm invaded the Beaufort and Chukchi seas in August 2012 from East Siberia Sea, contributing to record low summer sea ice coverage (Simmonds and Rudeva, 2012). Pacific origin storms approaching the area near the Bering Strait, which is the gateway from the Pacific Ocean to the Arctic Ocean, on a south to north course. They transport warm and moist air from the open water to the Chukchi and Beaufort Seas and thus also play a significant role in melting sea ice. With little to no sea ice, the coastal communities especially in the Chukchi Sea are subject to the threat of extreme weather events and very late formation of landfast ice caused

by intense storms. In the Beaufort Sea, strong surface winds driven by storms can result in coastal erosion and flooding (Reimnitz and Maurer, 1979). Storms with distinct origins and characteristics have different active period over the Chukchi and Beaufort Seas and their strengths vary seasonally, which can produce substantial regional changes in surface environmental conditions. Climatological statistic of storm activity in the Arctic have been elaborated since the 80s (Serreze and Barry 1988, Serreze et al., 1993, Serreze 1995, Serreze 1997, Barry 1998). Little research has been undertaken using fine resolution data to document climatological characteristics of storms from different source regions and investigate how they influence surface climate in the Chukchi and Beaufort Seas. The focus of this study is on the distinct behavior of storms originated outside of the Chukchi and Beaufort Seas and moved into the area along two primary pathways: one is migrating northward over the Bering Strait and adjacent land area from the North Pacific Ocean and the other is moving from the East Siberia Sea into the Chukchi and western Beaufort Seas. We document climatological features of the storms travel along different pathways and address the question on how they influence the surface environmental conditions. The study is organized as follows: data and method are described in Section 2; climatology of storms with different origins and moving routes and their distinct impacts on surface variables are present is Section 3; section 4 discuss and summarizes the results.

2.2 Data and Methods

This study is based on the 31-yr, 10-km horizontal, 1-hourly Chukchi-Beaufort High-resolution Atmospheric Reanalysis (CBHAR) (Liu et al., 2014; Zhang et al., 2013). The Advanced Research core of WRF (ARW; Skamarock et al. 2008) is the main tool for generating this reanalysis dataset. CBHAR is a three-dimensional observationally constrained and thermodynamically and

dynamically consistent gridded hindcast reanalysis. It covers the Chukchi and Beaufort Seas, the North Slope of Alaska and the Brooks Range, the western part of the Canadian Yukon and the East Siberian Sea. The initial and lateral boundary conditions are from The European Centre for Medium-Range Weather Forecasts (ECMWF) Interim Re-Analysis (ERA-I; Dee et al. 2011). The high spatial resolution makes it possible to analyze high-resolution climatology features of synoptic storms and their influences on surface climate and ocean properties.

We applied and refined the automatic storm identification and tracking algorithm developed by Zhang et al (2004) using 6-hourly sea level pressure (SLP) fields to track the storms. A storm center is identified if the SLP at the grid point is lower than all surrounding grid points within a 50 km radius using the CBHAR data. The minimum SLP gradient between the center of the storm and every surrounding grid point must be at least 0.1 hPa per 100 km. Two adjacent storm centers appearing at the same time within 500 km of each other are identified as the same storm system with the lowest storm center as the center of the combined storm system. The life time of storms must be at least 12 hours and each individual storm track must be at least 100 km long. The latter criteria eliminate minor disturbances generated by orographic effects.

Storm intensity, duration and track number have been calculated to study the climatology of Chukchi and Beaufort Seas storms. The storm intensity is obtained by calculating the mean absolute values of the difference between the central SLP of the storm and the climatological monthly mean SLP at the corresponding grid points over the cyclone duration. Intensity of storms in the month are averaged to get monthly mean absolute values. The storm track number is the count of storms moving in a particular geographical region in a month. The storm duration is the length of time between the first appearance of the storm and its subsequent disappearance. The average storm duration is obtained by averaging the storm durations within each region.

To investigate the characteristics of storms moving into the Chukchi and Beaufort seas along different pathways, we categorize all the storms into two groups based on the most frequent direction of motions they travel along. The first group of storms generated over west of Chukchi Sea move into the region along a west to east route. The second group of storms entered the area over the Bering Strait and adjacent land area from the Pacific Ocean migrate on a south to north course. Based on this criterion, a total of 85 first group storms and 64 second group storms are identified during the 31 years period. The total storm tracks of the two groups are displayed in Figure 1. We then performed composite analysis for each group of storm tracks using the CBHAR data by adding together the value of surface variable at each time step over each storm lifetime. We then sum all the averaged individual field for the two groups of storms respectively and divide by total storm track numbers of each storm track type over the years from 1979 to 2009. To study the surface climate variability linkage to storms, the composite analysis is performed for sea level pressure (SLP), 10-meter surface winds, 2-meter surface air temperatures (SAT), sea surface temperature (SST), downward longwave radiation (DWL) and downward shortwave radiation (DSR), surface sensible and latent heat fluxes. By performing the composite analysis, the details of individual storms are eliminated, leaving only the general features for storm along a specific pathway. Through the comparison of the results from composite analysis and surface climatological conditions, we highlight the substantial role of storms in modification of surface environmental parameters.

2.3 Results

2. 3. 1 Storm track climatology

Figure 2 shows annual cycle of storm activity for both groups. Group 1 and group 2 stand for storms following eastward and northward progression directions into the Chukchi and wester Beaufort Seas respectively. With activity peaks in summer, all three parameters, intensity, storm track number and duration show a clear seasonal cycle for group 1 storms. Climatologically, Arctic storms are not active in summer and it is widely acknowledged that the Arctic storms are typically more intense in winter. However, this is not the case for the group 1 storms. One the other hand, group 2 storms only display a modest seasonal cycle being most active during winter. Winter has the highest group 2 storm frequency, whereas summer has the lowest. The seasonal cycle of the group 1 and group 2 storms is out of phase with regard to their activities. To characterize the surface climate variability linkage to the most active and intense storms with different origins, we choose summer (June, July and August) group 1 storms and winter (December, January and February) group 2 storms to investigate the response of surface conditions over the Chukchi and western Beaufort Seas.

2. 3. 2 Composite analysis and comparison with climatological condition

We conducted a composite analysis of surface climate parameters under the influence of group 1 storms in summer (JJA) and group 2 storms in winter (DJF) for the 31 years period from 1979 to 2009 in the Chukchi and western Beaufort region. The surface climate parameters presented here are SLP, 10-meter wind, 2-meter surface temperature, SST, and energy budget terms, including downward longwave radiation and downward shortwave radiation. Averages of the parameters for summer (June, July and August) and winter were performed for comparison with the corresponding composites under the impact of group 1 and group 2 storms.

Climatologically, summer has a tendency for weak low-pressure system to be centered over the western Beaufort Sea at about 135° longitude and 73° latitude with a minimum SLP of about 1015 hPa (Figure 3a). In winter, the minimum pressure center locates farther south, south of the Bering Strait, with a minimum SLP below 1005 hPa (Figure 3b). Another noticeable feature of the winter SLP field is the presence of a high-pressure system over the northern Chukchi Sea and East Siberia Sea. Climatologically, the low pressure systems are more intense in winter than in summer due to the strong baroclinicity in the cold season.

Figure 4a shows the composite SLP field under the influence of group 1 storms in summer. Figure 4a features a closed low pressure center with a central pressure of about 1003 hPa over the East Siberia Sea, which is west of their climatological location. The winter composite SLP based on group 2 storms features a dipole pattern with a pronounced low pressure belt extending northward over the Bering Strait into the southern Chukchi Sea and a stronger Beaufort High (Figure 4b). The strengthened high pressure center is located east of its climatological position and the anomalous low pressure center covers a larger area north of the Bering Strait and over the adjacent land. Both low and high SLP centers are more intense then the climatological values and the isobars are more closely spaced, indicating a steeper pressure gradient between the low and high pressure systems in the composite SLP fields, which can cause anomalously strong winds in between.

Comparisons with the surface climatological SLP were undertaken to help diagnose the different responses of SLP to the winter group 2 storms. Figure 5 shows the difference between the composite and climatological SLP fields for both groups of storms. It is obvious that group 2 storms in winter make a greater impact on surface SLP. Summer group 1 storms induce moderate change of SLP with a decrease of about 5 hPa of central pressure over the East Siberia Sea (Figure

5a). When cold seasons storms enter the region, the central low pressure is about 20 hPa lower than the climatological value over the Bering Strait and southern Chukchi Sea (Figure 5b).

Figure 6 shows the climatological 10-meter wind patterns with surface wind vectors superimposed on the maps of wind speeds for JJA and DJF. In summer, surface wind speeds are much weaker compared to winter. In winter, northeast wind prevails over Chukchi and Beaufort Seas with maximum wind speed located over the open water near the coast south of the Bering Strait.

Corresponding composite 10-meter wind patterns of summer group 1storms and winter group 2 storms are displayed in Figure 7. The group 1 storms in summer bring southwesterly and southernly winds in Chukchi and western Beaufort Seas with a moderate increase of wind speeds near the East Siberia Sea coast and decrease of wind speeds over the Beaufort Sea (Figure 7a). With the onset of intense group 2 winter storms, there is a dramatic shift of wind directions and increase of wind speeds over the central Chukchi Sea (Figure 7b). In contrast to the Climatological northerly wind blowing over the Bering Strait, southerly winds dominate and turn anticlockwise into strong easterly winds over the central Chukchi Sea. It is obvious that the winter storms can reverse the direction of prevailing northerly wind to southerly wind over the Bering Strait. The southerly wind can bring warm and moist air into the Arctic. The locations of maximum wind speeds shift to the ice-covered central Chukchi Sea and along the coast of East Siberia. The wind speed above 10 m s^{-1} dominates a relatively large area of the Chukchi Sea. The maximum wind speed is located northeast of the composite winter group 2 storm center and is significantly correlated with the composite SLP pattern mentioned in the previous section. The maximum wind speed is related to the steep pressure gradient between the strengthened low pressure systems over the southern Chukchi Sea and high pressure systems over the western Beaufort Sea.

22

Wind speeds anomalies and wind vectors difference between the composite and climatological 10-meter surface wind fields are shown in Figure 8. There is no pronounced increase of wind speed when storms happen in summer but still the wind pattern shift notably over Chukchi Sea. Storms make southerly wind dominates over the Bering Strait and southern Chukchi Sea during winter even though the wind speed did not change much in those areas. The greatest wind speeds anomalies caused by the winter storms are situated in central Chukchi Sea and other region of wind speed increase is also found along the northernmost of East Siberian coast. The wind speeds in the Beaufort Sea do not change very much in both summer and winter.

Figure 9 illustrates the climatological summer and winter 2-meter surface air temperature. In summer, temperature contrast between open water and the ice-covered ocean is relatively small compared to winter, which indicates a stronger baroclinicity in winter. The highest SAT appears inland over Alaska in summer while the SAT peaks over northern Bering Sea open water in winter. When winter storms travel into the Chukchi Sea over the Bering Strait and adjacent areas, they warm the overlying SAT as warm oceanic air from North Pacific is advected northward (Figure 10). The warm SAT are shown to extend far into the Chukchi Sea reflecting the extensive warming effects of the storms in winter. These regions are collocated with regions of reduced SLP caused by the winter storms.

The difference between climatological and composite SAT is shown in Figure 11. Only winter storms can cause dramatic warming over Chukchi Sea and adjacent land in Alaska. The strong southerly wind is a key factor to this dramatic increase of temperature. The change of SAT caused by the summer storms is small with negligible decrease of temperature over northwestern Alaska.

As is typical for winters during 1979 to 2009 periods, Chukchi Sea is mostly ice-covered. When sea ice is present, even intense storms do not cause significant oceanic response. As a result, the winter group 2 storms have limited impact on the SST over the ice-covered Chukchi and Beaufort Seas and there is no remarkable difference between the climatological and composite SST field (Figure 12a). Summer group 1 storms have a stronger impact on SST with maximum increase over the Beaufort Sea coastal area and decrease over the southern Chukchi Sea. Both locations are ice-free in summer. The SST over and south of the Bering Strait open water area decreases slightly as the winter group 2 storms move into the region with magnitude about 0.2°C (Figure 12b). The possible process that might be responsible for the cooling is the vertical mixing enhanced by strong winds associated with the storms. The increased vertical mixing can induce cold water upwelling to the surface (Pickart et al., 2009).

Intense storms can increase cloudiness and modify the surface downward shortwave radiation (DSR) and downward longwave radiations (DLR) (Curry et al., 1996). Extensive cloud coverage associated with storms can trap heat emitted by the surface and re-emit part of the energy back to the surface causing an increase in DLR, while block and reflect solar radiation from the Sun causing a decrease in the DSR (Perovich et al., 2007). In general, positive anomalies of surface DSR appear under clear-sky conditions, whereas negative anomalies are associated with cloudy conditions. Figure 13a supports the fact that the presence of cloud associated with the summer group 1 storms significantly decreases surface DSR. The summer storms also play an opposing role of increasing the DLR (Figure 13b). With coincidence in the spatial patterns, a positive DLR anomaly is accompanied by a negative DSR. The magnitude of the decreased DSR is much larger than that of the increased DLR. Therefore, the DSR cooling effect outweighs the DLR warming effect when summer storms are over the region. The relative importance of DSR and DLR

anomalies depend on cloud height, thickness and hydrometer type and concentration, which are beyond the scope of this study. Due to the absence of solar radiation during winter, incoming shortwave radiation is negligible. Figure 14 suggests that in the presence of storms, increase of DLR emission from the cloud bottom to the surface dominates the change of surface radiation during winter with values as much as 10 times the change of DSR. Hence, the most outstanding variation brought by the storms in the surface radiation comes from increase of DLR, which enhance the air temperature and warms up the ice surface.

We conducted composite analysis for surface sensible and latent heat fluxes (positive is upward) and compared them with climatological field. As shown in Figure 15, the climatological sensible and latent heat fluxes in summer between sea surface and atmosphere are typically small, with values less than 10 W m^{-2}. The negative sensible heat flux over northern Chukchi and most of Beaufort Seas indicates that the atmosphere transfers heat to the surface (Figure 15a). The positive latent heat flux in Figure 15b indicates that heat released by sea ice melting is transferred to the atmosphere from the underlying open water. The negative sensible and latent heat flux anomalies south of 70° N over the thin ice and open water area collocated with the decrease of SST in summer (Figure 16). In winter, the Chukchi and Beaufort Seas are mostly ice-covered and the sea ice cover acts like a blanket between the atmosphere and the underlying seas by preventing the loss of heat and moisture from the ocean to the atmosphere via sensible and latent heat flux. Thus, positive sensible and latent heat fluxes are only shown over the open water areas in both climatological and composite fields (Figure 17). Climatologically, the negative sensible heat flux over the ice-covered surface of DJF is larger than that of JJA, indicating atmosphere transfers more heat to the ice-covered surface in winter. The sensible and latent heat flux slightly decrease but still be positive south of the Bering Strait when storms are over the area. Due to the fact that sea

ice suppresses vertical exchange of sensible and latent heat between the upper ocean and cold atmosphere, no significant difference between the climatology and composite fields are observed in the region (Figure 18).

2.4 Conclusion

The surface environmental conditions, including pressure, 2-meter surface air temperature, 10-meter surface wind, surface radiations and heat fluxes, over the Chukchi and Beaufort Seas are substantially different from climatology of the region with intrusions of intense storms. Storms are classified in two groups with respect to the pathways they entering the region. Seasonal onset of storms has different impact on the area. Winter storms moving from the North Pacific Ocean over the Bering Strait into the Chukchi Sea are typically more intense than the summer storms moving from the East Siberia Sea with respect to the values of central low pressure and maximum wind speed. Both storm types can strongly affect surface radiation.

Changes of sea ice concentration are caused by many processes. Winds can promote sea ice movement and break up the thin sea ice. Clouds can trap longwave radiation and warm up the sea ice surface. Both processes can be affected by the passage of storms. Cloud associated with summer storms moving from the East Siberia side following an eastward track decreases the absorption of solar radiation and have limited warming effect on the surface as the decreases of the surface downward solar radiation outweighs the increase of the surface downward longwave radiation. However, the decrease of the surface air temperature is not noticeable. The sea ice concentration declines in the southern Chukchi and Beaufort Seas, despite the cooling effect of the negative anomalies of the downward shortwave radiation (Figure 21). As shown in Figure 19b, the decrease of sea ice concentration mostly happens over thin ice, which is more easily disrupted by

winds. Thus, we attribute the sea ice decline to the unusually strong and warm southwesterly winds induced by the summer storms.

When storms enter from the south into the Chukchi and Beaufort Seas in winter, the increase of surface downward longwave radiation dominates over a much larger area over the Chukchi Sea causing a higher surface air temperature. There is a coincidence of the spatial patterns of the increase of the surface downward longwave radiation and surface air temperature. The increase of southerly wind locates mostly south of 70°N and the area under the influence of this warm and moist air is much smaller than the area affected by the increase of downward longwave radiation from the cloud. Our hypothesis is that the cloud radiative effect of the winter storms plays a more dominant role than the southerly winds with respect to the increase of the surface air temperature and also the decrease of the sea ice in the Chukchi Sea (Figure 22). We conclude that storm induced downward longwave radiation increase causes sea ice decline over the ice-covered southern Chukchi Seas in winter, while strong wind powered by the intense summer storms attribute to the decrease of sea ice over the thin ice area. Our hypothesis is that as the sea ice cover keeps retreating to the north in recent years over the Bering Strait and southern Chukchi Sea in winter, the strong southerly wind associated with the intense storms from the North Pacific would play a comparable role as the radiative effect in enhancing the air temperature and accelerating the melting of sea ice in the future.

insightful comments and review on this work. We also thank Dr. Jing Zhang of North Carolina A&T State University, who provided valuable information related to the CBHAR data. We would also like to express special thanks to the Project Officer Warren Horowitz at BOEM, who offered excellent recommendations and feedback.

References

Comiso, J. C. (2006): Abrupt decline in the Arctic winter sea ice cover. *Geophys. Res. Lett.*, 33, L18504

Comiso, J. C., C. L. Parkinson, R. Gersten, and L. Stock (2008): Accelerated decline in the Arctic sea ice cover. *Geophys. Res. Lett.*, 35, L01703.

Dee, D. P., Uppala, S. M., Simmons, A. J., Berrisford, P., Poli, P., Kobayashi, S., Andrae, U., Balmaseda, M. A., Balsamo, G., Bauer, P., Bechtold, P., Beljaars, A. C. M., van de Berg, L., Bid- lot, J., Bormann, N., Delsol, C., Dragani, R., Fuentes, M., Geer, A. J., Haimberger, L., Healy, S. B., Hersbach, H., Hólm, E. V., Isaksen, L., Kållberg, P., Köhler, M., Matricardi, M., McNally, A. P., Monge-Sanz, B. M., Morcrette, J.-J., Park, B.-K., Peubey, C., de Rosnay, P., Tavolato, C., Thépaut, J.-N., and Vitart, F. (2011): The ERA-Interim reanalysis: configuration and performance of the data assimilation system, *Q. J. Roy. Meteor. Soc.*, **137**, 553–597.

Graham, R. M., L. Cohen, A. A. Petty, L. N. Boisvert, A. Rinke, S. R. Hudson, M. Nicolaus, and M. A. Granskog (2017), Increasing frequency and duration of Arctic winter warming events, *Geophys. Res. Lett.*, 44, 6974–6983.

Liu F., J. R. Krieger, and J. Zhang (2014): Toward Producing the Chukchi–Beaufort High-Resolution Atmospheric Reanalysis (CBHAR) via the WRFDA Data Assimilation System. *Mon. Wea. Rev*., 142, 788–805.

Perovich, D. K., B. Light, H. Eicken, K. F. Jones, K. Runciman, and S. V. Nghiem (2007): Increasing solar heating of the Arctic Ocean and adjacent seas, 1979–2005: Attribution and role in the ice-albedo feedback, *Geophys. Res. Lett*., 34, L19505,

Pickart, R. S., G. W. K. Moore, D. J. Torres, P. S. Fratantoni, R. A. Goldsmith, and J. Yang (2009): Upwelling on the continental slope of the Alaskan Beaufort Sea: Storms, ice, and oceanographic response, *J. Geophys. Res*., 114, C00A13,

Roeckner, E; Bäuml, G; Bonaventura, L; Brokopf, R; Esch, M; Giorgetta, M; Hagemann, S; Kirchner, I; Kornblueh, L; Manzini, E; Rhodin, A; Schlese, U; Schulzweida, U; and Tompkins, A (2003): The atmospheric general circulation model ECHAM5. Part 1. Model description. Report no. 349, Max-Planck-Institut für Meteorologie (MPI-M).

Screen, J. A., and I. Simmonds (2010): The central role of diminishing sea ice in recent Arctic temperature amplification. *Nature*., 464, 1334–1337.

Serreze, M. C. (1995): Climatological aspects of cyclone development and decay in the Arctic. *Atmos.–Ocean*., 33, 1–23.

Serreze, M. C., and A. P. Barrett (2008): The summer cyclone maximum over the central Arctic Ocean. *J. Clim*., 21, 1048–1065.

Skamarock, W. C., and Coauthors (2008): A description of the Advanced Research WRF version 3. NCAR Tech Note NCAR/TN–4751STR, 113 pp.

Simmonds, I., C. Burke, K. Keay (2008): Arctic climate change as manifest in cyclone behavior. *J. Clim*., 21: 5777-5796.

Simmonds, I., and I. Rudeva (2012): The great Arctic cyclone of August 2012. *Geophys. Res. Lett.*, 39, L23709.

Steele, M., W. Ermold, and J. Zhang (2008): Arctic Ocean surface warming trends over the past 100 years. *Geophys. Res. Lett.*, 35, L02614.

Undén, P; Rontu, L; Järvinen, H; Lynch, P; Calvo, J; Cats, G; Cuxart, J; Eerola, K; Fortelius, C; Garcia-Moya, J A; Jones, C; Lenderlink, G; McDonald, A; McGrath, R; Navascues, B; Woetman Nielsen, N; Ødegaard, V; Rodrigues, E; Rummukainen, M; Rõõm, R; Sattler, K; Hansen Sass, B; Savijärvi, H; Wichers Schreur, B; Sigg, R; The, H; and Tijm, A (2002): HIRLAM-5 Scientific Documentation. Scientific Report. Can be downloaded from http://hirlam.org.

Wendler, G. (1973): Sea ice observation by means of satellite, *J. Geophys. Res.*, 78(9), 1427-1448, 1973.

Woods, C. and R. Caballero (2016): The Role of Moist Intrusions in Winter Arctic Warming and Sea Ice Decline. *J. Clim.*, 29, 4473–4485

Zhang, X., J. E. Walsh, J. Zhang, U. S. Bhatt, and M. Ikeda (2004): Climatology and interannual variability of Arctic cyclone activity, 1948–2002. *J. Clim.*, 17, 2300– 2317.

Zhang, X., J. Zhang, J. Krieger, M. Shulski, F. Liu, S. Stegall, W. Tao, J. You, and B. Potter, (2013): Beaufort and Chukchi Seas Mesoscale Meteorology Modeling Study, Final Project Report. Bureau of Ocean Energy Management, BOEM 2013-0119, 204 pp.

Figures
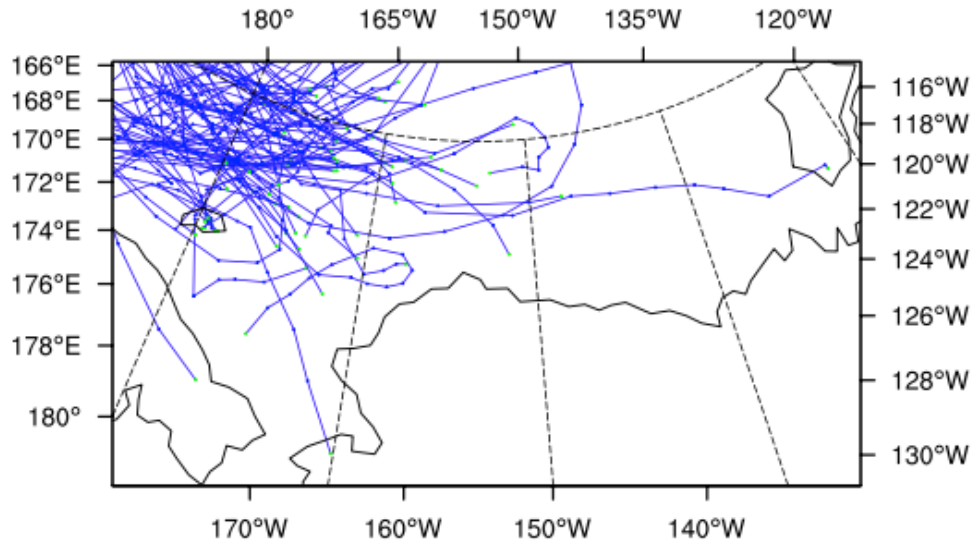
(a)
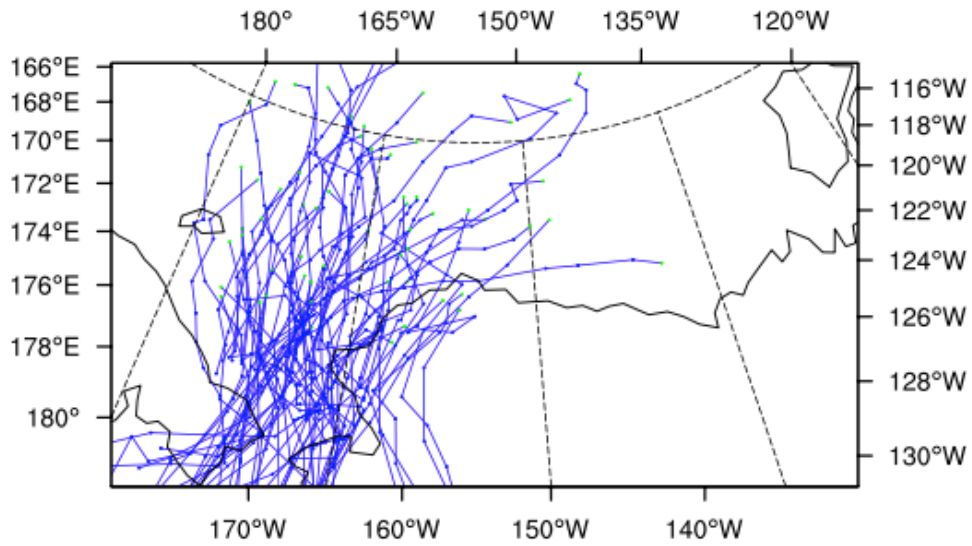
(b)

Figure 1. Storm tracks patterns (a) A total of 85 group 1 storm tracks following eastward and (b) a total of 64 group 2 storm tracks following northward pathway into the Chukchi and Beaufort Seas over the periods from 1979 to 2009.
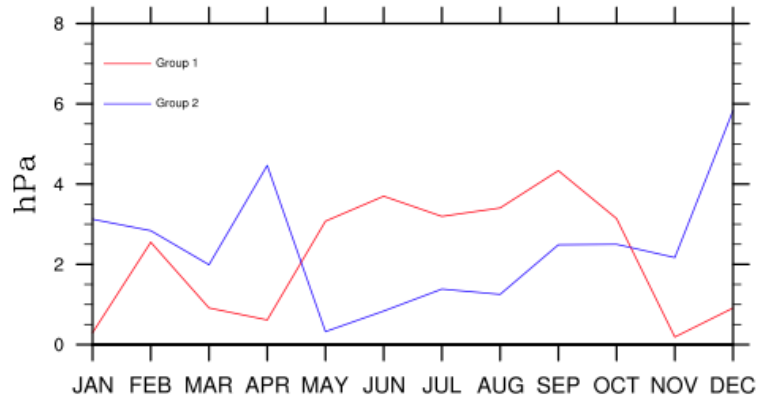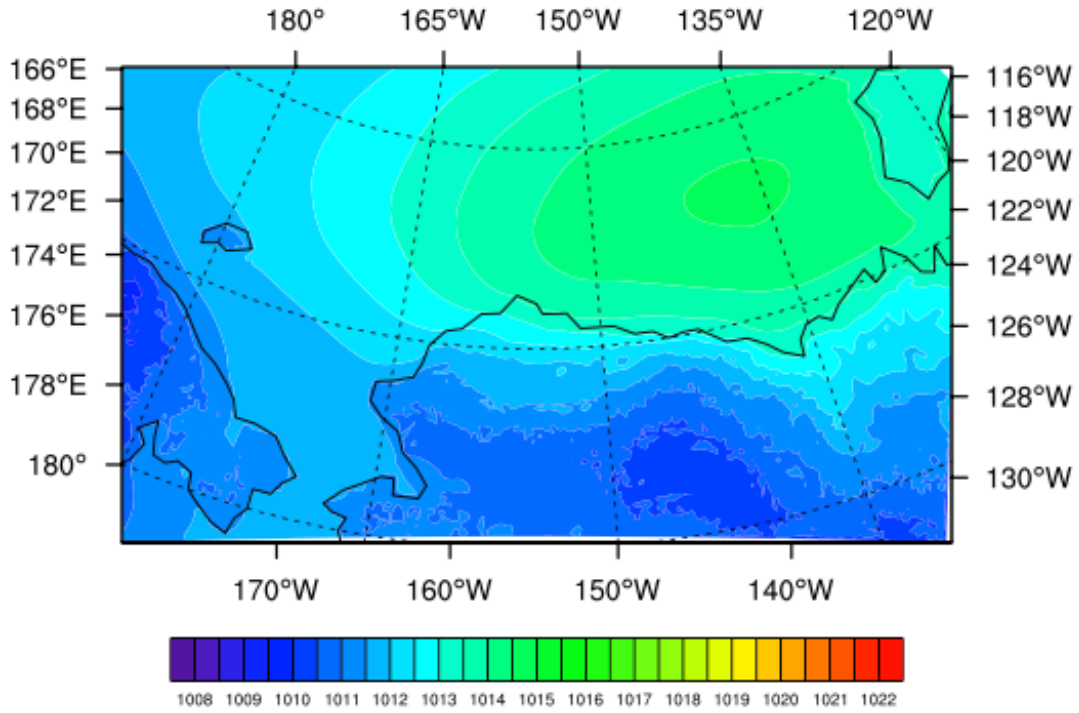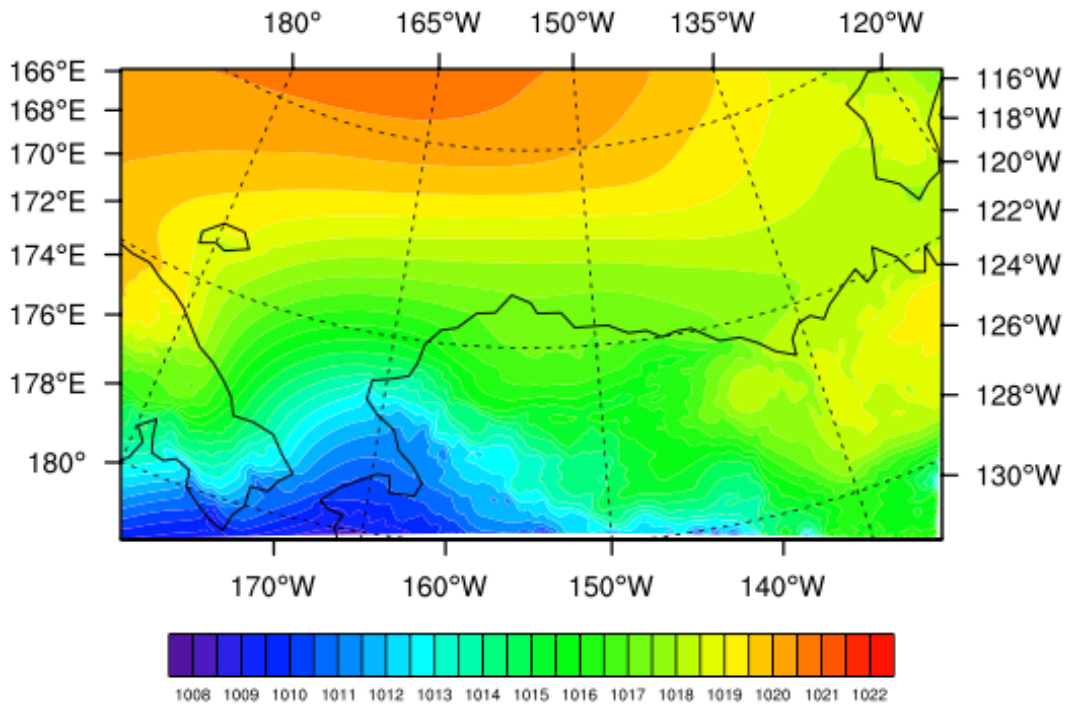
(a)
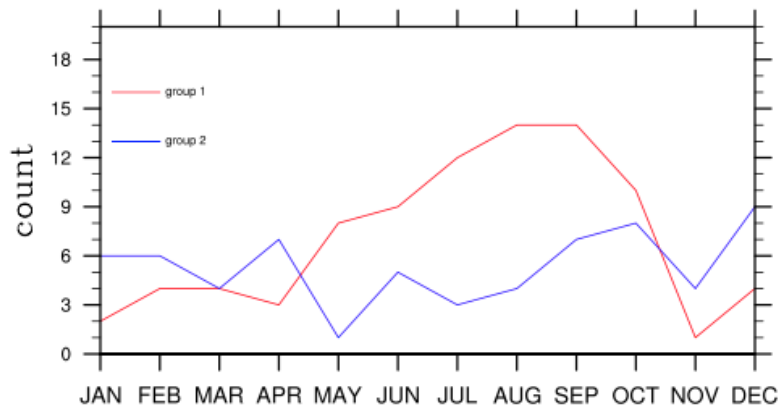
(b)
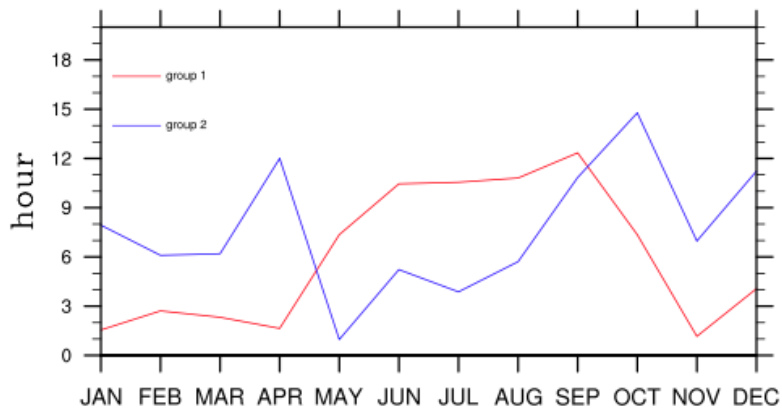
(c)

Figure 2. Storm climatology. Annual cycle of storm (a) intensity, (b) count and (c) duration for group 1 and group 2 storms.
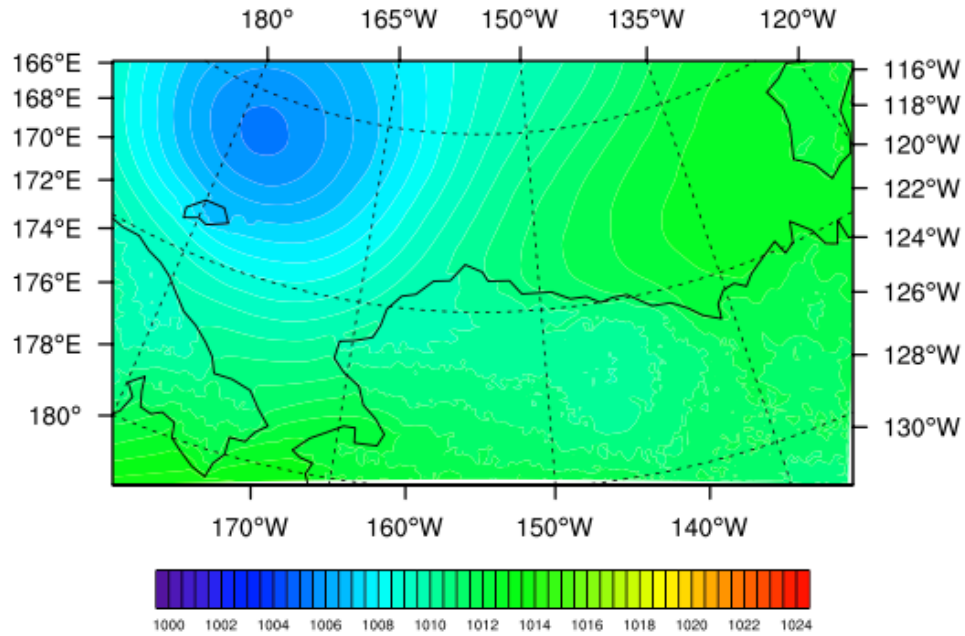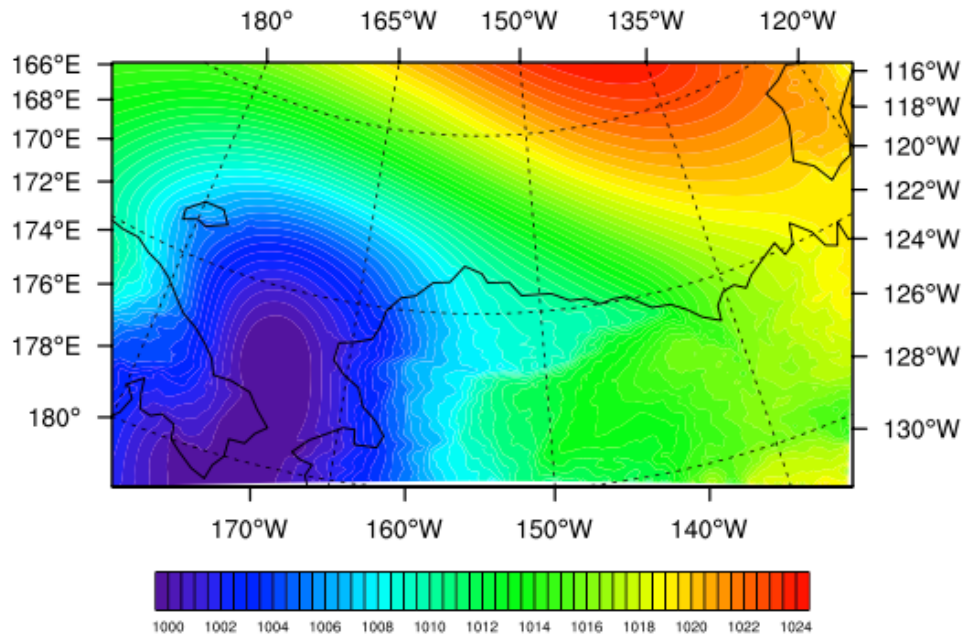
(a)

(b)

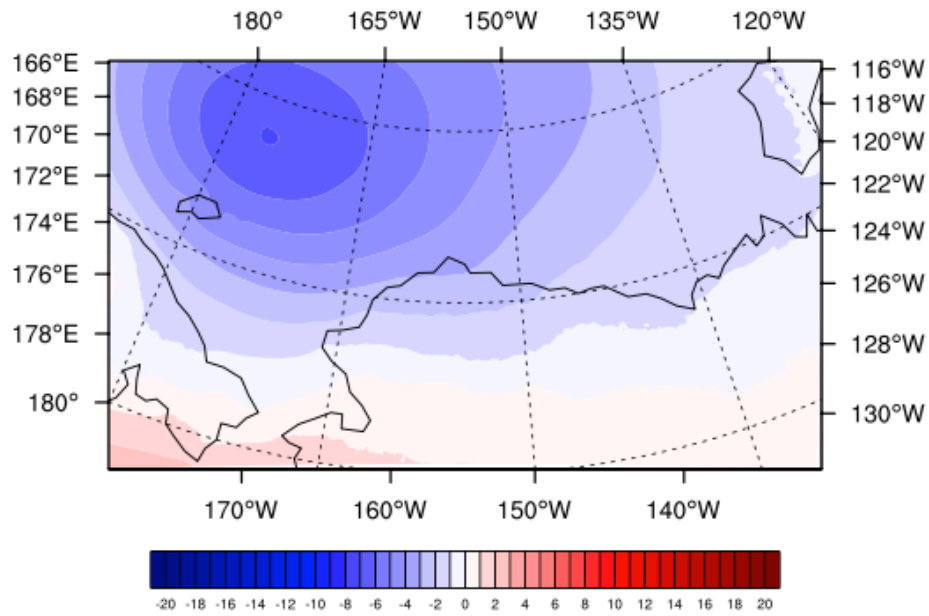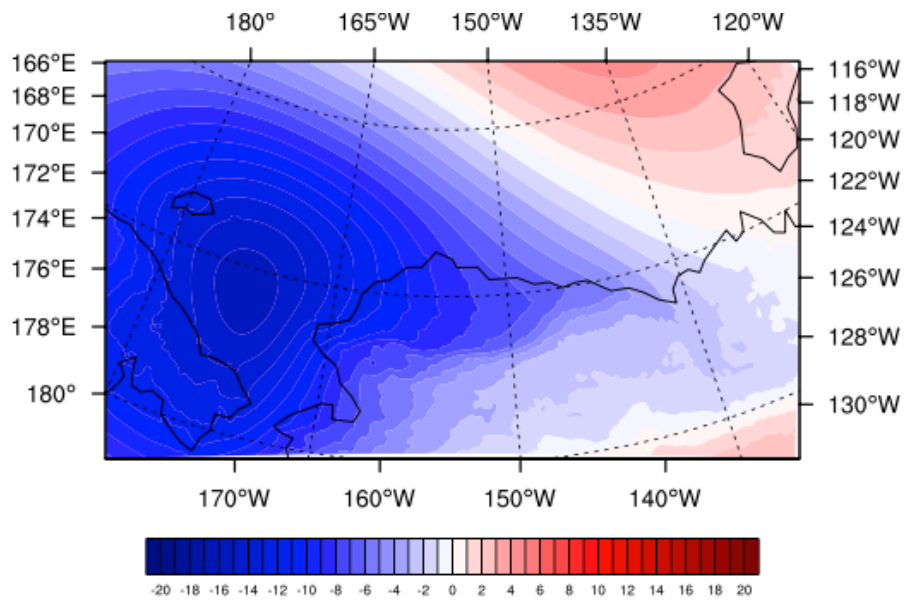Figure 3. Climatological mean SLP (hPa) in (a) JJA and (b) DJF

(a)

(b)

Figure 4. Composite of SLP (hPa) with the presence of (a) group 1 storms in JJA and (b) group 2 storms in DJF
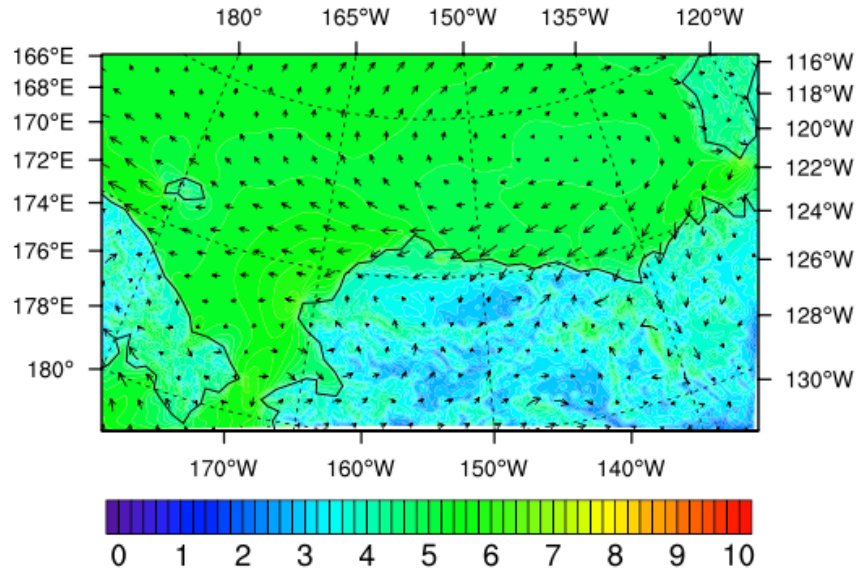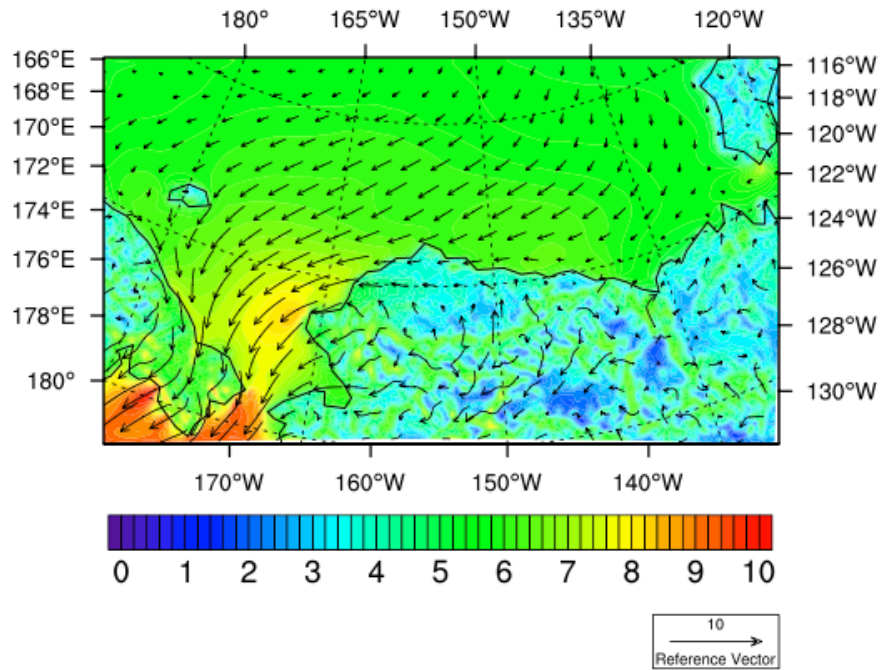
(a)

(b)

Figure 5. Difference between the composite and climatological mean SLP (a) JJA and (b) DJF
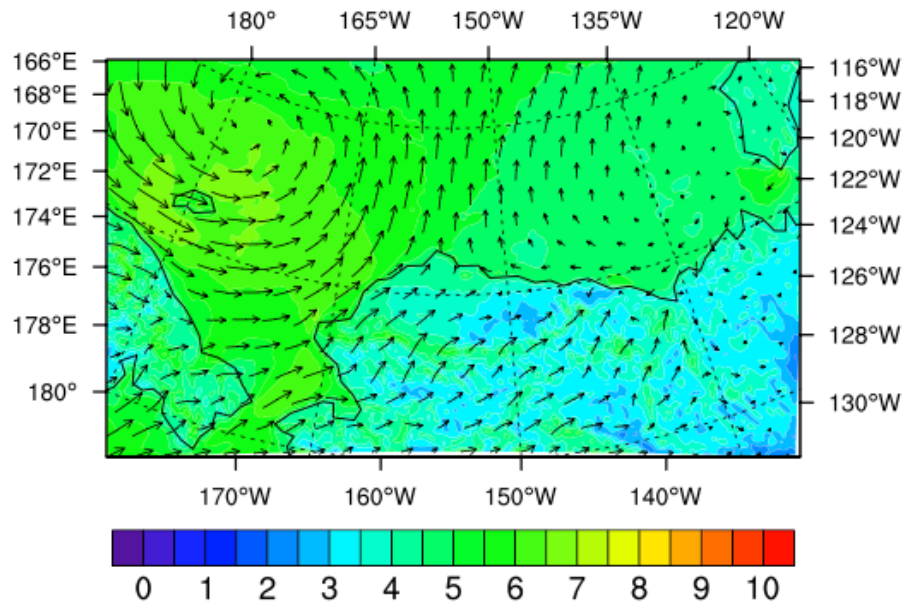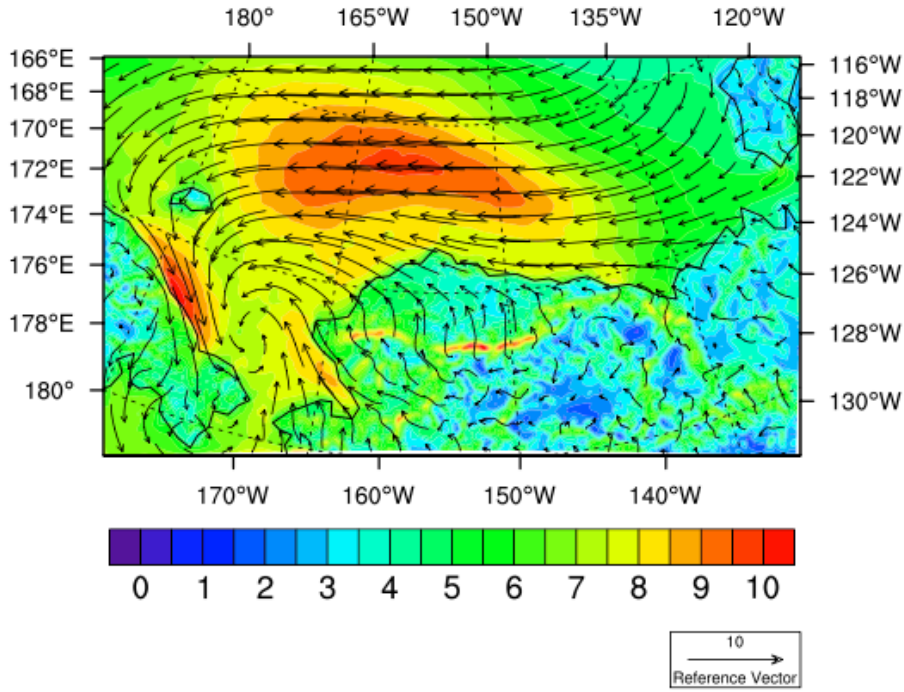
(a)

(b)

Figure 6. Climatological 10-meter surface wind speed and wind direction (a) JJA and (b) DJF. wind speed (shading, m s-1) and wind direction (vectors).
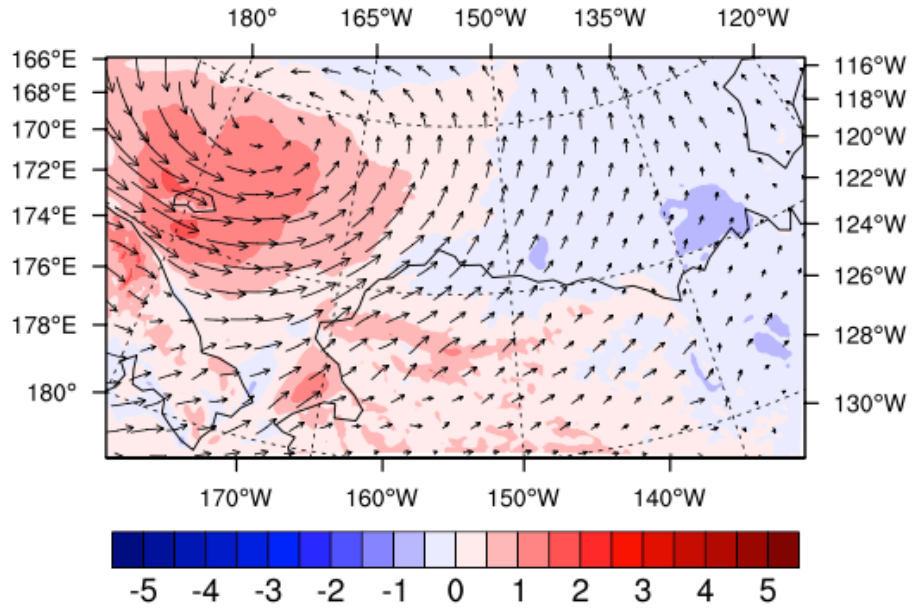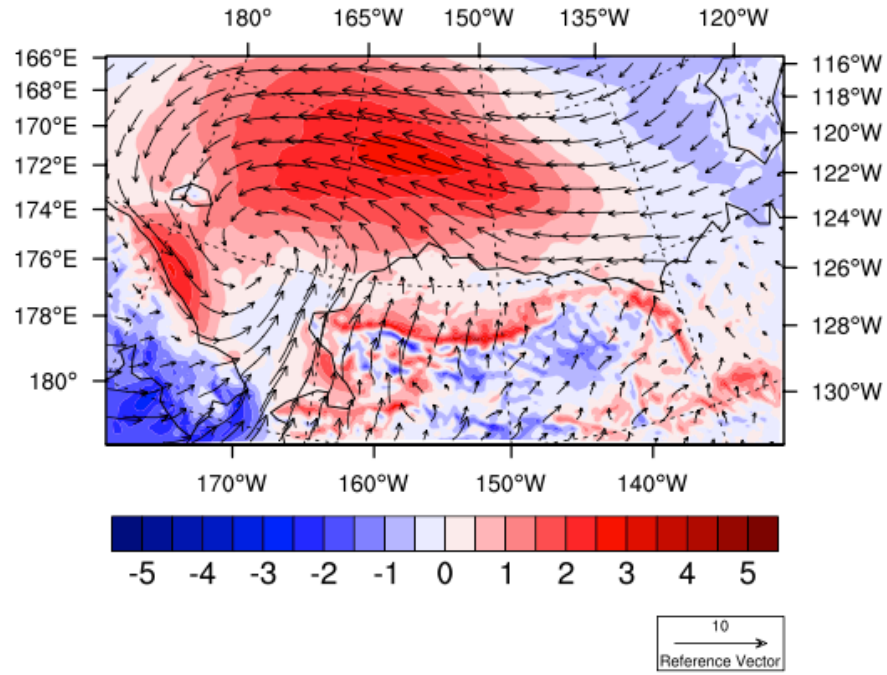
(a)

(b)

Figure 7. Composite 10-meter surface wind speed and wind direction with the presence of (a) group 1 storms in JJA and (b) group 2 storms in DJF
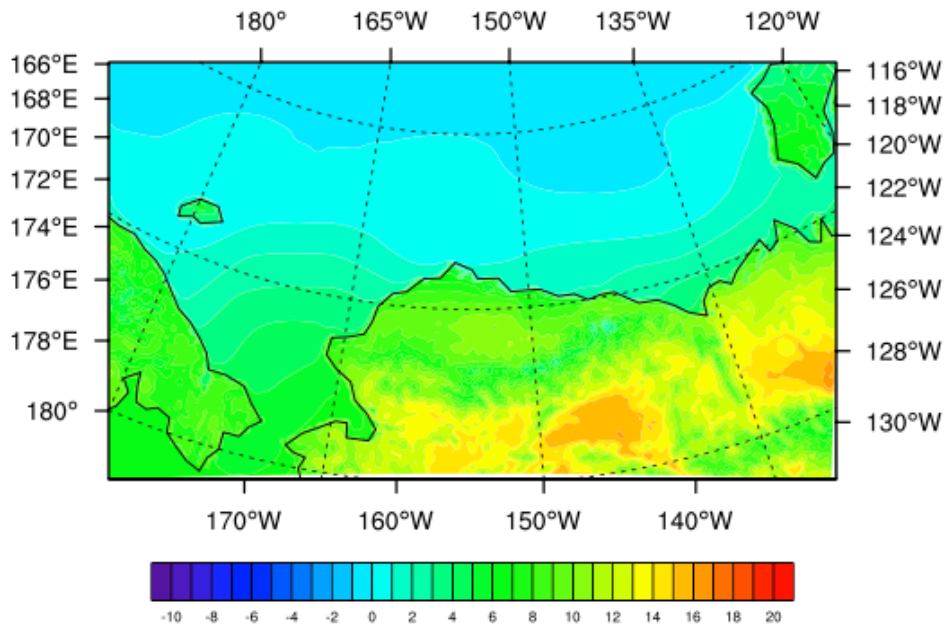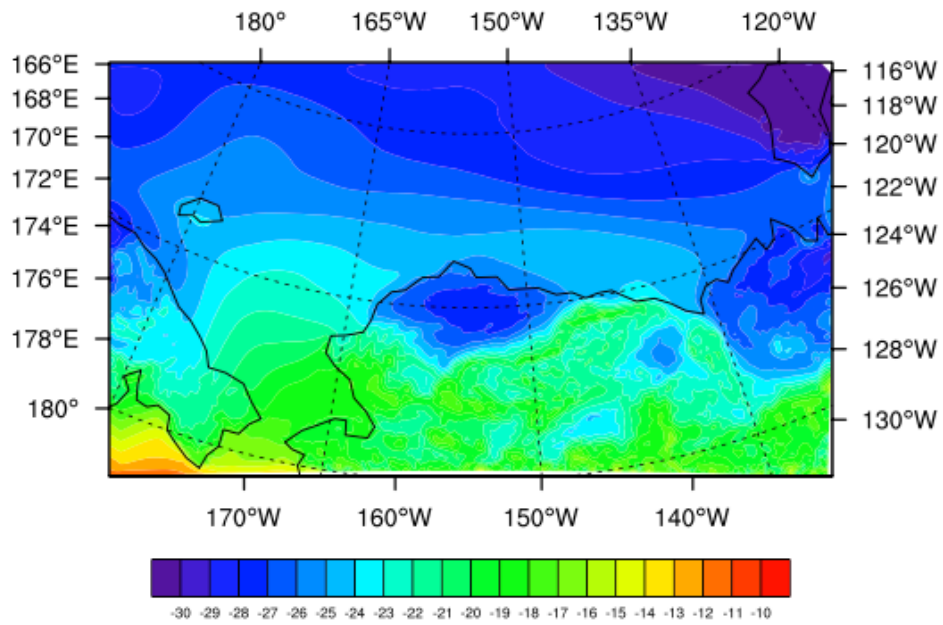
(a)

(b)

Figure 8. Difference between the composite and climatological 10-meter wind speed and wind direction (a) JJA and (b) DJF

(a)

(b)

Figure 9. Climatological mean 2-meter surface air temperature (a) JJA and (b) DJF
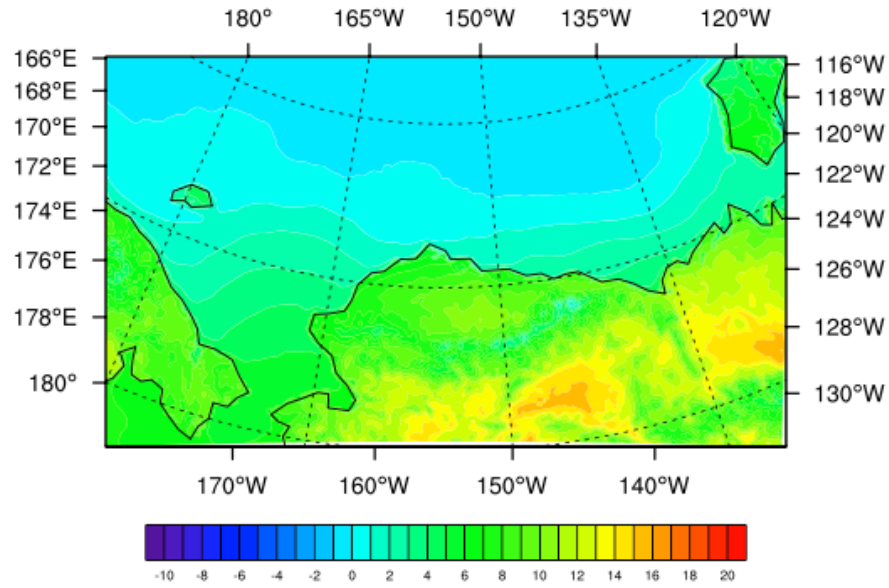
(a)
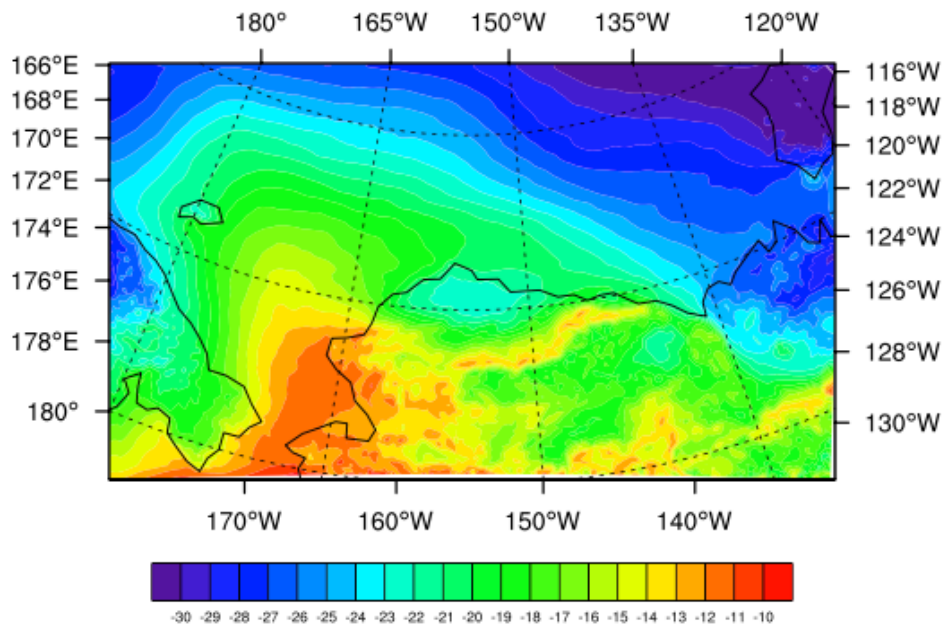
(b)

Figure 10. Composite 2-meter surface air temperature (a) group 1 storms in JJA and (b) group 2 storms in DJF
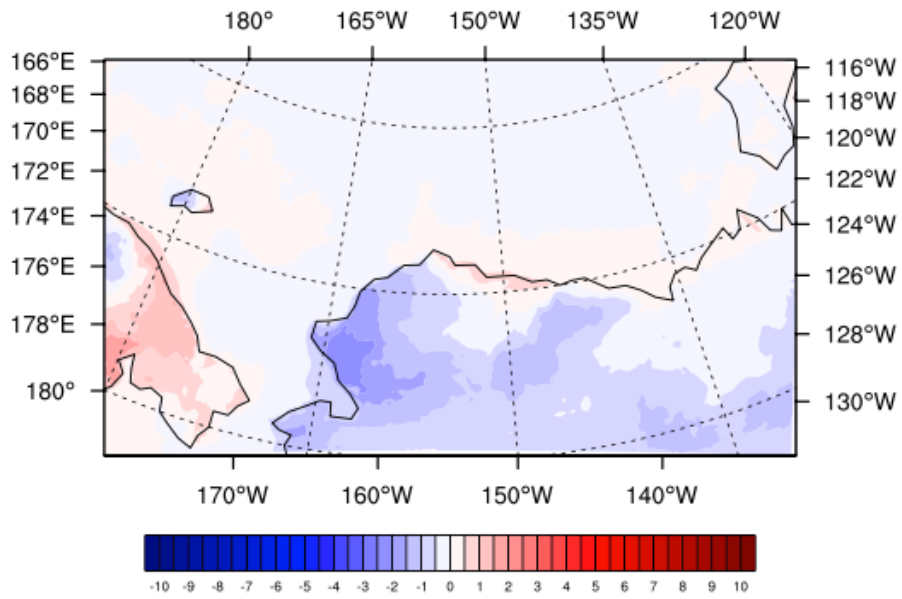
(a)
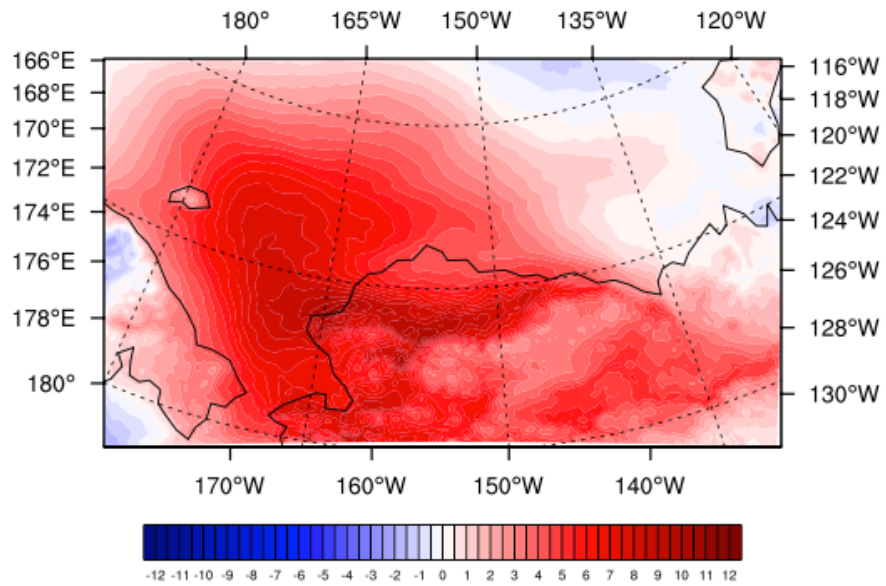
(b)

Figure 11. Difference between the composite and climatological 2-meter surface air temperature for (a) group 1 and (b) group 2 storms
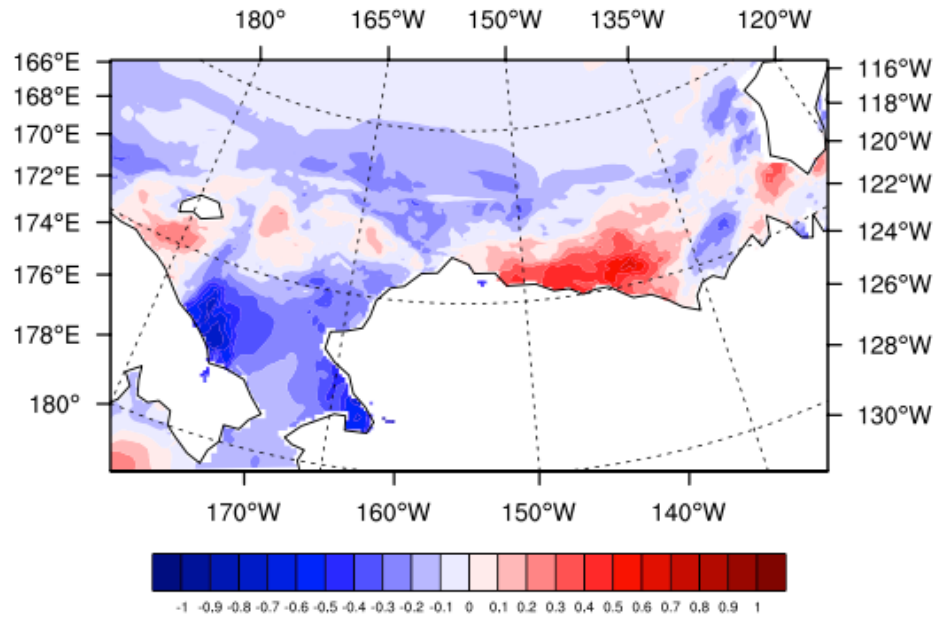
(a)
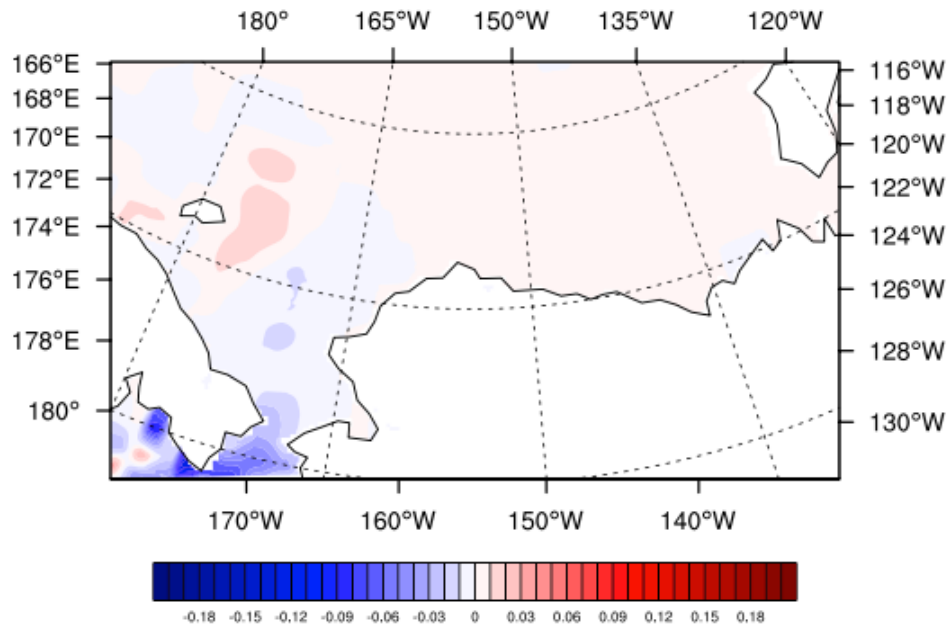
(b)

Figure 12. Difference between the composite and climatological SST (a) JJA and (b) DJF
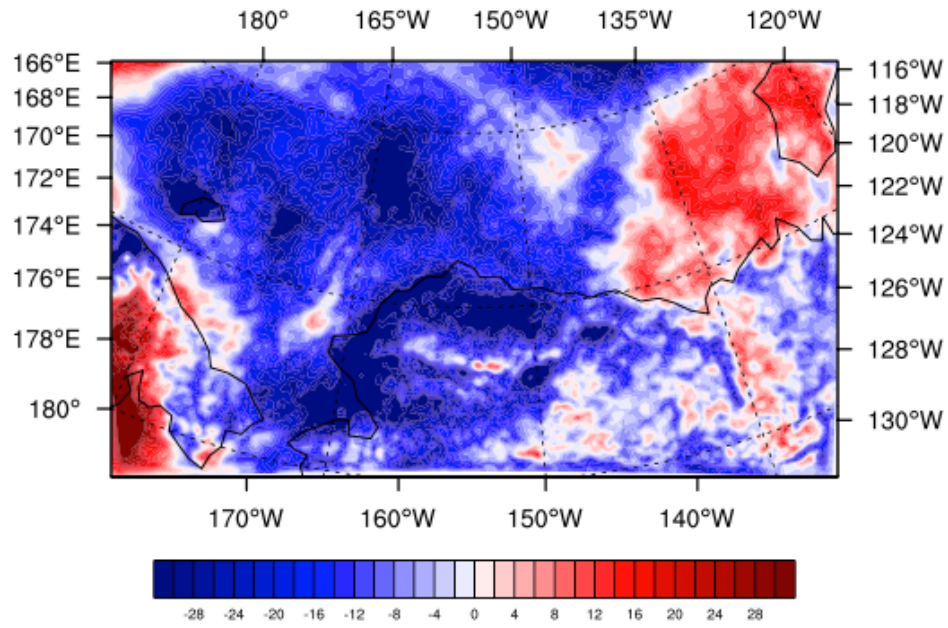
(a)
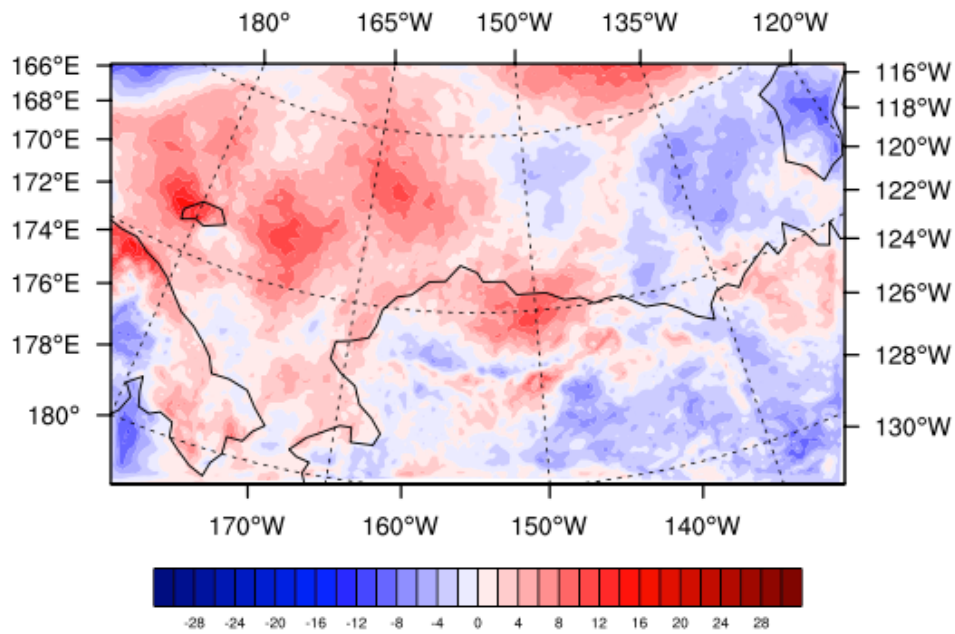
(b)

Figure 13. Difference between the composite and climatological downward (a) shortwave radiation and (b) longwave radiation in JJA
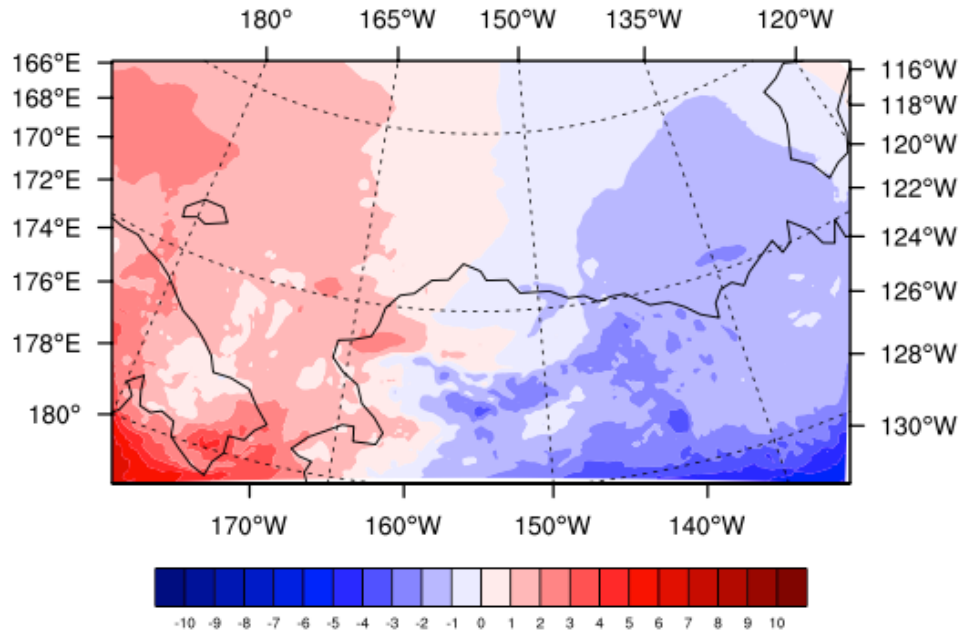
(a)
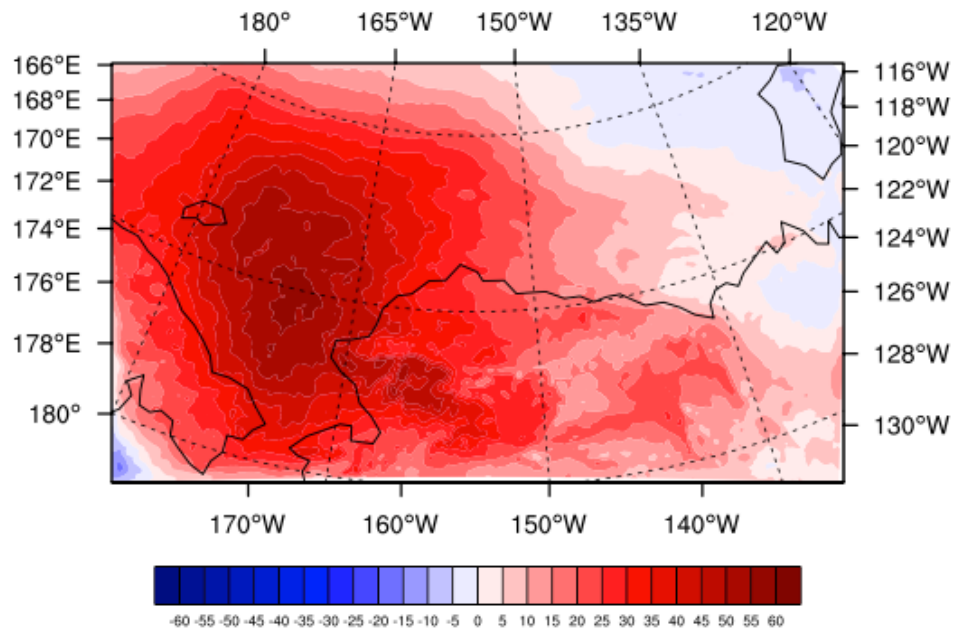
(b)

Figure 14. Difference between the composite and climatological downward (a) shortwave radiation and (b) longwave radiation in DJF
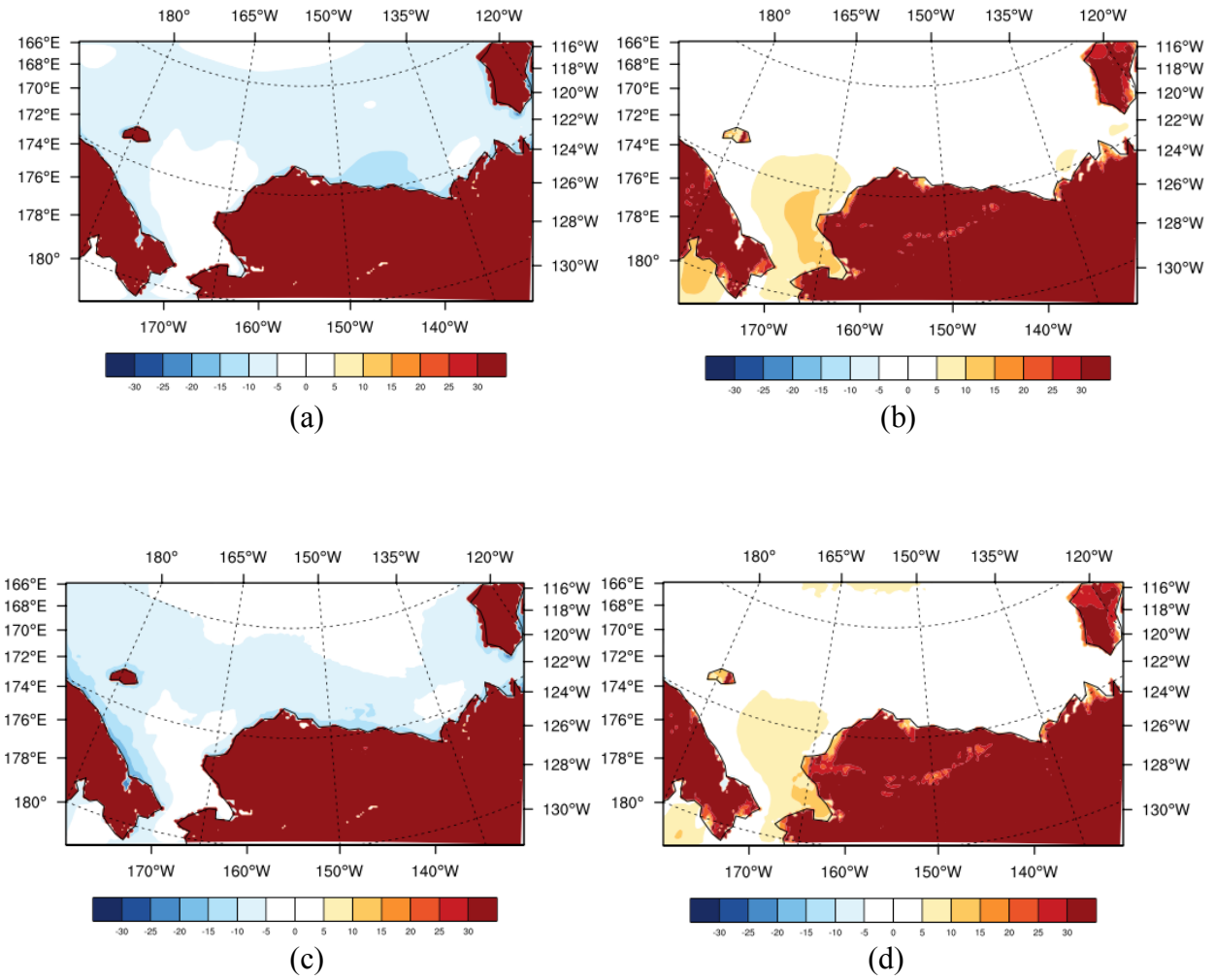
Figure 15. Climatological surface (a) sensible and (b) latent heat flux and composite surface (c) sensible and (d) latent heat flux in JJA (w m^{-2})
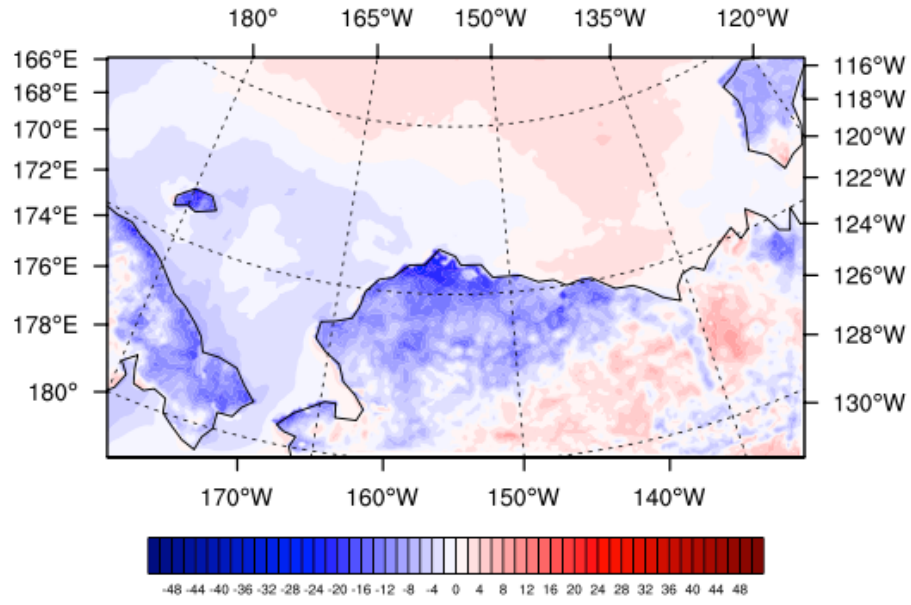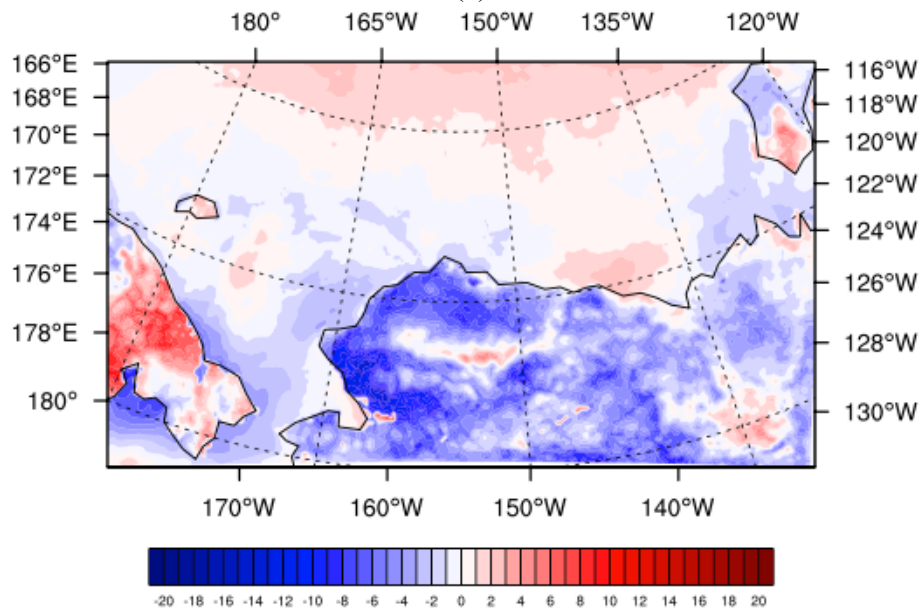
Figure 16. Difference between composite and climatological surface (a) sensible and (b) latent heat fluxes (w m-2) in JJA
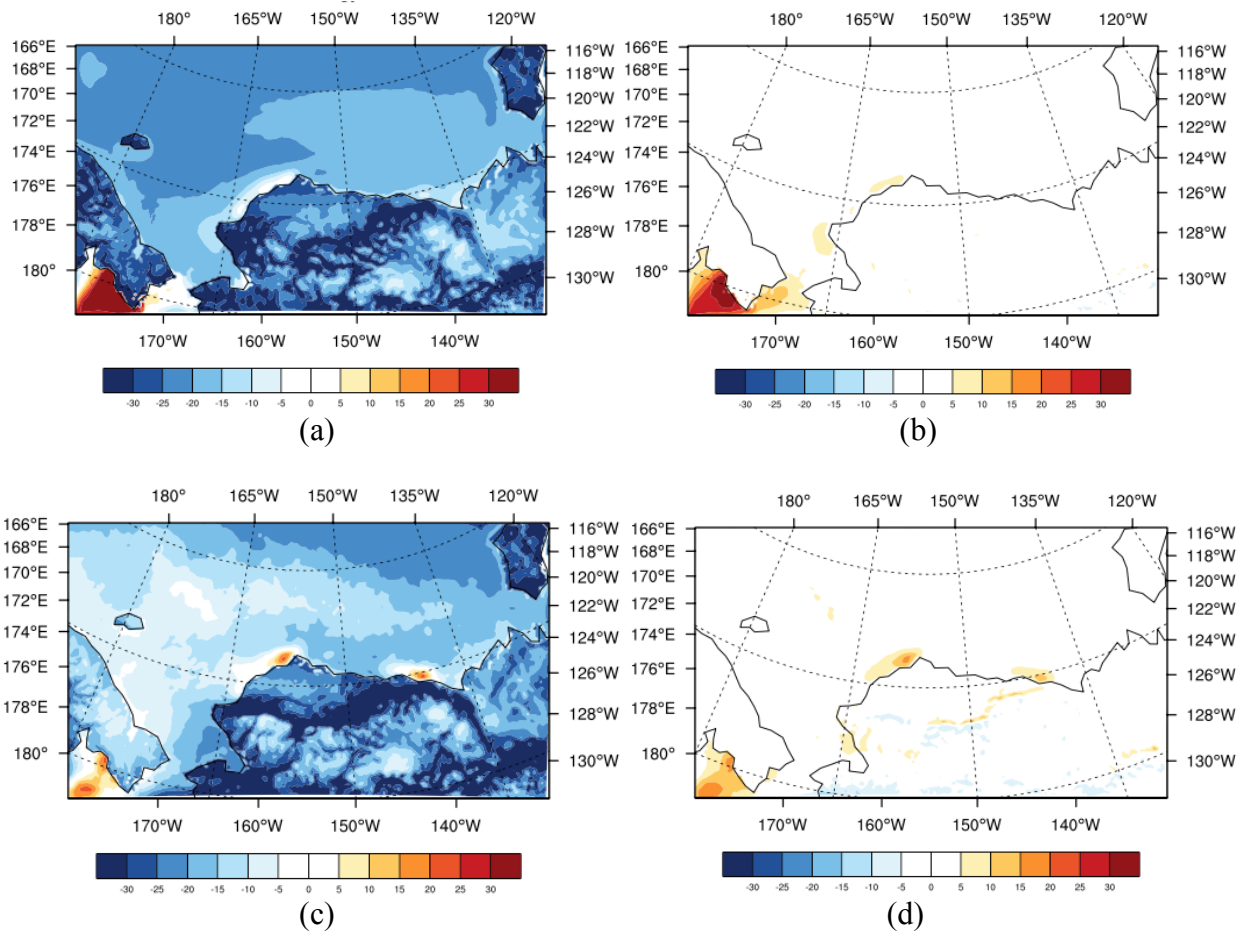
Figure 17. Climatological surface (a) sensible and (b) latent heat fluxes in JJA and Composite surface (c) sensible and (d) latent heat fluxes in DJF (w m^{-2})
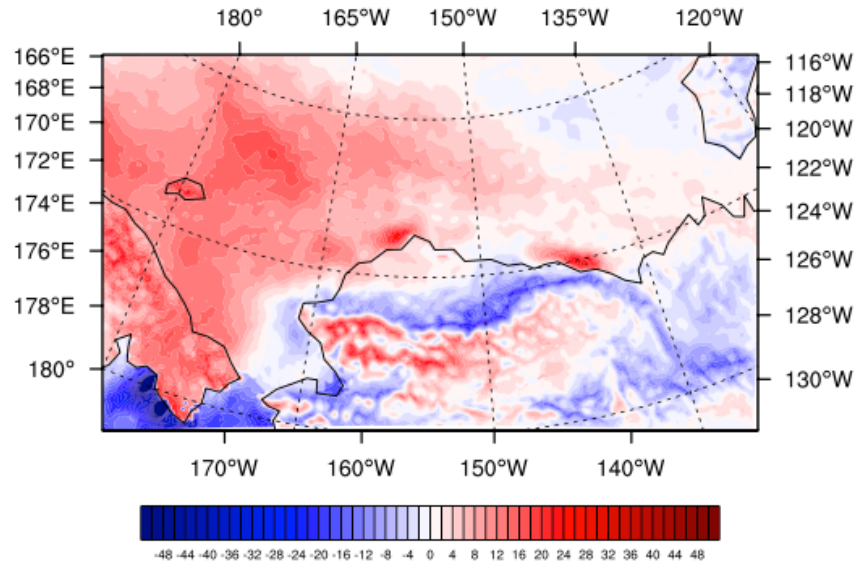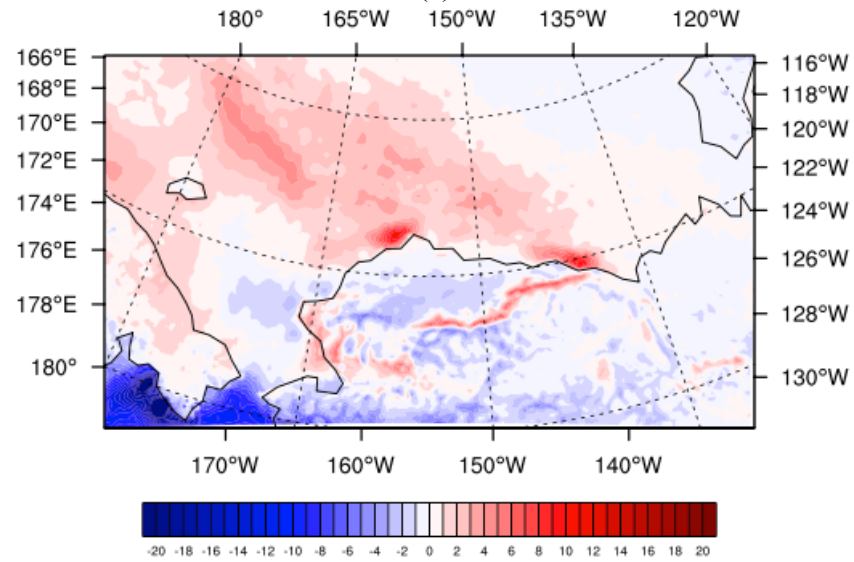
Figure 18. Difference between composite and climatological surface (a) sensible and (b) latent

heat fluxes (w m^{-2}) in DJF
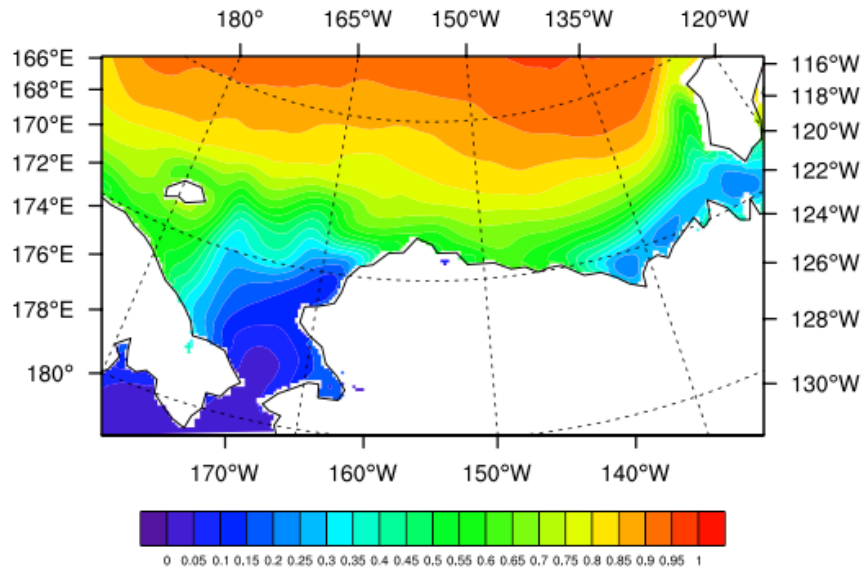
(a)
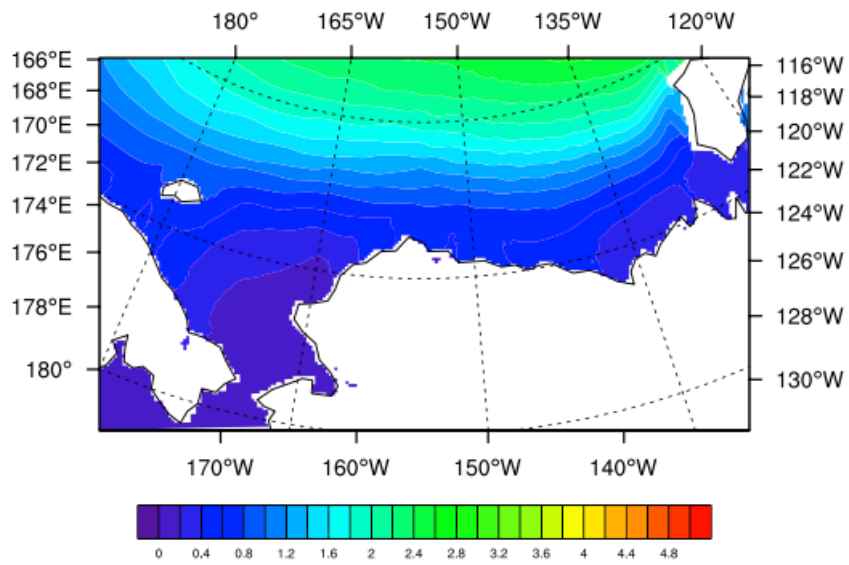
(b)

Figure 19. Climatological (a) sea ice concentration (%) and (b) sea ice thickness (m) in JJA
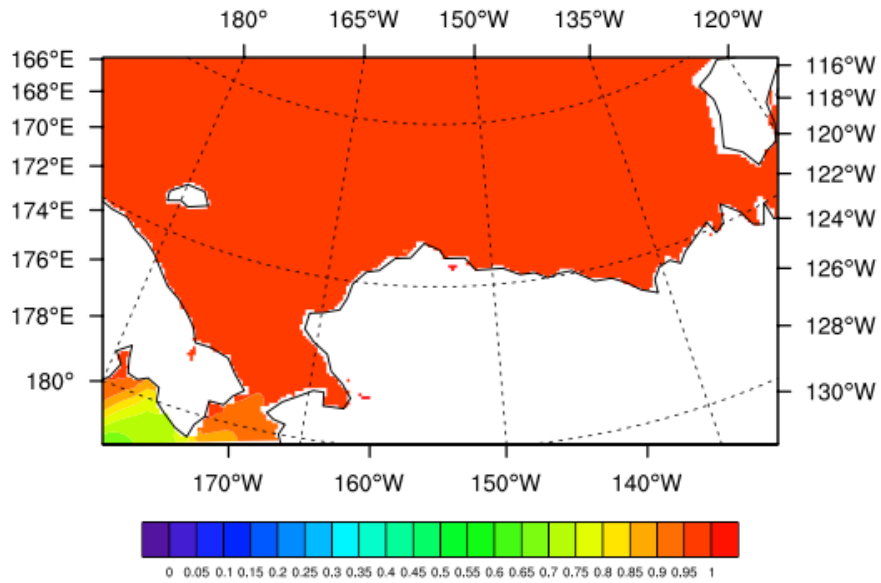
(a)
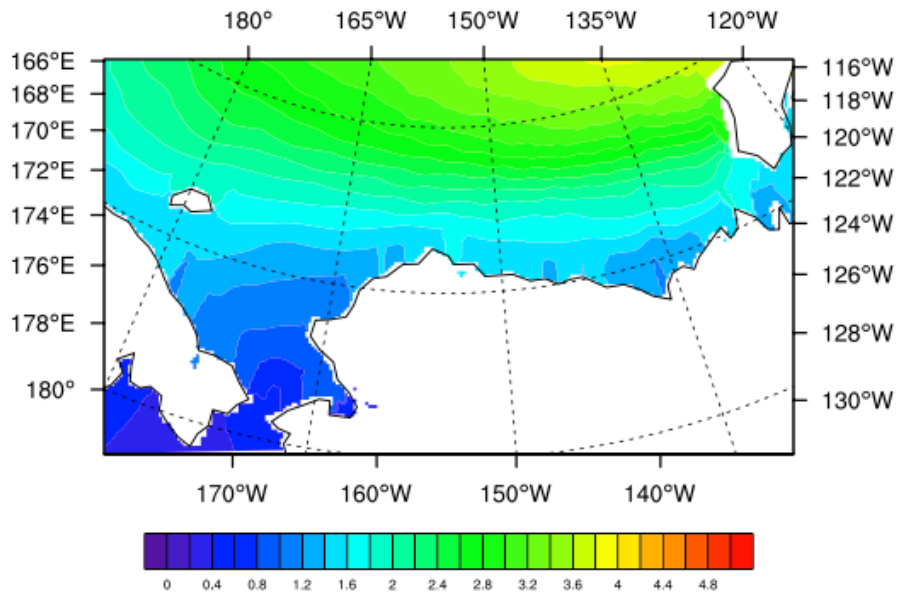
(b)

Figure 20. Climatological (a) sea ice concentration (%) and (b) sea ice thickness (m) in DJF
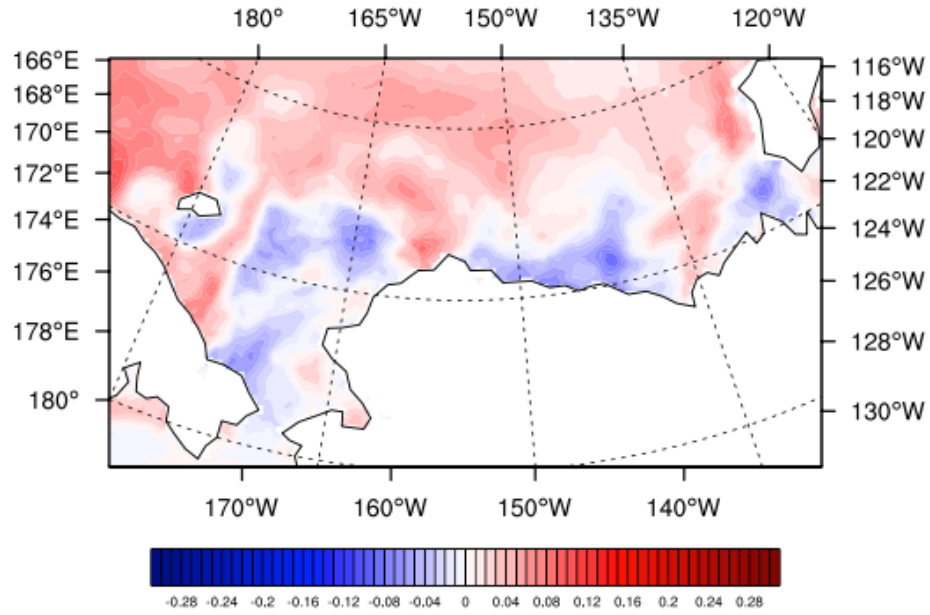
(a)
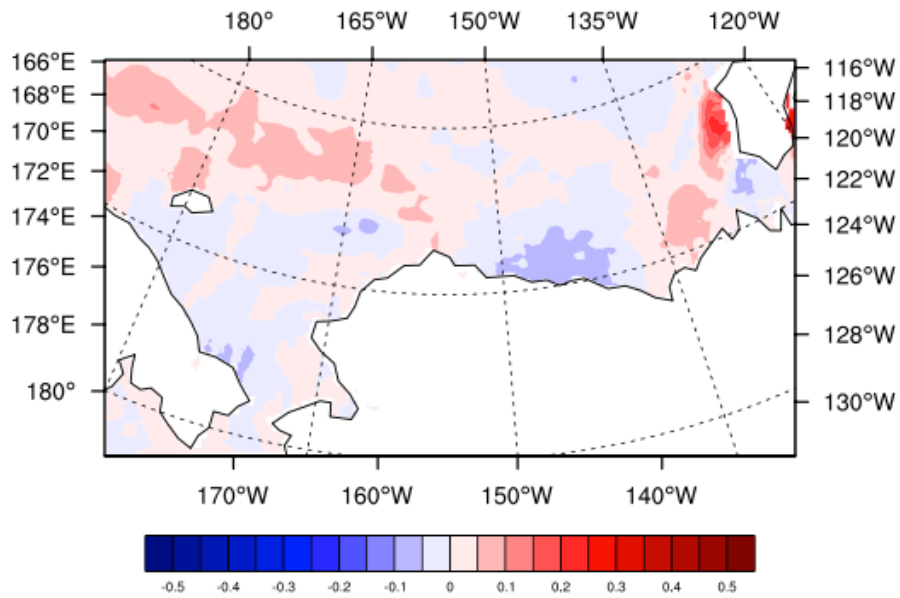
(b)

Figure 21. Difference between composite and climatological (a) sea ice concentration (%) and (b) sea ice thickness (m) in JJA
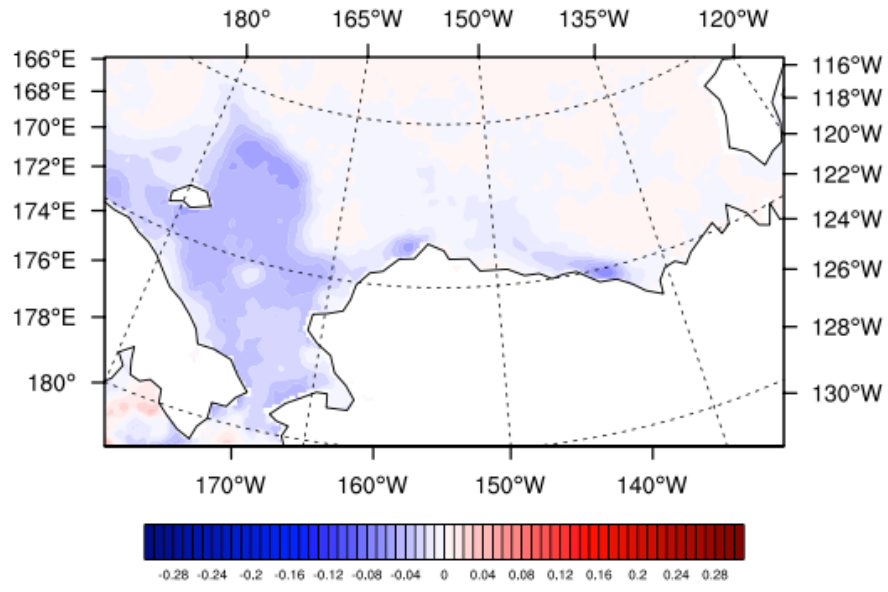
(a)
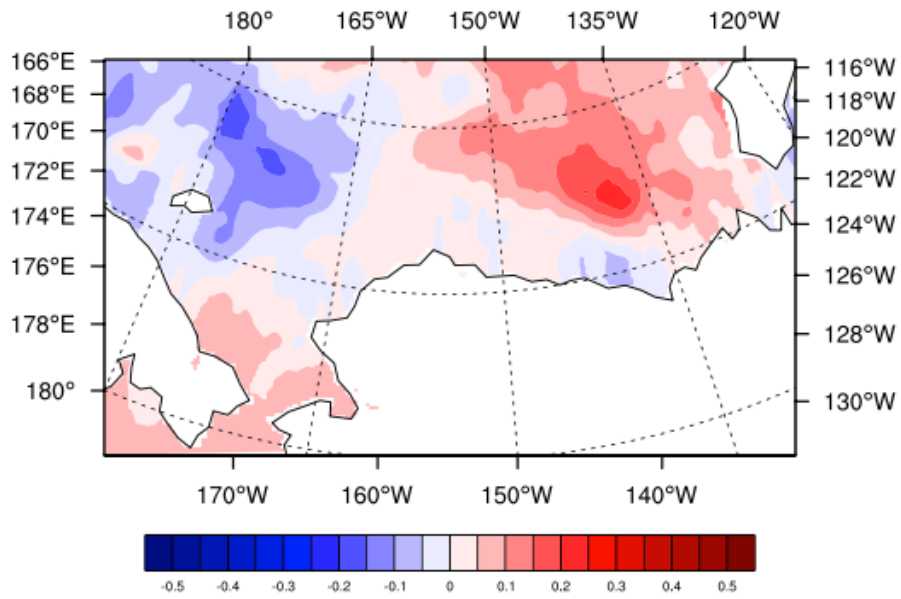
(b)

Figure 22. Difference between composite and climatological (a) sea ice concentration (%) and (b) sea ice thickness (m) in DJF

Chapter 3 The Influence of Arctic Sea Ice on Arctic Storm Activity

Abstract

The impact of the low and high sea ice volume to Arctic atmosphere conditions and synoptic storm systems in autumn are investigated based on the coupled regional climate model HIRHAM-NAOSIM. Ten ensembles of hindcast simulations from 1979 to 2014 are used to study the atmosphere with high and low sea ice volume conditions in the Pacific and Atlantic sectors respectively. The composite analysis results indicate that in the autumn of there is more transfer of heat and moisture fluxes from the open ocean to the atmosphere in the low sea ice years than in the high sea ice years in both the Pacific and Atlantic sectors. The largest increase of upward heat fluxes are over the Laptev, southern Chukchi and Beaufort Seas over the Pacific sector and over the southern Greenland and Barents Seas over the Atlantic sectors. The increased heat fluxes bring energy to warm the near surface atmosphere. The warmer surface temperature then reduces atmospheric stability and leads to enhanced baroclinicity and development of synoptic scale storms. The maximum increase of baroclinicity is over Laptev Sea and Beaufort Sea in the Pacific sector and over Greenland Sea and Barents Sea in the Atlantic sector, which are the locations with largest sea ice decreases. Enhanced baroclinity play a dominant role in the development of intense storm systems. In both sectors, storms in the low sea ice years are more intense than in high sea ice years. More storms occur around the locations where baroclinicity in the low sea ice years. From the MCA analysis, it is shown that sea ice volume anomalies are significantly correlated with synoptic storm counts. Leading modes of covariance between sea ice volume and storm count over Pacific and Atlantic sectors are identified respectively. The results are consistent with our findings in the composite analysis. The first pattern of the MCA in the Pacific sector shows increase of storm

count over the Laptev Sea corresponds to decrease of sea ice volume over that region. The decrease of sea ice volume is associated with decrease of storm count over the northern Greenland Sea.

3.1 Introduction

Arctic sea ice plays an important role in the global climate system and serves as an important insulation between the ocean and the atmosphere (Comiso, 2006). The exchange of heat and moisture between the ocean and the atmosphere is strongly moderated by the sea ice. In recent decades, sea ice is experiencing dramatically decreases (Comiso et al., 2008; Screen and Simmonds, 2010). The decline of sea ice in the Arctic Ocean has allowed the absorption of more solar radiation and hence more warming of the ocean surface (Steele et al. 2008). Negative Arctic sea ice anomalies are associated with increased transfer of heat and moisture from the ocean to the atmosphere. The warm ocean can provide more energy and moisture for the development of baroclinic instability and synoptic storms in the high latitude (Rudeva and Gulev, 2011). The large sea ice extent anomaly during summer 1990 has been linked to a high frequency of cyclone activity over the central Arctic Ocean during spring (Serreze et al., 1995). Linkages between sea ice anomalies and a sharp increase since 1989 in the frequency of cyclones over the central Arctic were also proposed by Maslanik et al. (1996).

In the background of quasi-geostrophic framework, Eady (1949) and Charney (1947) developed the linear theories of baroclinic instability that small-amplitude disturbances on an initially uniform, vertically sheared flow can amplify and make the flow unstable. The basic flow provides the energy for the disturbances to grow. From the thermal wind balance, the vertical shear of the zonal wind is proportional to the temperature gradient, which is proportional to the available potential energy. The disturbances convert the available potential energy from the basic flow to

kinetic energy. Large temperature gradient exits near the marginal zone between sea ice and open ocean and serves as the major source of synoptic scale storm development in the transition season (Inoue et al., 2011). The Atlantic water inflow through the Fram Strait and the Pacific water inflow through the Bering strait are considered as primary oceanic heat source affecting the sea ice variability. The influence of sea ice changes in these two sectors may result in different changes in storm activity in these regions. The storm characteristic in these two regions are also different. It is of interest to know how sea ice change in both Pacific and Atlantic sectors impact the storms occurs in that area. The emphasis of this study is on the variability of storm activity generated under low and high sea ice conditions in Atlantic and Pacific sectors. The goal is to establish an ice-storm relationship on the seasonal scale. Section 2 describes the data sets and method used in the study. Section 3 presents the results from the composite and statistical analysis. Section 4 summaries the study.

3.2 Data and methods

3.2.1 Data

Ten ensemble hindcast simulations from the coupled Arctic regional climate model HIRHAM-NAOSIM (Dethloff et al., 1996, Karcher at al., 2003; Kauker et al., 2003; Rinke et al., 2013) covering the pan-Arctic domain are used for this study. The horizontal resolution is 50 km in the atmosphere (HIRHAM) and 25 km in the ocean (NAOSIM). We use simulated monthly sea ice concentration and sea ice thickness data from the NAOSIM dataset to calculate total autumn (September to November) sea ice volume in the North Pacific domain (85°-70°N, 120°E-120°W) and Atlantic domain (85°-65°N, 100°E-30°W) respectively for each year of the time period 1979-2014 for each ensemble member. Low and high sea ice volume years are selected for both Pacific and Atlantic sectors. Years with sea ice volume anomaly smaller/larger than one standard deviation

is referred to as low and high sea ice years (Figure 23). Composite analysis of sea ice, heat flux, surface wind, temperature and SLP were performed based on high and low sea ice years. Differences in the composite data between high and low sea ice years are investigated for significance using a Student's t-test with 90% confidence level. The potential uncertainty of the total storm counts caused by the lateral boundary conditions in the ten ensemble runs is examined by calculating the mean standard deviation from the ten ensembles based on the total storm counts from 1979 to 2014. The mean standard deviation for the storm count is 34.5, which is small compared to the total storm count.

3.2.2 Methods

We apply and refined the storm identification and tracking algorithm (Zhang et al., 2004) using 6-hourly sea level pressure (SLP) from HIRHAM dataset. Low SLP center is identified if the SLP at the grid point is lower than all surrounding grid points within a 100 km radius. The minimum SLP gradient between the center of the storm and every surrounding grid point must be at least 0.1 hPa per 100 km. Two adjacent storm centers appearing at the same time within 500 km of each other are identified as the same storm system with the lowest storm center as the center of the combined storm system. The life time of storms identified must be at least 12 hours and each individual storm track must be at least 100 km long. The latter criteria eliminate minor disturbances generated by orographic and local heating effects.

Storm intensity and storm count are both investigated in this study. Storm intensity is obtained by calculating the mean values of the difference between the central SLP of the storm and the climatological monthly mean SLP at the corresponding grid points over the storm life time. Intensity of storms in the month are averaged to get monthly mean intensity values. Storm count is defined as the sum of storm low centers in each 100 km by 100 km grid cells over all ten

ensembles in order to increase the sample size for the study. When the storm tracks are passing the boundaries of either the Pacific or the Atlantic sector, instead of taking all the low centers from the whole storm track, only the low centers in the prescribed domain are counted.

We apply the probability distribution functions (PDFs) to storm intensity in both low and high sea ice years. A total of 2838 storms of low sea ice years and 2974 storms of high sea ice years from all ten ensembles in autumn were studied in Pacific sector and a total of 2630 storms of low sea ice years and 2869 storms of high sea ice years were studied in Atlantic sectors. Maximum correlation analysis (MCA) using singular value decomposition (SVD; see Appendix for details) is conducted to find optimal patterns which explain a maximum fraction of the covariance between averaged autumn sea ice volume and storm count distribution over the time period 1979 to 2014 for the Pacific and Atlantic sectors respectively. The first mode from the MCA analysis is examined in this study. The relative importance of the first mode is determined by the fraction of the total covariance explained by the first mode. More details about the SVD technique can be found in Bretherton et al. (1992), Wallace et al. (1992), von Storch and Navarra (1995).

3.3 Results

3.3.1 Composite analysis of low and high sea ice years

Composite sea ice volume in autumn for low and high sea ice years are shown in Figure 24. Over the Pacific sector, sea ice retreats to the northeast part of the Beaufort Sea in low sea ice years while large amount of sea ice covers most of Chukchi and Beaufort and part of East Siberia Sea in the high sea ice years. In high sea ice years over the Atlantic sector, high sea ice volume covers northern Greenland Sea and Barents Sea. The composite difference is calculated using values in low sea ice years minus values in high sea ice years. The largest decrease of sea ice volume is over

southern East Siberia, Chukchi and Beaufort Seas in the Pacific sector and over the northern Greenland Sea over the Atlantic sector.

The most direct impact of sea ice on the atmosphere is through changes in surface latent and sensible heat fluxes transfer. The total of sensible and latent heat flux for low and high sea ice years and their difference are shown in Figure 25. Negative values stand for upward heat flux in this study. In low sea ice years over the Pacific sector (Figure 25a), there is a lot of upward heat fluxes over open water and the marginal zones, indicating a warmer ocean and cold atmosphere in autumn. In high sea ice years (Figure 25c and 25d), as sea ice covers most East Siberia, Chukchi and Beaufort Seas, the upward heat flux region shrinks to southern Laptev Sea and coastal area in northern Alaska. Therefore, enhanced upward heat fluxes occur mostly over East Siberia, southern Chukchi and Beaufort Seas. In Atlantic sector, the largest enhanced upward heat fluxes over the Greenland Sea (Figure 25f). The increase of upward heat fluxes leads to warmer surface temperature over the regions and therefore lower static stability. We hypotheses that this modification would modify the degree of baroclinicity, which relates to synoptic storm activity. The Eady growth rate (Eady, 1949), the growth rate of baroclinic eddies, assesses the baroclinic instability through the vertical gradient in horizonal wind shear in the midlatitude troposphere. Following Hoskins and Valdes (1990), the Eady growth rate is

$$0.31 \frac{f}{N}\left|\frac{dU}{dz}\right|$$

f is the Coriolis parameter, N is the Brunt-Vaisala frequency, $\frac{dU}{dz}$ is the vertical wind shear of the horizontal wind. We calculated the Eady growth rate (day^{-1}) at 750 hPa for both low and high sea ice years to quantitatively assess the growth rate of baroclinic storm systems. Figure 26a shows that the Eady growth rate increases when sea ice volume is lower over East Siberia, northern

Chukchi and Beaufort Seas in the Pacific sector. Over Greenland, Barents and Kara Sea in the Atlantic sector, the Eday growth rate also increases with a larger magnitude (Figure 26b).

The results indicate an increase of baroclinity over those regions and therefore more synoptic storm activity in low sea ice years in both Pacific and Atlantic region are expected. The largest increase of baroclinicity tends to occur over the marginal area between sea ice and open ocean as sea ice retreats. The hypothesis is that the consequences of the increase of baroclinicity would be more storms over Laptev, East Siberia, northern Chukchi and Beaufort Seas in low sea ice years. Figure 27 shows the storm count spatial distribution composite differences between low and high sea ice years for Pacific and Atlantic sectors for autumn months. It is clearly shown that the storm count increase pattern is similar to the Eady growth rate increase pattern over the Pacific and Atlantic sectors. Storm activity increases the most over Greenland Sea in low sea ice years (Figure 27b). This result is consistent with the previous research work from Inoue et al. (2012) stating that lower baroclinicity over the Barents Seas during the low sea ice years could lead to fewer storms activities. Moderate increases of storm activity appear over Kara and Barents Seas. The SLP responses also support our finding as shown in Figure 28. There is significant decrease of SLP over the East Siberia Sea, where more storms occur in the Pacific sector (Figure 28a). However, the region with largest decrease of SLP over the Kara Sea only corresponds to regions with moderate storm increases (Figure 28b).

3.4 Statistical analysis

To examine the impact of low and high sea ice conditions on the intensity of storms over the Pacific and Atlantic sectors, probability density functions (PDFs) of storm intensity was applied to exhibit different storm intensity in low and high sea ice years (Figure 29). Storms in September, November

and December are identified and storm intensity are calculated for low and high sea ice years in the Pacific and Atlantic sectors respectively. Storm from all ten ensembles are used to increase the sample size. Storm intensity is characterized by a normal distribution and is the shape is similar in both low and high sea ice years. In low sea ice years, Atlantic storms tends to be more intense than Pacific storms. Intensity of maximum frequency is slightly higher in low sea ice years than in high ice years over both Pacific and Atlantic sector. The peak frequencies show a decrease over the Pacific and an increase over the Atlantic in the low sea ice years, causing the peak frequencies of storm intensity higher in the high sea ice years over the Pacific and higher in the low sea ice years over the Atlantic. This result supports our finding that enhanced baroclinicity and more intense storms prevail in low sea ice years.

Maximum covariance analysis (MCA) is applied to the simulated monthly autumn sea ice volume and storm count over the Pacific and Atlantic sectors respectively to study the coupling between the two fields. The MCA analysis covers the whole time period from 1979 to 2014 (Figure 30). There is a sea ice dipole in the first MCA patterns over the Pacific sector. The sea ice decrease over the Laptev and East Siberia Sea is accompanied by an increase of storm count over the Laptev Sea. The first MCA patterns over the Pacific sector explain 45% of the squared covariance. The results are similar to our previous findings in the composite analysis. In the Atlantic sector, areas with negative sea ice volume anomalies appear to coincide with positive storm count anomalies. The first MCA patterns explain a large portion (63%) of the squared covariance over the Atlantic sector.

3.5 Summary

The impact of autumn low and high sea ice volumes on Arctic synoptic storm activity are examined in this study using coupled Arctic regional climate model HIRHAM-NAOSIM data from 1979 to 2014. The storm count varies greatly over both Atlantic and Pacific sectors under different sea ice conditions. More intense storms powered by enhanced baroclinicity tend to occur near marginal zone in low sea ice years. To check the change of baroclinicity under different sea ice conditions, we calculated the Eady growth rate. The spatial distribution of positive storm count anomalies is in good agreement with negative SLP anomalies and positive Eady growth rate anomalies. The storm activity is weaker in high sea ice years. Storm count is significantly affected by the sea ice changes in both Pacific and Atlantic sectors. The locations where storm count increase response to sea ice decline the most are also identified in the MCA analysis. The coupled sea ice and storm count patterns are consistent with the results from the composite analysis. Storms count increases most over Laptev Sea, Barents Sea and over the northern Greenland Sea during autumn in the pacific and Atlantic sectors respectively, which are also the locations with significant sea ice decline. The first coupled mode in the Atlantic sector represents that negative sea ice volume anomalies are accompanied by positive storm count anomalies. The sea ice and storm coupling in the Pacific sector is weaker than that found in the Atlantic sector. Overall, the atmospheric feedback depends strongly on where the highest Eady growth rate are located and where the sea ice decreases the most.

References

Bretherton, C. S., C. Smith, and J. M. Wallace (1992): An intercomparison of methods for finding coupled patterns in climate data. *J. Clim*, 5, 541–560.

Comiso, J. C. (2006): Abrupt decline in the Arctic winter sea ice cover. *Geophys. Res. Lett*., 33, L18504

Comiso, J. C., C. L. Parkinson, R. Gersten, and L. Stock (2008): Accelerated decline in the Arctic sea ice cover. *Geophys. Res. Lett*., 35, L01703.

Charney, J. G. (1947): The dynamics of long waves in a baroclinic westerly current. *J. Meteor*., 4, 136–162.

Eady, E. T. (1949): Long waves and cyclone waves. *Tellus*. 1. 33-52.

Dethloff, K., A. Rinke, R. Lehmann, J. H. Christensen, M. Botzet, and B. Machenhauer (1996): Regional climate model of the Arctic atmosphere, *J. Geophys. Res*., 101, 23,401–23,422.

Dorn, W., K. Dethloff, A. Rinke, S. Frickenhaus, R. Gerdes, M. Karcher, and F. Kauker (2007): Sensitivities and uncertainties in a coupled regional atmosphere-ocean-ice model with respect to the simulation of Arctic sea ice, *J. Geophys. Res*.112.

Inoue, J., Hori, M.E. (2011): Arctic cyclogenesis at the marginal ice zone: A contributory mechanism for the temperature amplification. *J. Geophys. Res*, 38, L12502.

Inoue, J., M. E. Hori, and K. Takaya (2012): The role of Barents sea ice in the wintertime cyclone track and emergence of a warm-Arctic cold-Siberian anomaly, *J. Clim*., 25, 2561– 2568.

Karcher, M. J., R. Gerdes, F. Kauker, and C. Köberle (2003): Arctic warming: Evolution and spreading of the 1990s warm event in the Nordic seas and the Arctic Ocean, *J. Geophys. Res*., 108(C2), 3034.

Kauker, F., R. Gerdes, M. Karcher, C. Köberle, and J. L. Lieser (2003): Variability of Arctic and North Atlantic sea ice: A combined analysis of model results and observations from 1978 to 2001, *J. Geophys. Res*., 108(C6).

Maslanink, J. A., Mark C. Serreze and Roger G. Barry (1996): Recent decreases in Arctic summer ice cover and linkages to atmospheric circulation anomalies. *J. Geophys. Res*.

Rinke, A., Dethloff, K. Dorn, W. Handorf, D., Moore, J.C. (2013): Simulated Arctic atmospheric feedbacks associated with late summer sea ice anomalies. *J. Geophys. Res.- Atmos*., 118.

Rudeva I, Gulev S.K. (2011): Composite analysis of North Atlantic extratropical cyclones in NCEP-NCAR reanalysis data. *Mon. Weather Rev*. 139: 1419– 1446.

Screen, J. A., and I. Simmonds (2010): The central role of diminishing sea ice in recent Arctic temperature amplification. *Nature*., 464, 1334–1337.

Serreze, M. C. (1995): Climatological aspects of cyclone development and decay in the Arctic. *Atmos.–Ocean*., 33, 1–23.

Steele, M., W. Ermold, and J. Zhang (2008): Arctic Ocean surface warming trends over the past 100 years. *Geophys. Res. Lett*., 35, L02614.

von Storch, H., and A. Navarra, Eds. (1995): Analyses of Climate Variability - Applications of Statistical Techinques. *Springer*, 334 pp.

Wallace, J. M., C. Smith, and C. S. Bretherton (1992): Singular value decomposition of wintertime sea surface temperature and 500-mb height anomalies. *J. Clim*, 5, 561-576.

Zhang, X., J. E. Walsh, J. Zhang, U. S. Bhatt, and M. Ikeda (2004): Climatology and interannual variability of Arctic cyclone activity, 1948–2002. *J. Clim*., 17, 2300– 2317.

Appendix

Maximum Correlation Analysis (MCA) using Singular Value Decomposition (SVD)

Maximum Correlation Analysis (MCA) is used to find patterns in two space-time datasets which explain a maximum fraction of the covariance between them to study the coupling between the two fields (i.e. sea ice volume field and storm count spatial distribution field).

In this study, we consider two data matrices with same time dimension (36 years from 1979 to 2014) and different spatial dimensions (storm count is calculated based on the HIRHAM 100×110 grids domain; sea ice volume is calculated from the NAOSIM 284×163 grids domain).

One matrix X_{ni} is sea ice volume in the NAOSIM domain, with n stands for total grid points number of sea ice (spatial dimension) and i is the time dimension.

$$X_{ni} = X(i) = X_1(i), X_2(i), \ldots, X_{n1}(i)$$

The other matrix Y_{mi} is storm count in the HIRHAM domain, with m stands for total grid points number of storm count (spatial dimension) and i is the time dimension.

$$Y_{mi} = Y(i) = Y_1(i), Y_2(i), \ldots, Y_{m1}(i)$$

n and m are respectively the number of X and Y measurements at each time. The time dimension is the same for X_{ni} and Y_{mi} $i = 1, 2, \ldots, N$.

$$time: 1 \to N$$

$$n \times N: X = \begin{bmatrix} X_1(1) & \cdots & X_1(N) \\ \vdots & \ddots & \vdots \\ X_n(1) & \cdots & X_n(N) \end{bmatrix} \quad \begin{array}{c} 1 \\ space: \downarrow \\ n \end{array}$$

$$time: 1 \to N$$

$$m \times N: Y = \begin{bmatrix} Y_1(1) & \cdots & Y_1(N) \\ \vdots & & \vdots \\ \vdots & \ddots & \vdots \\ \vdots & & \vdots \\ Y_m(1) & \cdots & Y_m(N) \end{bmatrix} \quad \begin{array}{c} 1 \\ space: \downarrow \\ m \end{array}$$

Both X and Y need to detrend by removing the least squares linear trend.

The mathematical procedure to solve the MCA problem is by using SVD on the covariance matrix C_{XY} formed from the input data matrices X and Y. First, we calculate the $n \times m$ cross-covariance matrix C_{XY} (of dimension n by m) of the two data sets X and Y.

$$C_{XY} = cov(X, Y)$$

$$X: n \times N \qquad\qquad Y^T: N \times m$$

$$= \frac{1}{N} \begin{bmatrix} X_1(1) & \cdots & X_1(N) \\ \vdots & \ddots & \vdots \\ X_n(1) & \cdots & X_n(N) \end{bmatrix} \begin{bmatrix} Y_1(1) & \cdots\cdots & Y_m(1) \\ \vdots & \ddots & \vdots \\ Y_1(N) & \cdots\cdots & Y_m(N) \end{bmatrix} = \frac{1}{N} XY^T$$

$$= \begin{bmatrix} cov(X_1, Y_1) & cov(X_1, Y_r) & cov(X_1, Y_m) \\ cov(X_r, Y_1) & cov(X_r, Y_r) & \vdots \\ cov(X_n, Y_1) & \cdots & cov(X_n, Y_m) \end{bmatrix}$$

Then MCA seeks patterns that maximize the covariance. Next, we need to find pairs of mutually orthogonal patterns (singular vectors) to maximize the covariance, U and V,

$$C_{XY} = U\Sigma V^T$$

Let u be an arbitrary unit column n-vector representing a pattern in the X matrix and v be an arbitrary unit column m-vector representing a pattern in the Y matrix. u are the columns of the $n \times n$ matrix U and the v are the columns of the $m \times m$ matrix V. The column space U gives us

the structure vectors of X and the column space V gives us the structure vectors of Y that optimally explain the covariance between the two fields X and Y. Each pair of singular vectors is a mode of covriability between the two fields X and Y.

Now we have $u_1, \dots, u_r$ is an orthonormal basis for the column space. $u_{r+1}, \dots, u_n$ is an orthonormal basis for the left nullspace $N(C_{XY}^T)$. $v_1, \dots, v_r$ is an orthonormal basis for the row space. $v_{r+1}, \dots, v_n$ is an orthonormal basis for the nullspace $N(C_{XY})$. The covariance matrix C_{XY} can be diagonalized by these basis vectors.

$$C_{XY} = U\Sigma V^T = u_1\sigma_1 v_1{}^T + \cdots + u_r\sigma_r v_r{}^T$$

u_1 and v_1 are the structures in X and Y that vary together and are parallel to the strongest part of the covariance. u_2 and v_2 also vary together and they explain the next strongest covariability. Each of them is orthogonal to the previous corresponding vector. The singular vectors are nondimensional. There are r singular values, denoted by $\sigma_1, \dots, \sigma_r$. SVD analysis maximizes the fraction of the squared covariance explained by the leading modes.

We now only consider the first mode for simplicity. If singular vectors u_1 explains the largest covariability in the covariance matrix, then the resemblance between u_1 and X at a given time step i can be quantified as the projection of data $X(i)$ onto singular vector u_1.

At time step $i = 0$, the projection of the original data X on to the singular vector u_1 is

$$X(0)^T \cdot u_1$$

At time step $i = 1$, the projection of the original data X on to the singular vector u_1 is

$$X(1)^T \cdot u_1$$

At time step $i = i$, the projection of the original data X on to the singular vector u_1 is

$$X(i)^T \cdot u_1$$

Therefore, the time series of the pattern associated with the first SVD mode u_1, is

$$a_1(i) = X(0)^T \cdot u_1, \; X(1)^T \cdot u_1, \dots, X(i)^T \cdot u_1$$

This time series describes the temporal evolution of the projection of original data on the first mode u_1.

Similarly, if singular vectors v_1 explains the largest covariability in the covariance matrix, then the resemblance between v_1 and Y at a given time step i can be quantified as the projection of data $Y(i)$ onto singular vector v_1.

At time step $i = 0$, the projection of the original data Y on to the singular vector v_1 is

$$Y(0)^T \cdot v_1$$

At time step $i = 1$, the projection of the original data Y on to the singular vector v_1 is

$$Y(1)^T \cdot v_1$$

At time step $i = i$, the projection of the original data Y on to the singular vector v_1 is

$$Y(i)^T \cdot v_1$$

Therefore, the time series of the pattern associated with the first SVD mode v_1, is

$$b_1(i) = Y(0)^T \cdot v_1, \; Y(1)^T \cdot v_1, \dots, Y(i)^T \cdot v_1$$

The time series describe the temporal evolution of the projection of original data on the first mode v_1.

For the first mode, we have time series

$$a_1(i) = X(0)^T \cdot u_1, \; X(1)^T \cdot u_1, \dots, X(i)^T \cdot u_1$$

$$b_1(i) = Y(0)^T \cdot v_1, \; Y(1)^T \cdot v_1, \dots, Y(i)^T \cdot v_1$$

For the second mode, we have time series

$$a_2(i) = X(0)^T \cdot u_2, \; X(1)^T \cdot u_2, \dots, X(i)^T \cdot u_2$$

$$b_2(i) = Y(0)^T \cdot v_2, \; Y(1)^T \cdot v_2, \dots, Y(i)^T \cdot v_2$$

Similarly, for the i mode, we have time series

$$a_r(i) = X(0)^T \cdot u_r, \ X(1)^T \cdot u_r, \dots, X(i)^T \cdot u_r$$

$$b_r(i) = Y(0)^T \cdot v_r, \ Y(1)^T \cdot v_r, \dots, Y(i)^T \cdot v_r$$

$a_r(i)$ is left coefficients, also called left SVD scores and $b_r(i)$ is right coefficient, also called right SVD scores. $a_r(i)$ and $b_r(i)$ have the same units as the corresponding original data sets X and Y. We projected the original data sets $X(i)$ and $Y(i)$ on to the singular vectors u_1 and v_1 to find the corresponding paired expansion coefficients (time series that describe the temporal evolution of the first mode).
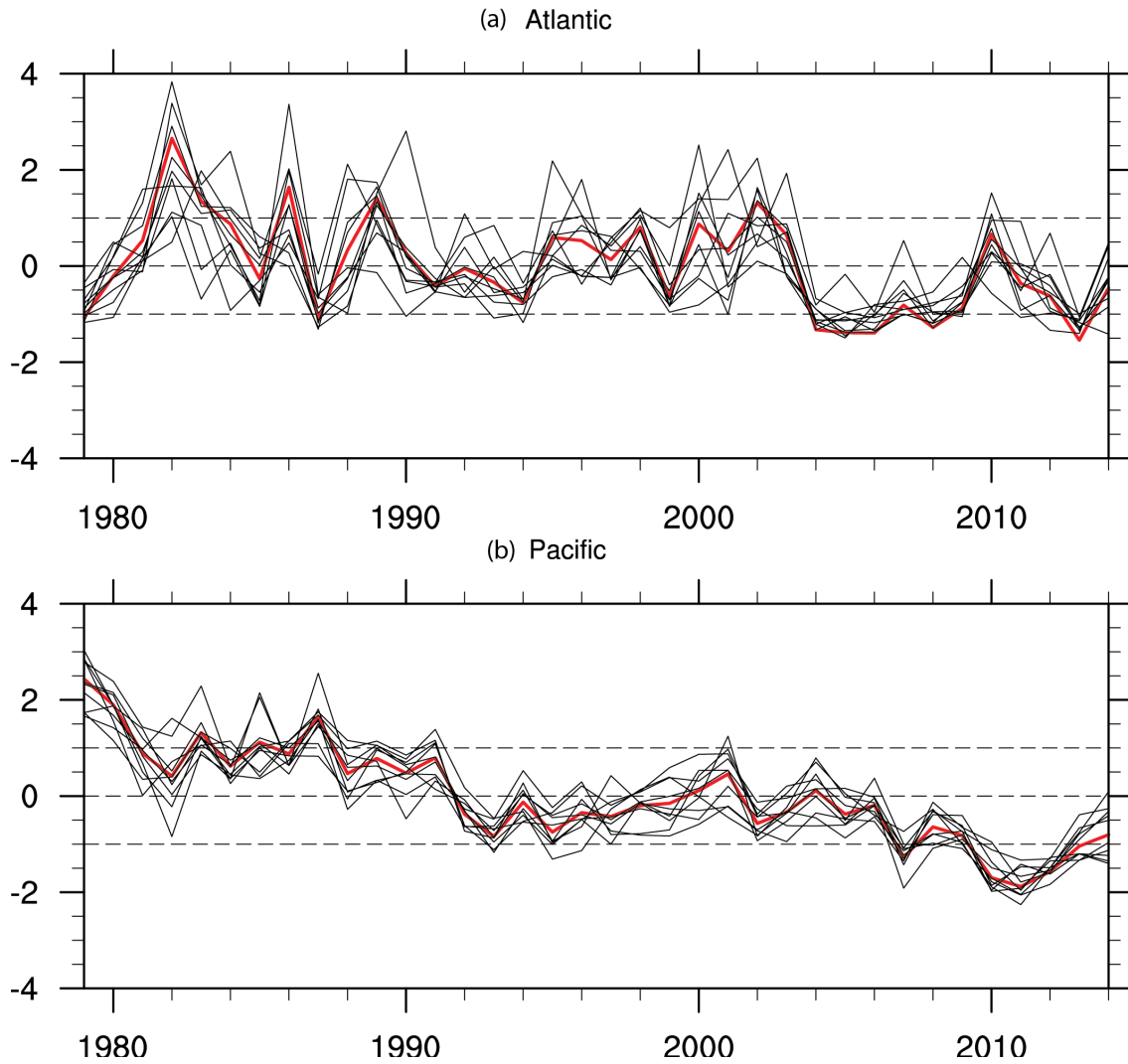
Figure 23. Time series of simulated autumn sea ice volume anomalies. The red line represents the ensemble mean and the ten black lines represent the ensembles. The dash lines are one standard deviation lines
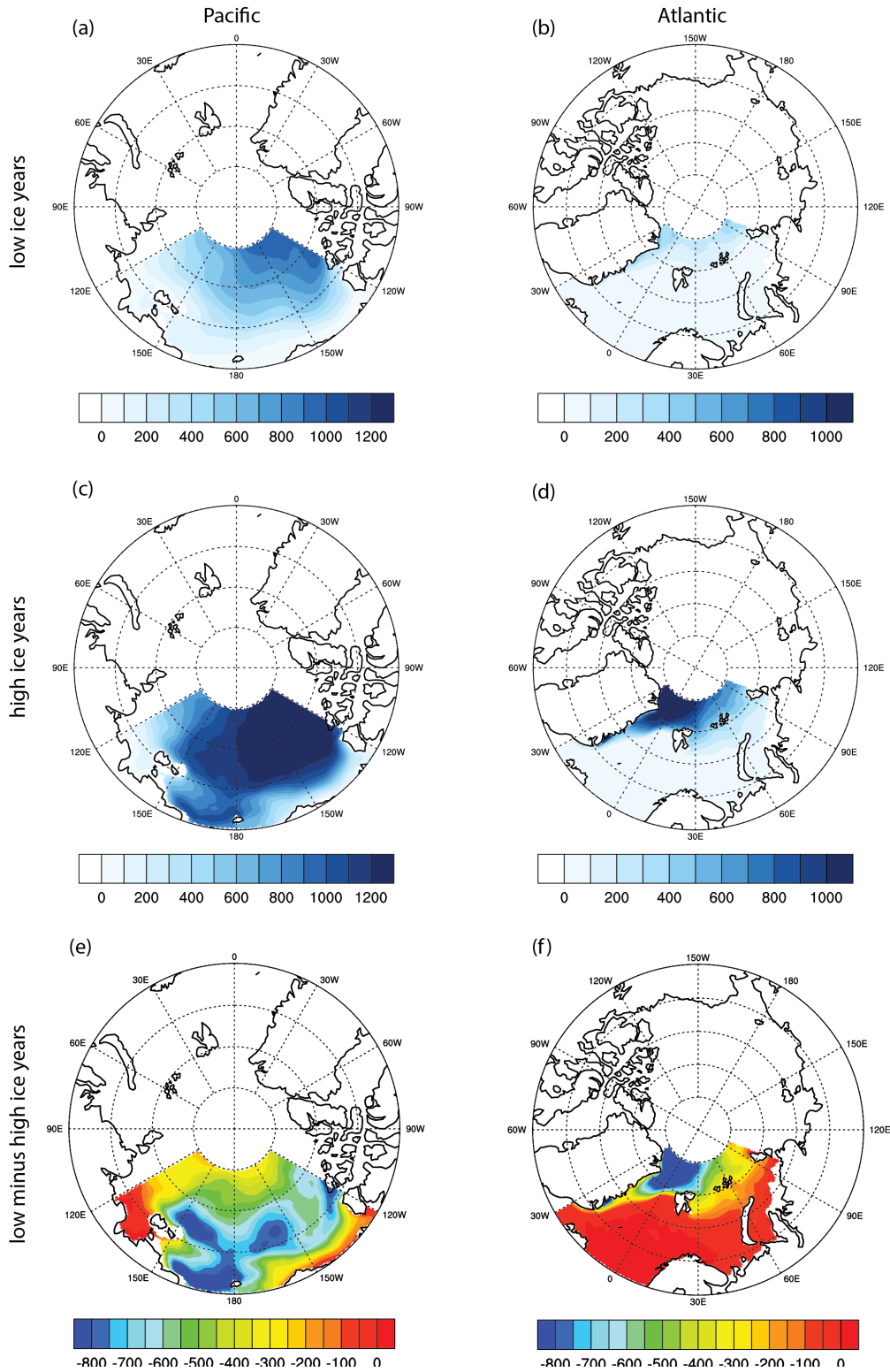
Figure 24. Composite autumn sea ice volume for Pacific and Atlantic sectors in low (a, b) and high (c, d) sea ice volume years. (e, f) are the composite difference between low and high sea ice volume years
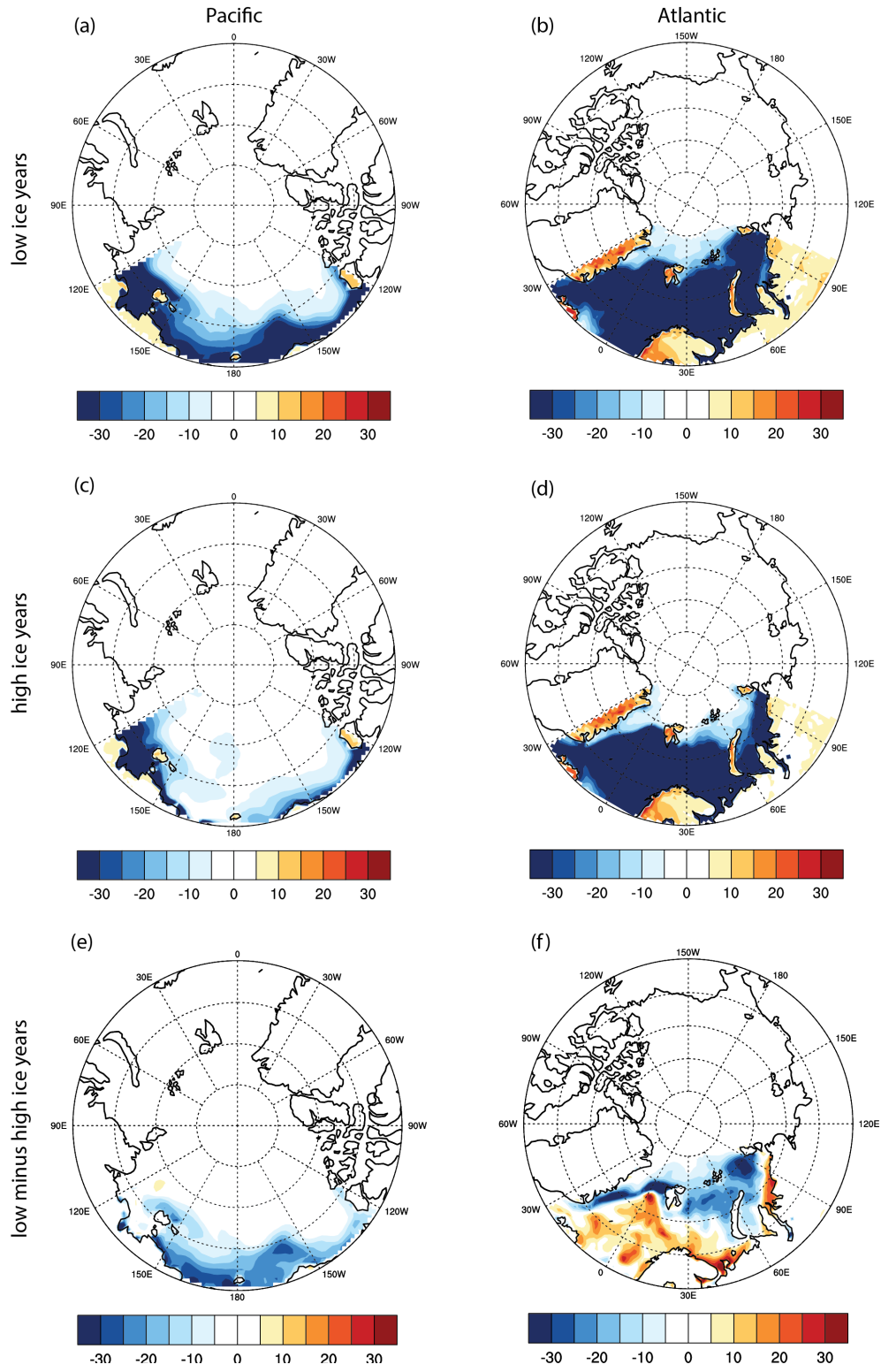
Figure 25. Composite autumn total sensible and latent heat flux for Pacific and Atlantic sectors in low (a, b) and high (c, d) sea ice volume years. (e, f) are the composite difference between low and high sea ice volume years
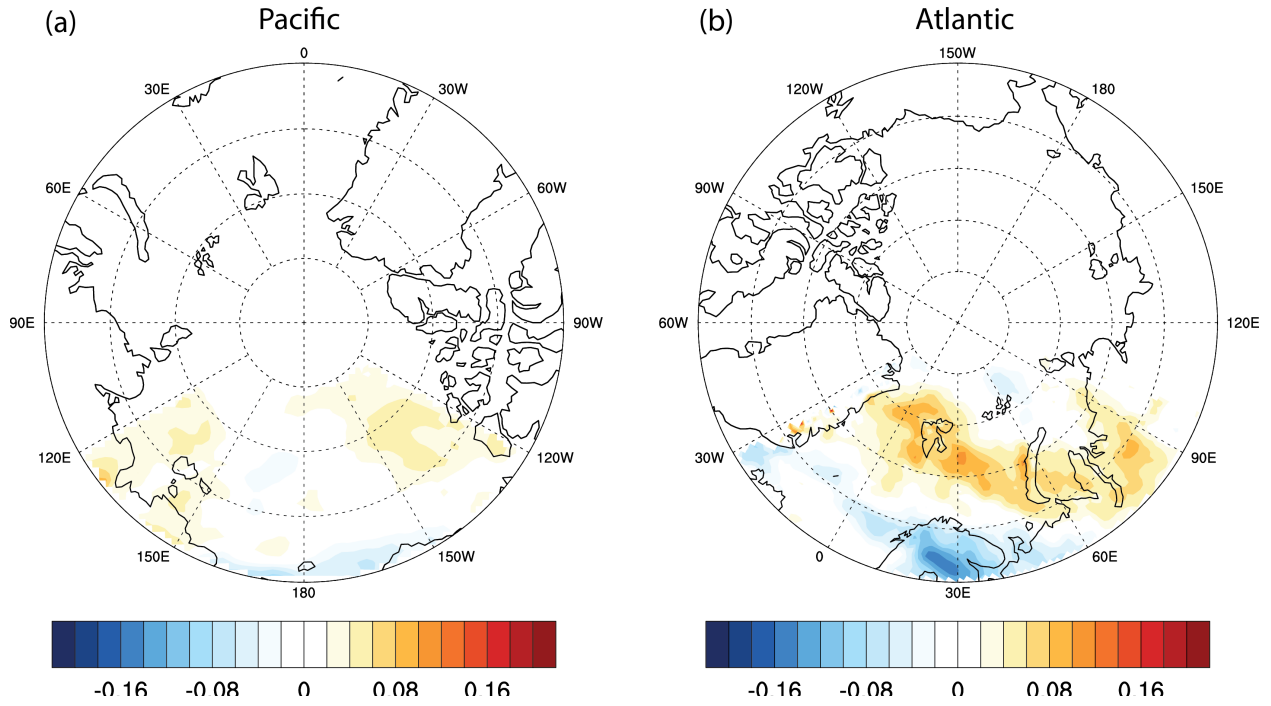
Figure 26. The Eady growth rate composite differences between low and high sea ice years for (a) Pacific and (b) Atlantic sectors for autumn averaged over ten ensembles
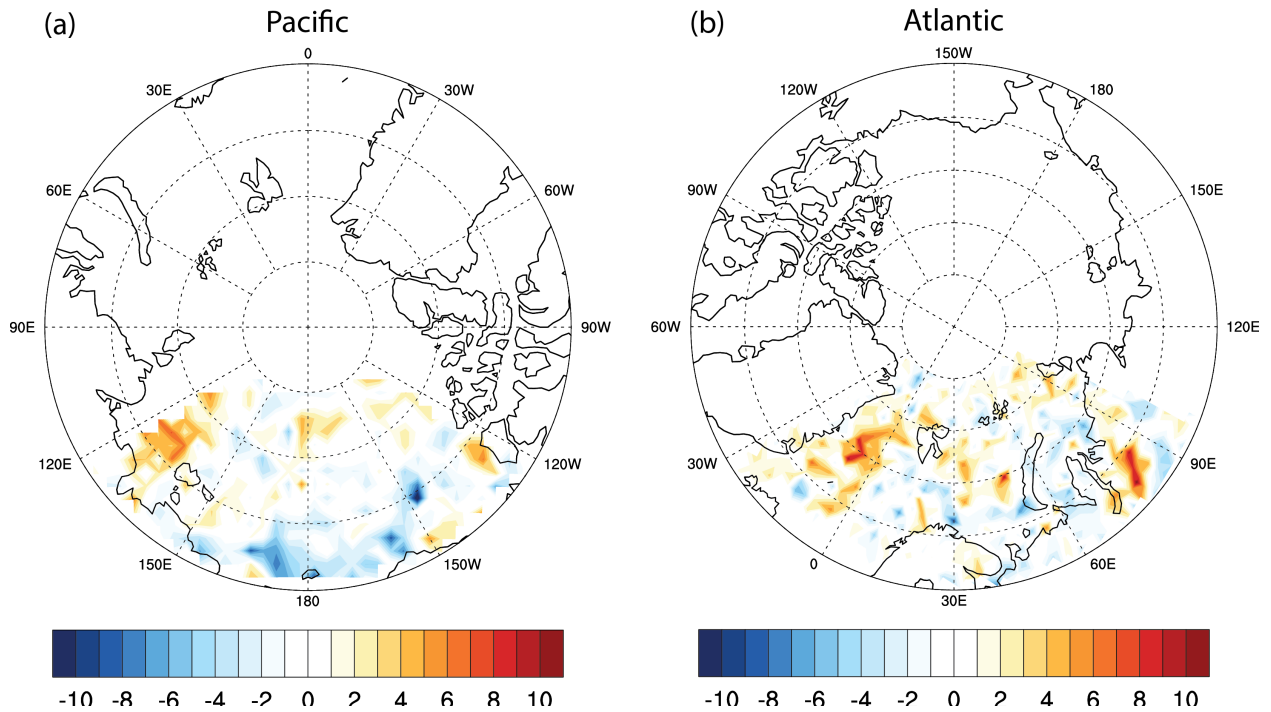
Figure 27. Storm count spatial distribution composite differences between low and high sea ice years for (a) Pacific and (b) Atlantic sectors for autumn averaged over ten ensembles
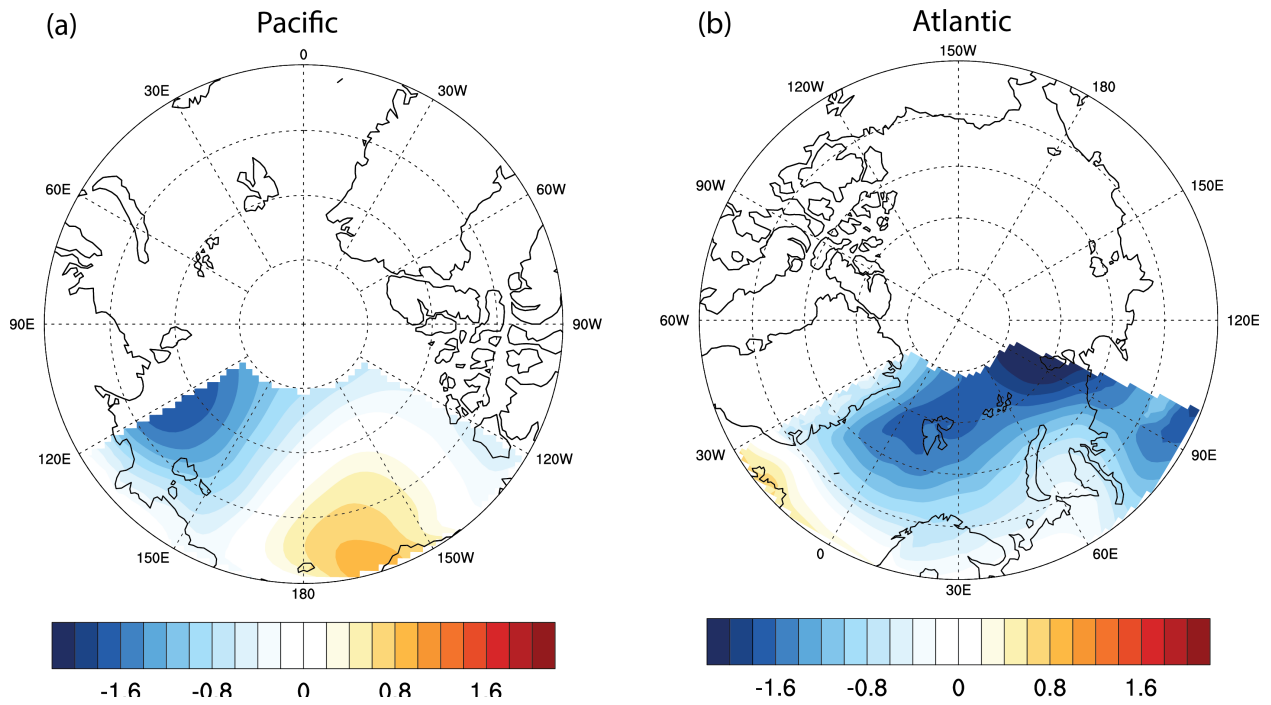
Figure 28. SLP composite differences between low and high sea ice years for (a) Pacific and (b) Atlantic sectors for autumn averaged over ten ensembles
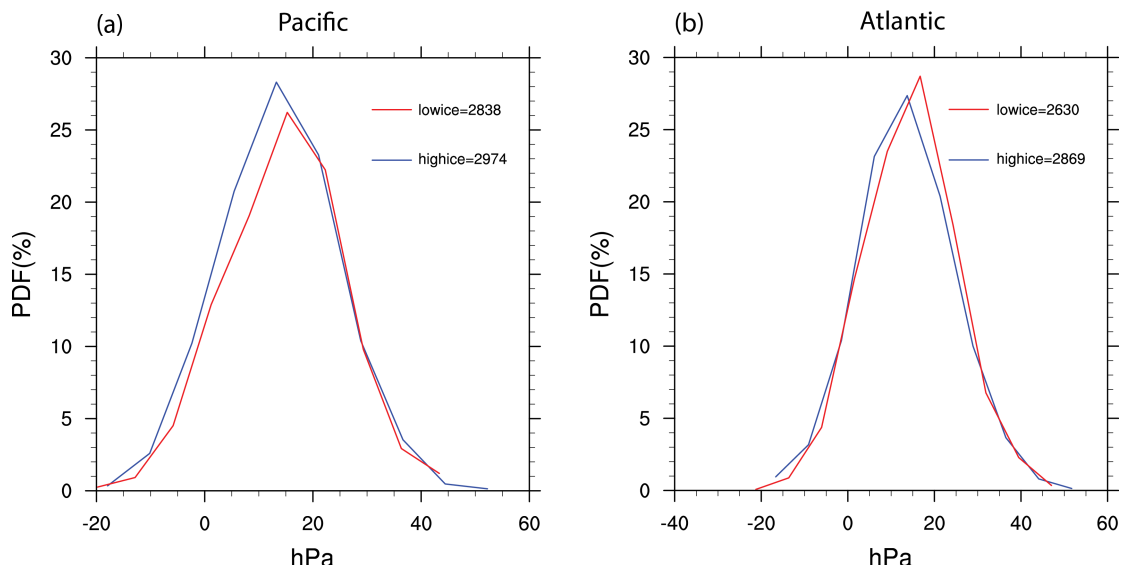
Figure 29. Probability density functions (PDFs) of the autumn storm intensity for Pacific and Atlantic sectors. The red (blue) lines represent storm intensity in low (high) sea ice years
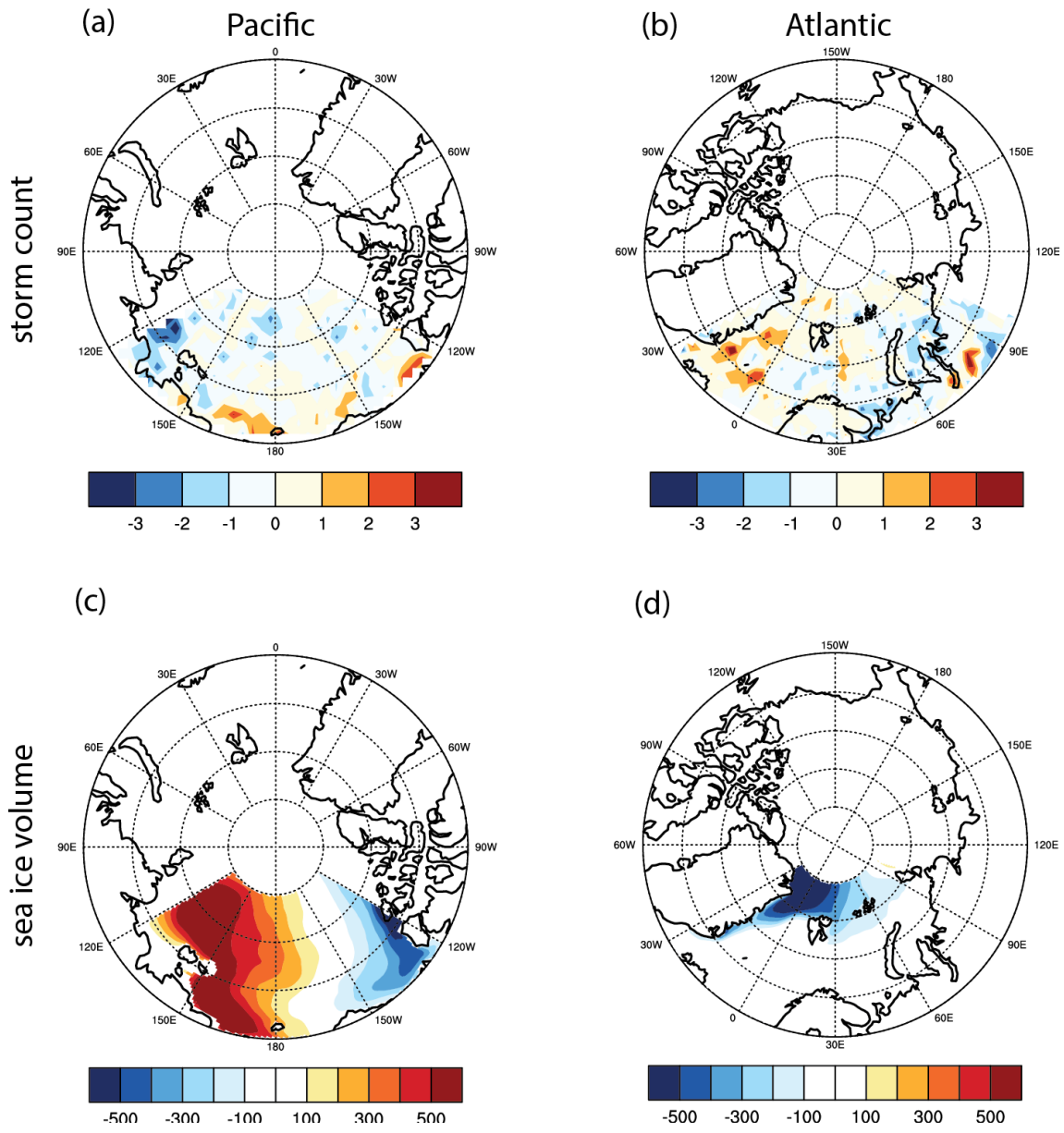
Figure 30. The first pair of coupled patterns in Pacific sector (a, c) and Atlantic sector (b, d) from the maximum covariance analysis (MCA) of sea ice volume and storm count in autumn in. Upper row represents the sea ice volume anomalies and lower row represents

Chapter 4 Influence of stratospheric quasi-biennial oscillation on storm track variability over the

North Pacific

Abstract

A possible mechanism for causing poleward-moving storm tracks to shift over the North Pacific Ocean under the influence of stratosphere quasi-biennial oscillation (QBO) is examined by performing a composite analysis of detailed vertical structure of the storms. During the QBO west phase, storms extend into higher latitudes and extend farther into the Arctic compared to storms in the QBO east phase. QBO west phase storms also tend to travel longer distances meridionally. Detailed vertical atmospheric structure of the storms from the composite analysis shows that a stronger potential vorticity (PV) anomaly associates with the QBO west phase, and this can produce enhanced warm air advection near the surface. A warm core structure at the surface can form east and northeast of storm's surface low pressure center. Isentropes bow downward as a result. Upward motion following the isentropes reduces the surface low pressure, which in turn facilitates propagation of storms to the east and northeast. Under the QBO east phase, there is a weak surface warm core southeast of the storm low pressure center. The development of these storms is relatively slow and they tend to move southeastward.

4.1 Introduction

The quasi biennial oscillation (QBO) is a periodic phenomenon in the equatorial stratosphere. The zonally symmetric westerly and easterly winds alternate with a period of about 26 to 28 months. The QBO phases are classified based on the zonal mean equatorial wind at stratosphere. The QBO

west phase is defined as the years when the mean wind exceeds 10 meter per second and the QBO east phase is defined as the years when the mean wind is less than -10 meter per second.

Previous studies show a connection between the stratospheric quasi-biennial oscillation (QBO) with tropical cyclone activities (Gray, 1984; Shapiro, 1989; Gray et al., 1992; Chan, 1995; Jury et al., 1999). However, the impact of QBO on storms tracks over the North Pacific has received less attention. An improved understanding of the physical mechanisms connecting the QBO to the North Pacific storm tracks has the potential to improve seasonal and decadal scale forecast ability of storm track patterns. Many studies have shown the connection between the stratospheric variability and tropospheric circulation (Baldwin and Dunkerton, 2001; Thompson et al., 2002; Scaife et al., 2014, 2016; Kidston et al., 2015; Hansen et al., 2017) and the direct connection between the QBO and tropospheric processes over tropical and subtropical regions (Giorgetta et al., 1999; Collimore et al., 2003; Ho et al., 2009; Liess and Geller, 2012; Garfinkel and Hartmann, 2011a; Nie and Sobel, 2015). The impact of the QBO on Northern Hemisphere stratospheric polar vorticity (PV) has been well known for decades (Holton and Tan, 1980, 1982; Baldwin et al., 2001; Anstey and Shepherd, 2014). The variability of the equatorial winds affects the vertical propagation of the planetary-scale waves from the troposphere via its influence on the stratospheric waveguide in winter via refraction or reflection of the waves towards or away from high latitudes, respectively. The PV becomes stronger when the QBO winds in the lower-mid stratosphere are westerly phase (Lu et al., 2008, 2014; Anstey and Shepherd, 2008; Christiansen, 2010) and vice-versa the easterly phase.

Mid-latitude storms travel through the North Pacific along an important pathway by which they can impact the Arctic (Zhang et al., 2004). A phase lock between upstream upper-level PV anomalies and downstream lower-level PV anomalies has been shown to contribute to storm

intensification (e.g. Hoskinset al.,1985; Davis and Emanuel, 1991; Rossaet al., 2000; Cavallo and Hakim, 2010; Campa and Wernli, 2012; Odellet et al., 2013). An increased occurrence of intense storms over the North Pacific results in weather hazards, which impact the offshore environment (Dupre, 1980; Dau et al., 2011; Terenzi et al., 2014), coastal communities, and the regional landscape (Anderson et al., 2018). A better understanding of the mechanisms controlling storm track propagation to further predict long-term variability is of great importance. In this study, we connect upper level PV anomaly under two QBO phase conditions to surface storm tracks propagation. In the next section, we briefly describe the data and methods used to detect storms tracks and QBO phases. The third section has an innovative storm composite analysis. In the last section, we summarized our major findings and conclusions.

4.2 Data and methods

West and east phases of the QBO are determined by using the National Centers for Environmental Prediction-National Center for Atmospheric Research (NCEP-NCAR) reanalysis data. The QBO index was calculated by using the monthly and zonally mean wind speed and wind shear between 50 and 70 hPa. We applied our storm detection algorithm based on the sea level pressure (SLP) from the ERA-Interim reanalysis dataset (Dee et al., 2011). Every low pressure center north of 30°N and spanning 1979 to 2018 are identified, and storm tracks are obtained by connecting low centers within a 650 km radius from successive 6-hourly SLP maps. We selected storms with life duration greater than two days and their tracks spanning more than 5 degrees of latitude in the meridional direction over the Pacific sector (Figure 31). Storms that travel zonally are not included in this study. Storms are counted in both months if their duration extends for two months. In this study, we focused on storms during late fall and winter months (November, December, January

and February). Based on the month that a storm occurred and the corresponding QBO index for that month, storms are categorized into two groups. If the QBO index exceeded one standard deviation, the corresponding winter is categorized in the QBO east phase. If the QBO index was less than negative one standard deviation, the corresponding winter is categorized in the QBO west phase.

4.3 Results

A total of 265 and 298 storms tracks were classified into the westerly and easterly phase of the QBO respectively. The storm counts are estimated as the total number of storms within a 5 by 5 grid box. The storm tracks in QBO west and east phases and storm counts are shown in Figure 31. More than half of the storms are in the region south of 55°N and disappear near 180°W, which is close the center of the Aleutian low. Less than half of the total storms move northward into the Arctic. Once the storms pass 60°N, the fraction of storms from the QBO west phase exceeds the storms from the east phase. Therefore, under the QBO west phase, more storms are able to travel further north.

Even though most storms originate in the region between 150°E and 170°E and between 40°N and 45°N in both west and east phases, a clear difference of the storm track distribution pattern can be seen during the two QBO phases. During the QBO west phase, storm tracks tend to form slightly to the west and south of the region relative to the storm tracks during the QBO east phase. A larger difference can be found on the locations where the storms under the west and east phase of the QBO. More storms tend to shift to the west during the QBO east phase relative to the QBO west phase. The distance storms travel is relatively short during the QBO east phase, indicating a longer duration for the storm in the west QBO phase. The probability density function (PDF) is calculated for longitudes and latitudes of the storm tracks start and end locations (Figure

32). As shown in Figure 32a, we find that storm tracks tend to extend more zonally during the QBO east phase as there is a larger range of longitude covered by the storm tracks. On the other hand, storm tracks extend more meridionally during the QBO west phase, indicating that these storms more likely to travel northward into the Arctic. Thus, more storms can propagate into the Arctic region under the QBO west phase condition, while under the QBO east phase storms are more likely to travel zonally and not having potential impact on the Arctic.

To investigate the possible reasons for such different behaviors of the storm tracks and potential linkage to different QBO phases, we conducted a composite analysis for the detailed structure of the storm under both west and east phase QBO influence. The parameters we examined are potential temperature, wind, geopotential height, and potential vorticity. We composite all storms in each phase into a 10 x 10 grid box without any rotation of the frame (e.g. positive y axis always heading to North). In the newly constructed vertical cross section, the origin of the grid box is the center of the composite storm and the relative x and y axis corresponds to zonal and meridional direction. Pressure levels are used as the z coordinate. We select a domain to composite all the storms in that region under QBO east and west phase respectively. The composite region is selected between 55°N and 60°N and between 163°E and 168°E. This longitude range avoids the locations where most storms end. Based on the storm track distribution, the latitude range encompasses region well suited for determining if storms will keep moving northward or eastward. Vertical structures of the composite storm are shown in Figure 33 for both QBO west phase and east phase. As shown in Figure 33a, during the QBO west there is a stronger PV anomaly penetrating from upper level into the lower level compared to the PV anomaly in the QBO east phase. The contours of the PV anomaly during the QBO west phase cover a broader and deeper space. A stronger cyclonic circulation at the upper level exist for the storms of the QBO west phase

indicating by the composite wind vectors compared to the QBO east phase. The location of the center of this PV anomaly is in the upstream direction of the surface low pressure center (northwest of the surface low pressure). Associated with this PV anomaly, the cyclonic circulation results in a strong southerly wind on the east side of the storm. The maximum wind speed corresponding to strong southerly winds can be found at the pressure level of 300 hPa and extend to the surface level. The southerly wind subsequently causes warm air advection near the surface. Over the surface baroclinic zone, the stronger upper level PV anomaly during the QBO west phase induces an enhanced warm air advection and forms a warm core to the northeast of the storm center (Figure 33a). On the other hand, a weaker PV anomaly associated with the QBO east phase corresponds to a relatively weaker warm air advection. The warm core was located southeast of the storm center (Figure 33b). In adjacent to the surface positive potential temperature anomaly, the isentropic surfaces, which are the potential temperature contours, bow downwards from the upper level PV anomaly. The air flow will then follow the isentropic surface traveling into lower level. A stronger warm core corresponding to a steeper slope of the isentropes. The strongest upwards air motion can be found on the east and northeast side of the storm center during the QBO west phase, while to the southeast during the QBO east phase. The rising motion reduces surface pressure and causes storms to develop where the surface pressure keep decreasing. Therefore, storms tend to move east and northeast during the QBO west phase and move along southeastward paths during the east phase of the QBO.

4.4 Conclusions

This study shows the different patterns of the North Pacific storm tracks during the QBO east and west phase using the ERA-Interim reanalysis data. Since the QBO can be predicted well, a better

understanding of the relation between the QBO and the storms can provide useful information for the regional study of the storms and their impacts. Based on the composite analysis of the storm vertical structure, during the QBO east phase storms tracks tend to be shorter in distance and travels along zonally pathways. On the other hand, storm track can extend longer distance and move further northward over a higher latitude into the Arctic compared to the QBO east phase. The underlying mechanism is found to connect to the changes in upper level PV anomaly during the two QBO phases. A stronger PV anomaly during the QBO west phase results in a stronger southerly flow over the western portion of the storm from surface to the upper level, which in turn can cause stronger warm air advection near the surface. A strong surface warm core can form east and northeast relative to the storm low pressure center. The formation of the warm core makes the isentropes bow downward, which results in a slantwise upward motion following the isentropes. The rising motion then causes further reduction of the surface level pressure and propagation of the storm eastward and northeastward. A weaker upper PV anomaly is unable to support further northward displacement of the storms into high latitudes, the associated surface warm air advection is much weaker, and there is not enough baroclinicity to trigger storm development. Therefore, the storm tracks during the QBO east phase tend to be shorter and more zonally distributed. The relation can be used to further predict the storm track pattern under different QBO phases.
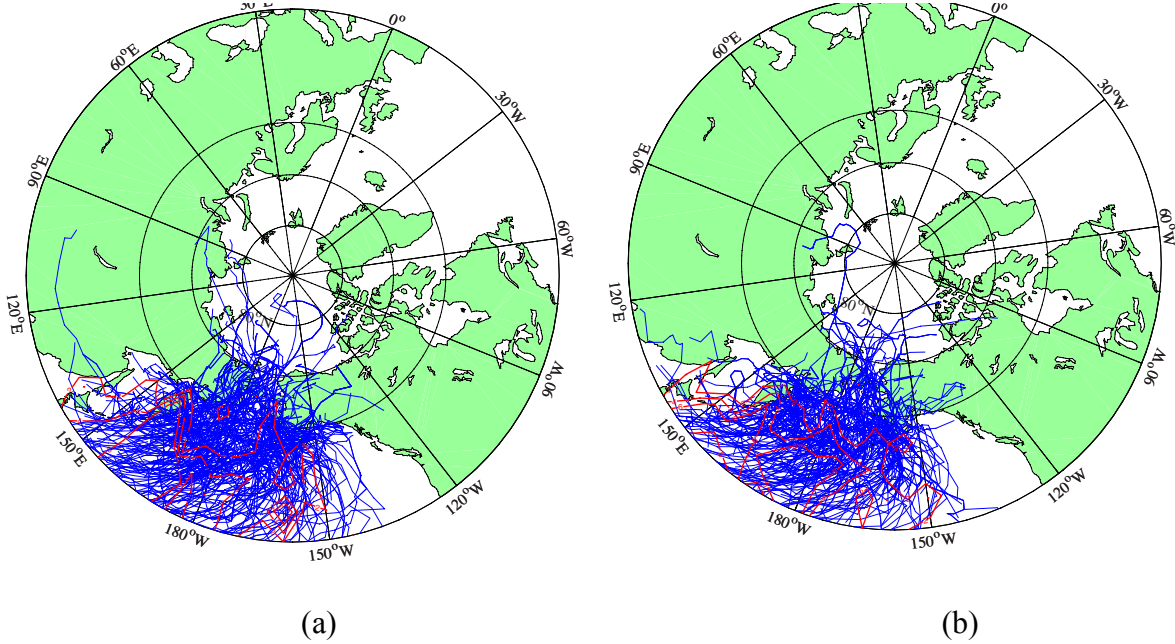
Figure 31. The North Pacific storm tracks (blue lines) and counts (red contours) during the (a) west and (b) east phase of QBO
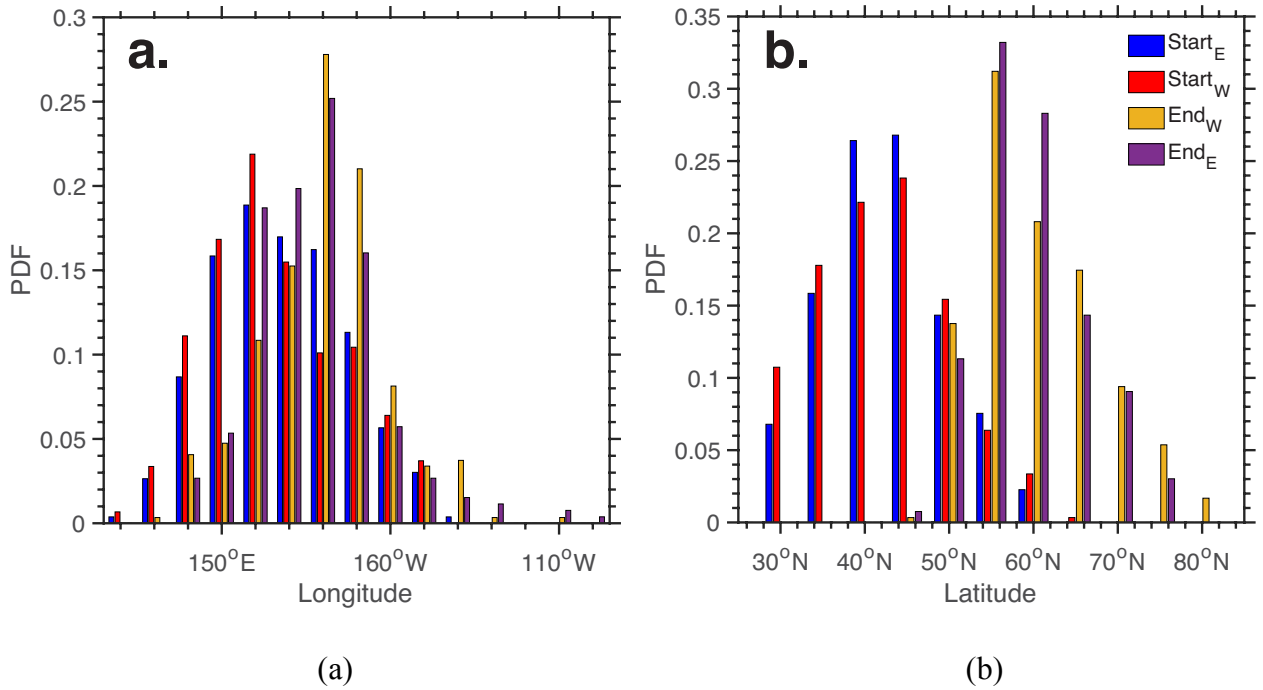
Figure 32. The PDF of the storm's (a) start and end longitudes and (b) start and end latitudes
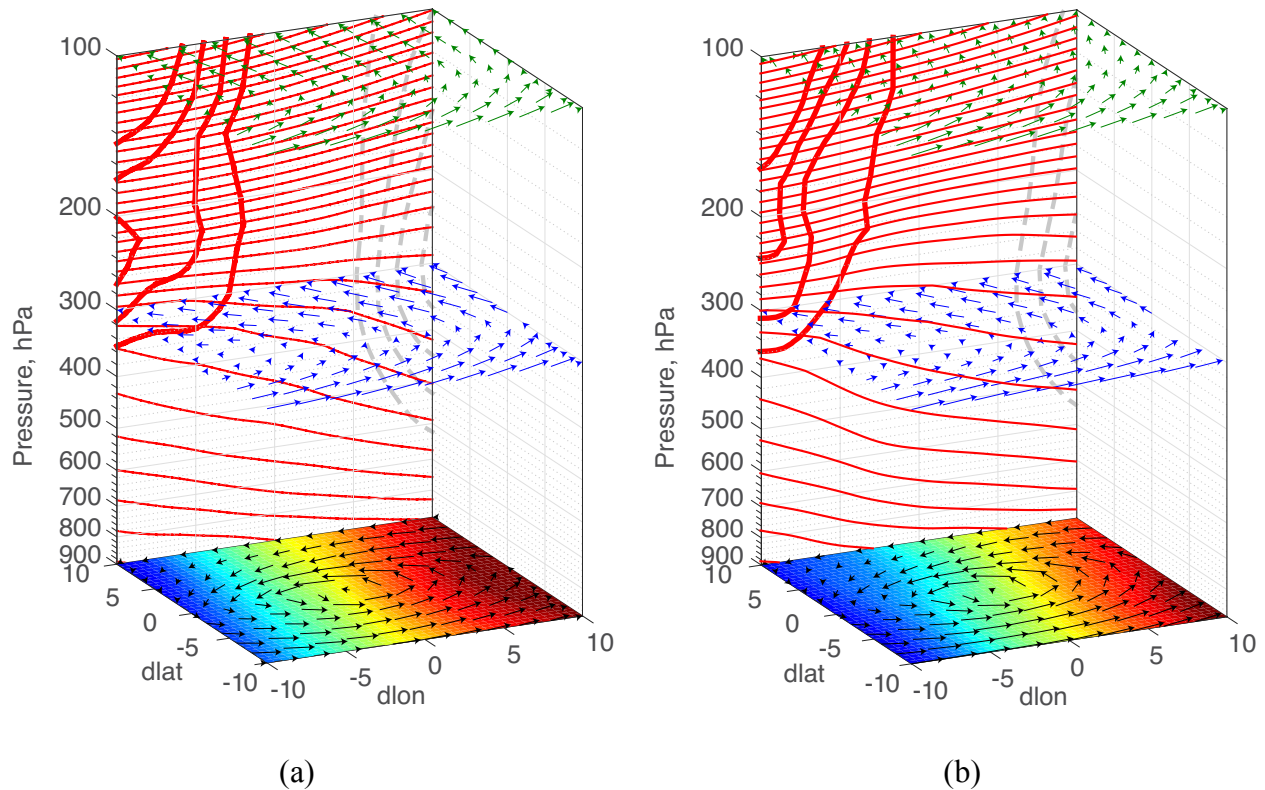
Figure 33. A comparison of the atmospheric structure between QBO (a) east phase and (b) west phase. Black, blue, and green arrows represent the wind vectors at 900 hPa, 300 hPa, and 100 hPa respectively. The potential temperature at 900 hPa are shown as the color

References

Anderson, T. R., C. H. Fletcher, M. M. Barbee, B. M. Romine, S. Lemmo, and J. M. S. Delevaux (2018): Modeling multiple sea level rise stresses reveals up to twice the land at risk compared to strictly passive flooding methods. *Sci. Rep.*, 8, 14484.

Anstey, J. A. and Shepherd, T. G. (2008): Response of the north- ern stratospheric polar vortex to the seasonal alignment of QBO phase transitions, *Geophys. Res.* Lett., 35, L22810.

Anstey, J. A. and Shepherd, T. G. (2014): High-latitude influence of the quasi-biennial oscillation, *Q. J. Roy. Meteor. Soc.*, 140, 1–21.

Baldwin, M. P. and Dunkerton, T. J. (2001): Stratospheric Harbingers of Anomalous Weather Regimes, *Science*, 294, 581–584.

Campa J., Wernli H. (2012): A PV perspective on the vertical structure ofmature midlatitude cyclones in the Northern Hemisphere. *J. Atmos. Sci.*, 69, 725 − 740.

Cavallo SM, Hakim GJ. (2010): Composite structure of tropopause polar cyclones. *Mon. Weather Rev.*, 138, 3840 − 3857.

Collimore, C. C., Martin, D. W., Hitchman, M. H., Huesmann, A., and Waliser, D. E. (2003): On the relationship between the QBO and tropical deep convection, *J. Clim*, 16, 2552–2568.

Chan, J. C. L. (1995): Tropical cyclone activity in the western North Pacific in relation to the stratospheric quasi-biennial oscillation, *Mon. Wea. Rev.*, 123, 2567−2571.

Christiansen, B. (2010): Stratospheric bimodality: can the equatorial QBO explain the regime behavior of the NH winter vortex, *J. Clim*, 23, 3953–3966.

Dau, C. P., J. G. King Jr. and C. J. Lensink (2011): Effects of storm surge erosion on waterfowl habitats at the Kashunuk River, Yukon− Kuskokwim Delta, Alaska. U.S. Fish and Wildlife Service, Anchorage, Alaska, USA.

Davis C. A., Emanuel K. A. (1991): Potential vorticity diagnostics of cyclogenesis. *Mon. Weather Rev.*, 119, 1929 − 1953.

Dee, D. P., Uppala, S. M., Simmons, A. J., Berrisford, P., Poli, P., Kobayashi, S., Andrae, U., Balmaseda, M. A., Balsamo, G., Bauer, P., Bechtold, P., Beljaars, A. C. M., van de Berg, L., Bid- lot, J., Bormann, N., Delsol, C., Dragani, R., Fuentes, M., Geer, A. J., Haimberger, L., Healy, S. B., Hersbach, H., Hólm, E. V., Isaksen, L., Kållberg, P., Köhler, M., Matricardi, M., McNally, A. P., Monge-Sanz, B. M., Morcrette, J.-J., Park, B.-K., Peubey, C., de Rosnay, P., Tavolato, C., Thépaut, J.-N., and Vitart, F. (2011): The ERA-Interim reanalysis: configuration and performance of the data assimilation system, *Q. J. Roy. Meteor. Soc.*, 137, 553–597.

Dupre, W. R. (1980): Yukon Delta coastal processes study. National Oceanic and Atmospheric Administration, Outer Continental Shelf Environmental Assessment Program, *Tech. Rep.*, 58, 393–447.

Giorgetta, M. A., Bengtsson, L., and Arpe, K. (1999): An investigation of QBO signals in the east Asian and Indian mon- soon in GCM experiments, *Clim. Dynam.*, 15, 435–450.

Garfinkel, C. I. and Hartmann, D. L. (2011): The influence of the quasi- biennial oscillation on the troposphere in winter in a hierarchy of models. Part I: Simplified dry GCMs, *J. Atmos. Sci.*, 68, 1273– 1289.

Gray, W. M. (1984): Atlantic seasonal hurricane frequency. Part I: El Nino and 30 mb quasi- biennial oscillation influences, *Mon. Wea. Rev.*, 112, 1649−1668.

Gray, W. M., C. W. Landsea, P. W. Mielke Jr., and K. J. Berry (1992): Predicting Atlantic seasonal hurricane activity 6−11 months in advance, *Wea. Forecasting*, 7, 440−455.

Gray, L. J. (2003): The influence of the equatorial upper stratosphere on stratospheric sudden warmings, *Geophys. Res. Lett.*, 30, 1166– 1169.

Hansen, F., Greatbatch, R. J., Gollan, G., Jung, T., and Weisheimer, A. (2017), Remote control of North Atlantic Oscillation predictability via the stratosphere, *Q. J. Roy. Meteorol. Soc.*, 143, 706–719.

Ho, C. H., Kim, H. S., Jeong, J. H., and Son, S. W. (2009): Influence of stratospheric quasi-biennial oscillation on tropical cyclone tracks in western North Pacific. *Geophys. Res. Lett.*, 36, L06702.

Holton, J. R. and Tan, H. C. (1980): The Influence of Equatorial Quasi- Biennial Oscillation on the Global Circulation at 50 mb, *J. Atmos. Sci.*, 37, 2200–2208.

Holton, J. R. and Tan, H. C. (1982): The quasi-biennial oscillation in the Northern Hemisphere lower stratosphere, *J. Meteorol. Soc. Jpn.*, 60, 140–148.

Hoskins B. J., McIntyre M. E., Robertson A. W. (1985): On the use and significanceof isentropic potential vorticity maps. *Q. J. R. Meteorol. Soc.,* 111, 877 – 946.

Jury, M. R., B. Pathack, and B. Parker (1999): Climatic determinants and statistical prediction of tropical cyclone days in the southwest Indian Ocean, *J. Clim.*, 12, 1738−1746.

Kidston, J., Scaife, A. A., Hardiman, S. C., Mitchell, D. M., Butchart, N., Baldwin, M. P., and Gray, L. J. (2015): Stratospheric in- fluence on tropospheric jet streams, storm tracks and surface weather, *Nat. Geosci.*, 8, 433–440.

Nie, J. and Sobel, A. H. (2015): Responses of tropical deep convection to the QBO: Cloud-resolving simulations, *J. Atmos. Sci.*, 72, 3625− 3638.

Liess, S. and Geller, M. A. (2012): On the relationship between the QBO and distribution of tropical deep convection, *J. Geophys. Res.- Atmos.*, 117, D03108.

Lu, H., Baldwin, P. B., Gray, L. J., and Jarvis, M. J. (2008): Decadal scale changes in the effect of the QBO on the northern stratospheric polar vortex, *J. Geophys. Res.*, 113, D10114.

Lu, H., Bracegirdle, T. J., Phillips, T., Bushell, A., and Gray, L. J. (2014): Mechanisms for the Holton – Tan relationship and its decadal variation, *J. Geophys. Res.- Atmos.*, 119, 2811–2830.

Odell L., Knippertz P., Pickering S., Parkes B., Roberts A. (2013): The Braer storm revisited. *Weather,* 68, 105 – 111.

Rossa A. M., Wernli H., Davies H. C. (2000): Growth and decay of an extratropical cyclone's PV-tower. *Meteorol. Atmos. Phys.*, 73: 139 – 156.

Scaife, A. A., Athanassiadou, M., Andrews, M., Arribas, A., Baldwin, M., Dunstone, N., Knight, J., MacLachlan, C., Manzini, E., Müller, W. A., Pohlmann, H., Smith, D., Stockdale, T., and Williams, A. (2014): Predictability of the quasi-biennial oscillation and its northern winter teleconnection on seasonal to decadal timescales. *Geophys. Res. Lett.*, 41, 1752–1758.

Scaife, A. A., Karpechko, A. Y., Baldwin, M. P., Brookshaw, A., Butler, A. H., Eade, R., Gordon, M., MacLachlan, C., Martin, N., Dunstone, N., and Smith, D. (2016): Seasonal winter forecasts and the stratosphere, *Atmos. Sci. Lett.*, 17, 51–56.

Shapiro, L. (1989): The relationship of the QBO to Atlantic tropical storm activity, *Mon. Wea. Rev.*, 117, 1545–1552.

Terenzi, J., M. T. Jorgenson, and C. R. Ely. (2014): Storm-surge flooding on the Yukon–Kuskokwim Delta, Alaska. Arctic 67:360–374.

Thompson, D. W. J., Baldwin, M. P., and Wallace, J. M. (2002): Stratospheric connection to Northern Hemisphere win- tertime weather: Implications for prediction, *J. Clim*, **15**, 1421–1428.

Zhang, X., J. E. Walsh, J. Zhang, U. S. Bhatt, and M. Ikeda (2004): Climatology and interannual variability of Arctic cyclone activity, 1948–2002. *J. Clim*., 17, 2300– 2317.

Chapter 5 Conclusion

The main focus of the work presented in this dissertation is synoptic storm activity in the regions over the Chukchi and Beaufort Seas, the Arctic and the North Pacific. Climatology of the storms travelling into the Chukchi and Beaufort Seas from different origins have significantly different impacts. The storms travelling from the East Siberia Sea into the region have the longest duration and strongest intensity in summer. On the other hand, storms from the North Pacific are most active during the winter. Therefore, in order to better understand the impact of storms on the surface climate, storms with different origins are grouped based on their track orientation to study their resulting impacts on surface environmental conditions. An updated storm track algorithm has been adapted in this study to select intense storms coming from the East Siberian Sea and the North Pacific, based on CBHAR reanalysis data from 1979 to 2009. With this algorithm, storm start and end locations, storm duration, distribution were investigated. The responses of the surface climate to storms moving from the west and storms moving from the south into the Chukchi and Beaufort Seas show significant differences in surface temperature, sea level pressure, surface wind, sea surface temperature, sea ice and radiation fields. The change of the west and northeasterly wind to southerly wind in the presence of storms has the greatest impact on sea ice for both eastward and northward moving storms. Strong southerly winds can bring warm and moist air from North Pacific into the Arctic, increasing the surface and sea temperature and inducing sea ice melt. Decreasing sea ice may lead to stronger winds (Mioduszekwki et al., 2018). The connections between wind and sea surface temperature are complicated by the presence of sea ice (Zhang et al., 2018). In the future, climate model experiments can be used to further investigate the underlying physical processes of sea ice melt caused by wind and surface radiative fluxes. The

analysis should expand from 1979 to the present using updated reanalysis data to include recent years.

We study the connection between sea ice and storms over the Arctic region from the perspective changing storm activity resulting from variable sea ice conditions. We divide the Arctic into the North Atlantic sector and the North Pacific sector to study the impact of low and high sea ice on storms in these areas. Sea ice volumes are calculated for each of the sectors based on sea ice concentration and thickness data from 1979 to 2014. The high and low sea ice years are selected when the sea ice volume is higher or lower than one standard deviation from the mean value. Composite analysis based on 10 hindcast ensemble simulations from a coupled atmosphere-sea ice model was used to investigate the storm center count distribution and the central low pressure. Since baroclinic instability is the main mechanism for synoptic storm development, in the low sea ice years with more open water the baroclinicity increase significantly in the winter months. Thus, regions with high baroclinicity favors increases of storm activity as there is more open water in the low sea ice years. On the other hand, regions with low baroclinity has fewer storms and lower storm intensity. We apply the maximum covariance analysis using the singular value decomposition to study the correlation between the sea ice and storm count. The results are similar to the composite analysis: when there is less sea ice the storm counts increase, whereas when there is more sea ice in the region, storm occurrences decline. Therefore, the region over Laptev Sea and Beaufort Sea in the Pacific sector and Greenland Sea and Barents Sea in the Atlantic are the regions where storms occur the most when in the sea ice ow years. The storm count and sea ice correlation can be affected by the decadal scale atmosphere variation (Deser et al., 2000; Zhang et al., 2008); it would be help to isolate the impact of decadal variability.

Storm tracks over the North Pacific are under the influence of the equatorial stratosphere quasi-biennial oscillations (QBO). The QBO is a phenomenon that occurs about every two years, and is well predicable. We examined the relation between the QBO and the storm track pattern over the North Pacific in relation to storm activity. Based on the selected QBO west and east phase years, composite analysis is conducted to study different storm track patterns over the North Pacific Ocean. In this study, we examine storms in the cold seasons over the North Pacific Ocean from the years between 1979 and 2018 based on the ERA-Interim reanalysis data We find that during the QBO west phase more storms tend to move further north into the Arctic and the track extend more meridionally. The storms during the QBO east phase are more likely to travel in the zonal direction, and does not have any significant impact on the Arctic. Detailed storm vertical cross sections examined the potential vorticity (PV) anomaly. We found that the PV anomaly penetrates deeper from the upper level to the lower level and covers a broader region during the QBO west phase. The associated cyclonic circulation induces strong southerly winds and increase warm air advection near the surface, which promotes the development of the intense storms. This study showed connections between the stratosphere QBO and troposphere synoptic storm activity. This is of great practical importance for future prediction of storm activity in winter months. This result indicates that the QBO can provide prediction for the North Pacific storm activity. Based on previous studies, knowledge of the stratosphere can be used to improve longer timescale forecast for the surface climate on seasonal time scales (Thompson et al., 2002; Fereday et al., 2012). Operational forecasts work best when the stratosphere is in a most active state (Mukougawa et al., 2009; Scaife et al., 2014). Large uncertainty remains and accurate seasonal predictions of the North Pacific storms based on the stratospheric and tropospheric processes needs further investigation.

Numerical models using simulation of stratosphere and troposphere coupling is likely to help improve prediction accuracy.

Reference

Deser, C., J. E. Walsh, and M. S. Timlin (2000): Arctic sea ice variability in the context of recent atmospheric circulation trends, *J. Clim*, 13, 617–633.

Fereday, D. R., Maidens, A., Arribas, A., Scaife, A. A. & Knight, J. R. (2012): Seasonal forecasts of Northern Hemisphere winter 2009/10. *Environ. Res. Lett.*, 7, 034031.

Mioduszewsku, J., S. Vavrus, and M. Wang (2018): Diminishing Arctic sea ice promotes stronger surface winds. *J. Clim*, 31, 8101–8119.

Mukougawa, H., Hirooka, T. & Kuroda, Y. (2009): Influence of stratospheric circulation on the predictability of the tropospheric Northern Annular Mode. *Geophys. Res. Lett*. 36, L08814

Scaife, A. A. (2014): Predictability of the quasi-biennial oscillation and its northern winter teleconnection on seasonal to decadal timescales. *Geophys. Res. Lett*. 41, 1752–1758

Thompson, D. W. J., Baldwin, M. P. & Wallace J. M. (2002): Stratospheric connection to Northern Hemisphere wintertime weather: implications for prediction. *J. Clim*. 15, 1421–1428

Zhang, J., S. T. Stegall, and X. Zhang (2018): Wind–sea surface temperature–sea ice relationship in the Chukchi–Beaufort Seas during autumn. *Environ. Res. Lett.*, 13, 034008.

Zhang X, Sorteberg A, Zhang J, Gerdes R, Comiso JC (2008) Recent radical shifts of atmospheric circulations and rapid changes in Arctic climate system. *Geophys. Res. Lett.,* 35, L22701.